REPORT DOCUMENTATION PAGE

AFRL-SR-AR-TR-08-0049

1. REPORT DATE *(DD-MM-YYYY)*

2. REPORT TYPE
Final Technical Report

3. DATES COVERED (From – To)
1 September 2005 – 31 August 2007

4. TITLE AND SUBTITLE
Modeling of Flowing Plasmas and Pulse Power Schemes for O2 Production for Chemical Lasers

5a. CONTRACT NUMBER

5b. GRANT NUMBER
FA9550-05-1-0470

5c. PROGRAM ELEMENT NUMBER

6. AUTHOR(S)
Professor Mark J. Kushner

5d. PROJECT NUMBER

5e. TASK NUMBER

5f. WORK UNIT NUMBER

7. PERFORMING ORGANIZATION NAME(S) AND ADDRESS(ES
Department of Electrical and Computer Engineering
Iowa State University
104 Marston Hall
Ames IA 50011-2151

8. PERFORMING ORGANIZATION REPORT NUMBER

9. SPONSORING/MONITORING AGENCY NAME(S) AND ADDRESS(ES)
USAF/AFRL
AFOSR
875 North Randolph Street
Arlington VA 22203
Dr Michael Berman/NA

10. SPONSOR/MONITOR'S ACRONYM(S)
AFOSR

11. SPONSORING/MONITORING AGENCY REPORT NUMBER
N/A

12. DISTRIBUTION AVAILABILITY STATEMENT

Distribution Statement A: Approved for public release. Distribution is unlimited.

13. SUPPLEMENTARY NOTES

14. ABSTRACT

The objectives of the research program were met. Significant progress was made in improving our understanding of the plasma kinetics of O2(1?) production for pumping of eCOILs. Advances were made in 3 areas: 1) pulse power schemes, 2) use of additives and 3) high pressure operation. Methods and scaling laws were developed to optimize the yield of O2(1?) in flowing plasmas in each of these areas.

15. SUBJECT TERMS

16. SECURITY CLASSIFICATION OF:			**17. LIMITATION OF ABSTRACT**	**18. NUMBER OF PAGES**	**19a. NAME OF RESPONSIBLE PERSON**
a. REPORT	**b. ABSTRACT**	**c. THIS PAGE**	Unclassified	49	**19b. TELEPONE NUMBER** *(Include area code)*
Unclassified	Unclassified	Unclassified			(703)

Final Report

MODELING OF FLOWING PLASMAS AND PULSE POWER SCHEMES FOR $O_2(^1\Delta)$ PRODUCTION FOR CHEMICAL LASERS

Contract FA95500510470

Period of Performance
1 September 2005 – 31 August 2007

Submitted to:

Dr. Michael Berman (michael.berman@afosr.af.mil)
Air Force Office of Scientific Research

Submitted by:

Prof. Mark J. Kushner
Iowa State University
Department of Electrical and Computer Engineering
104 Marston Hall
Ames, IA 50011-2151
Voice: (515) 294-9988 FAX: (515) 294-9273 mjk@iastate.edu

19 January 2008

Objectives:

A program of research was conducted during which modeling of the plasma kinetics of $O_2(^1\Delta)$ generation in flowing plasmas for use in electrically excited chemical oxygen iodine lasers (eCOILs) was investigated. The goals of this program were to improve the knowledge base in this important technology area, provide computational support to ongoing experiments and to propose new plasma excitation strategies to optimize and scale $O_2(^1\Delta)$ production and yields.

Status of Effort:

The objectives of the research program were met. Significant progress was made in improving our understanding of the plasma kinetics of $O_2(^1\Delta)$ production for pumping of eCOILs. Advances were made in 3 areas: 1) pulse power schemes, 2) use of additives and 3) high pressure operation. Methods and scaling laws were developed to optimize the yield of $O_2(^1\Delta)$ in flowing plasmas in each of these areas.

Accomplishments and New Findings:

Computational Issues:

In this computational investigation, two modeling platforms were utilized. *nonPDPSIM* is a two dimensional, plasma hydrodynamics model in which the fundamental plasma kinetics equations are solved in concert with the Navier-Stokes equations for flow, plasma chemistry and electromagnetics (or electrostatics). *Global_Kin* is a global or plug flow model which uses the same reaction mechanisms as *nonPDPSIM*. Given its less-dimensional nature, *Global_Kin* runs more rapidly. Significant computational improvements were made to *nonPDPSIM* to enable simulation of spiker-sustainer circuitry, high pressure flow at high power, and having multiple nozzles for injection of gases. Similar improvements were made to *Global_Kin*.

Spiker Sustainer Circuitry:

Operation of the chemical oxygen-iodine laser (COIL) is based on an electronic transition between the spin-orbit levels of the ground state configuration of the iodine atom $I(^2P_{1/2}) \rightarrow I(^2P_{3/2})$ (1.315 μm). The upper level is populated by near resonant energy transfer (quantum defect ~ 219 cm^{-1}) from $O_2(^1\Delta)$ to ground state $I(^2P_{3/2})$. The COIL generates ground state I by dissociative excitation transfer from $O_2(^1\Delta)$ to I_2. Production of $O_2(^1\Delta)$ using electric discharges, eCOIL, provides a means for an all gas phase system. Much of the development of eCOIL has focused on efficiently generating $O_2(^1\Delta)$ by engineering the operating E/N (electric field/gas number density) of the discharge to be closer to the optimum value for exciting $O_2(^1\Delta)$. To maximize the fraction of discharge power that is directly dissipated in the electron-impact excitation of $O_2(^1\Delta)$, the electron temperature, T_e, should be near 1.2 eV, which corresponds to an E/N of $\approx$10 Townsend [1 Townsend (Td) = 10^{-17} V-cm^2]. Self-sustained discharges in He/O_2 mixtures operate at least a few tens of Td.

One of the methods to reduce the time averaged electron temperature is to use a pulsed discharge in which a short, high power pulse (the spiker) is followed by a longer period of lower power (the sustainer) before applying another high power pulse. The duration of the high power pulse should be long enough for T_e to spike and for the gas to avalanche, producing an electron density in excess of the steady-state value. The high power pulse should be short enough so that the discharge does not come into a quasi-steady state. If there is sufficient excess ionization during the period of lower power deposition, there may be an extended period where T_e falls below the self-sustaining value, T_{eo}, which for He/O_2 mixtures enables a more efficient production of $O_2(^1\Delta)$. The duty cycle of the spiker and length of the sustainer should be chosen so that the average value of electron temperature $\overline{T}_e < T_{eo}$. The optimum length of the sustainer is then largely determined by the time required for the electron density to decrease to its steady state value, thereby increasing T_e towards T_{eo}. This method for engineering T_e is often referred to as spiker-sustainer (S-S) excitation.

In previous work we found that the yield of $O_2(^1\Delta)$ generally scales linearly with energy deposition for moderate loadings up to 5-8 eV/O_2-molecule. Energy deposition beyond these values produces excess dissociation which ultimately reduces yield. Initial scaling studies of S-S excitation suggested that under ideal conditions, as are represented by global models, $O_2(^1\Delta)$ yields approaching 30% might be possible using S-S methods. In this work, we computationally investigated S-S methods for optimizing $O_2(^1\Delta)$ producing using *nonPDPSIM*. Doing so more realistically represents the electrical circuitry, electrode losses, uniformity and flow considerations. In particular, we investigated capacitively coupled radio frequency (rf) excited systems in He/O_2 mixtures.

We found that S-S methods do hold the potential for increasing $O_2(^1\Delta)$ yields above that for continuous wave (CW) excitation for the same average power, though the amount of the increases is less than that suggested by the global models. S-S techniques generally do lower the time averaged T_e compared to CW excitation and so improve the efficiency of excitation and yield for $O_2(^1\Delta)$. This advantage to S-S excitation is diminished at higher powers where T_e is naturally lower for CW excitation. Lower duty cycles (shorter spiker pulses) are generally more advantageous for S-S excitation as the limit of a delta-function spiker is approached. Increasing the frequency of excitation is also advantageous due to the lowering of T_e and increasing the electron density, n_e. Again, the advantage of S-S excitation is diminished as frequency increases due to the natural decrease in T_e with CW excitation. The length of the sustainer pulse should be short enough so that T_e is largely below the self sustaining value but long enough so that T_e and n_e begin recovering towards their steady-state values. This recovery indicates a good utilization of the excess ionization produced by the spiker.

For details, see the Appendix for the reprint: Natalia Yu. Babaeva, R. A. Arakoni and M. J. Kushner, "Production of $O_2(^1\Delta)$ in Flowing Plasmas Using Spiker-Sustainer Excitation", J. Appl. Phys. **99**, 113306 (2006).

Use of Additives:

In eCOIL systems, $O_2(^1\Delta)$ is typically generated upstream of the laser cavity. I_2 is injected immediately prior to the cavity upon which the flow is supersonically expanded to lower the gas temperature as required to maximize the gain. A challenge in eCOILs is to produce sufficiently high yields of $O_2(^1\Delta)$, and hence laser gain, to enable the laser transition to be saturated and produce high power. In this regard, recent research has focused on tailoring the discharge parameters and using additives such as CO, H_2, D_2 and NO to improve the excitation efficiency of $O_2(^1\Delta)$. NO and NO_2 are also used as additives to control the post-discharge chemistry. In fact, all demonstrations of laser gain and oscillation to date have used flowing plasmas in He/O_2 mixtures with NO as an additive.

eCOILs differ from conventional COILs in that atomic oxygen is also produced in the electrical discharge by electron impact dissociation of O_2. The O atoms flow downstream where 3-body reactions produce O_3 and the remaining O atoms may react with the injected I_2. Beneficial reactions of O with I_2 produce ground state $I(^2P_{3/2})$ atoms (referred to as I), thereby eliminating the expense of $O_2(^1\Delta)$ molecules for the initiating dissociating reactions. Detrimental reactions involving O atoms include quenching of $I(^2P_{1/2})$ (the upper laser level, referred to as I^*) which reduces gain. As such, management of the O atom density is important to optimizing these opposing effects.

Injection of NO or NO_2 through or downstream of the discharge in eCOIL systems has two goals; improving the efficiency of direct production of $O_2(^1\Delta)$ in the discharge by electron impact and management of the O atom density downstream of the plasma. Including NO in the gas stream flowing through the discharge has, in part, the goal of improving production of $O_2(^1\Delta)$. NO, having a lower ionization potential (9.26 eV) than either O_2 or He, is likely to provide more rapid ionization with the possibility of lowering the operating E/N (electric field/gas number density) and electron temperature, T_e. Lowering T_e from the values typical of self-sustained He/O_2 mixtures is advantageous in more efficiently producing $O_2(^1\Delta)$ by direct electron impact. Discharges in NO have also been known to produce $O_2(^1\Delta)$ in relatively large amounts even though O_2 may not be present as a feedstock gas. However, when flowing NO through the discharge, some of the power that would otherwise be available to excite O_2 is dissipated by excitation and ionization of NO, an unwanted consequence.

In addition to possibly improving the production of $O_2(^1\Delta)$, NO and NO_2 are potentially effective in managing the inventory of O atoms through direct and cyclic reactions which have the effect of converting O atoms back into O_2. In the context eCOIL systems where I_2 is injected, O atoms are beneficial by dissociating I_2 (and product species IO) to form I atoms which are then pumped to I^* by collisions with $O_2(^1\Delta)$. The O atoms are detrimental by quenching I^*. Totally eliminating O atoms is therefore not necessarily beneficial. NO and NO_2 also have secondary effects in that they react with I atoms forming intermediary species such as INO, and INO_2 which further react with I to reform I_2.

A computational investigation was performed on the consequences of NO and NO_2 additives on flowing He/O_2 plasmas and their afterglows with I_2 injection. These investigations were conducted using *nonPDPSIM* and *Global_Kin*. We fund that although for most conditions the addition of NO to the inlet gas stream reduced the density of $O_2(^1\Delta)$, it ultimately increased the densities of I^* downstream of the discharge through management of the O atom density. The inlet NO mole fraction also typically increased the extent of the region over which positive laser gain could be achieved. This can be particularly useful in high speed flows where mixing lengths are longer. Injection of NO_2 in the post-discharge flow can help in rapidly scavenging O atoms in two body reactions (as compared to scavenging by NO which proceeds by a 3-body mechanism). In general, addition of NO_2 in the post-discharge region improves laser gain. The downside to NO_2 injection is a rise in gas temperature due to the exothermicity of the reactions between NO_2 and O.

For details, see the Appendix for the reprint: R. A. Arakoni, N. Y. Babaeva and M. J. Kushner "$O_2(^1\Delta)$ Production and Gain in Plasma Pumped Oxygen-Iodine Lasers: Consequences of NO and NO_2 Additives", J. Phys. D **40**, 4793 (2007).

High Pressure Operation:

Many system issues motivate operating eCOILs at higher pressures to obtain larger densities of $O_2(^1\Delta)$ for a given yield and to provide higher back pressure for supersonic expansion in the laser cavity. If higher order effects are not important, and parameters such as energy deposition per molecule are maintained constant, it is expected that absolute $O_2(^1\Delta)$ production (that is, the total number of $O_2(^1\Delta)$ molecules produced) should scale linearly with pressure, thereby providing additional motivation for higher pressure operation.

In previous work, it was found that the yield of $O_2(^1\Delta)$ generally scaled linearly with energy deposition at low pressures (<10 Torr) until the ground state O_2 is depleted. We computationally investigated radio frequency (rf) discharge excited flowing He/O_2 plasmas using *nonPDPSIM* and *Global_Kin* with the goal of developing scaling laws for $O_2(^1\Delta)$ production in eCOIL systems when operating at higher pressures.

We found that the densities and yields of $O_2(^1\Delta)$ can have significant sub-linear scaling with pressure. Although yields may decrease with increasing pressure, the absolute densities of $O_2(^1\Delta)$ typically do increase. Although these results depend on the layout of the electrodes and the aspect ratio of the flow tube more general conclusions can be made. Obtaining high yields of $O_2(^1\Delta)$ will require careful management of the O_3 density. Left unchecked, quenching of $O_2(^1\Delta)$ by the O_3 produced at high pressure is a rate limiting step. At higher energy densities and pressures, quenching by O atoms and energy pooling with $O_2(^1\Delta)$ may also become important. This is particularly the case for possible 3-body quenching involving O atoms, though the importance of this reaction can be minimized by managing the density of O atoms with additives such as NO. Pressure scaling also requires management of the gas temperature, as exothermic recombination reactions rapidly increase. Although the destruction of O_3 at higher temperatures is beneficial, in general an intermediate gas temperature is likely preferred.

Discharge stability must also be managed and this will be highly temperature dependent. Non-uniform excursions of gas temperature in the plasma zone will likely produce non-uniform power deposition and constrictions near the electrodes. As such, low aspect ratio, transverse electrodes allowing for more aggressive gas cooling and more distributed electric fields will likely be required for high pressure operation

For details, see the Appendix for the reprint: N. Y. Babaeva, R. A. Arakoni and M. J. Kushner "$O_2(^1\Delta)$ Production in High Pressure flowing He/O2 Plasmas: Scaling and Quenching", J. Appl. Phys. **101**, 123306 (2007).

Personnel Supported:

1. Dr. Natalie Yu. Babaeva, Post-doctoral Research Fellow
2. Mr. Ramesh Arakoni, Graduate student in Aerospace Engineering
3. Prof. Mark J. Kushner, Faculty Principle Investigator

Peer Reviewed Journal Articles (Citations to date exclude self-citations):

1. D. Shane Stafford and M. J. Kushner, "$O_2(^1\Delta)$ Production in Flowing He/O_2 Plasmas I: Axial Transport and Pulsed Power Formats," J. Appl. Phys. **98**, 073303 (2005). [Note: Work was dominantly completed under prior AFRL/AFOSR support.] 6 citations.
2. R. Arakoni, D. Shane Stafford, Natalia Y. Babaeva and M. J. Kushner, "$O_2(^1\Delta)$ Production in Flowing He/O_2 Plasmas II: 2-dimensional Modeling," J. Appl. Phys. **98**, 073304 (2005). [Note: Work was dominantly completed under prior AFRL/AFOSR support. 5 Citations]
3. N. Y. Babaeva, R. Arakoni and M. J. Kushner, "Production of $O_2(^1\Delta)$ in Flowing Plasmas using Spiker-Sustainer Excitation," J. Appl. Phys. **99**, 113306 (2006). [See Appendix for reprint.] 5 Citations
4. N. Y. Babaeva, R. A. Arakoni and M. J. Kushner, "$O_2(^1\Delta)$ Production in High Pressure Flowing He/O_2 Plasmas: Scaling and Quenching", J. Appl. Phys. **101**, 123306 (2007). [See Appendix for reprint.]
5. R. A. Arakoni, N. Y. Babaeva and M. J. Kushner, "$O_2(^1\Delta)$ Production and Gain in Plasma Pumped Oxygen-Iodine Lasers: Consequences of NO and NO_2 Additives", J. Phys. D. **40**, 4793 (2007) [See Appendix for reprint.]

Interactions and Transitions:

Presentations at Conferences and Workshops (See Appendix for copies of presentations):

1. N. Yu Babaeva, R. A. Arakoni and M. J. Kushner, "Strategies for Higher Yields of $O_2(^1\Delta)$ at Higher Pressures for Electrical Excited Chemical Oxygen Iodine Lasers," Workshop on Electrically Excited COIL Lasers, Albuquerque, NM, May 2006. (Invited)
2. N. Y. Babaeva, R. Arakoni, and M. J. Kushner, "Excitation of $O_2(^1\Delta)$ in Pulsed Radio Frequency Flowing Plasmas for Chemical Oxygen Iodine Lasers," 58th Gaseous Electronics Conference, San Jose, CA, October 2005.
3. N. Yu. Babaeva, Ramesh A. Arakoni and M. J. Kushner, "Optimization of $O_2(^1\Delta)$ Yields in Pulsed RF Flowing Plasmas For chemical Oxygen Iodine Lasers," 33rd International Conference on Plasma Science, Traverse City, MI, June 2006.
4. R. Arakoni, Natalia Y. Babaeva and M. J. Kushner, "$O_2(^1\Delta)$ Production and Oxygen-Iodine Kinetics in Flowing Afterglows for Electrically Excited Chemical-Oxygen-Iodine Lasers," 59th Gaseous Electronics Conference, Columbus, OH, October 2006.

5. N. Y. Babaeva and M. J. Kushner, "$O_2(^1\Delta)$ Production in High Pressure Flowing He/O_2 Plasmas: Scaling and Quenching", 34th International Conference on Plasma Science, Albuquerque, NM June 2007.
6. R. A. Arakoni, N. Y. Babaeva and M. J. Kushner, "$O_2(^1\Delta)$ and $I(^2P_{1/2})$ Production in Flowing Afterglows for Oxygen-Iodine Lasers: Effect of NO/NO_2 Additives", 34th International Conference on Plasma Science, Albuquerque, NM June 2007.
7. N. Y. Babaeva, L. A. Garcia, R. A. Arakoni and M. J. Kushner, "Plasma Excited Chemical-Oxygen-Iodine Lasers: Optimizing Injection and Mixing for Positive Gain", 60th Gaseous Electronics Conference, Washington, DC, October 2007.

Technology Transfer:

During the period of performance, calculations and parameterizations were performed for other research groups under contract to AFRL/AFOSR for development of eCOIL systems. These computations were important to the design and scaling of experimental apparatus. The group we performed modeling for include:

1. CU-Aerospace, Inc.
2. Research Group of Prof. William Rich, Ohio State University

Appendix: Reprints of Publications and Presentations:

Journal Articles:

1. Natalia Yu. Babaeva, R. A. Arakoni and M. J. Kushner, "Production of $O_2(^1\Delta)$ in Flowing Plasmas Using Spiker-Sustainer Excitation", J. Appl. Phys. **99**, 113306 (2006).
2. R. A. Arakoni, N. Y. Babaeva and M. J. Kushner "$O_2(^1\Delta)$ Production and Gain in Plasma Pumped Oxygen-Iodine Lasers: Consequences of NO and NO_2 Additives", J. Phys. D **40**, 4793 (2007).
3. N. Y. Babaeva, R. A. Arakoni and M. J. Kushner "$O_2(^1\Delta)$ Production in High Pressure flowing He/O_2 Plasmas: Scaling and Quenching", J. Appl. Phys. **101**, 123306 (2007).

Conference Presentations:

4. N. Yu Babaeva, R. A. Arakoni and M. J. Kushner, "Strategies for Higher Yields of $O_2(^1\Delta)$ at Higher Pressures for Electrical Excited Chemical Oxygen Iodine Lasers," Workshop on Electrically Excited COIL Lasers, Albuquerque, NM, May 2006. (Invited)
5. N. Y. Babaeva, R. Arakoni, and M. J. Kushner, "Excitation of $O_2(^1\Delta)$ in Pulsed Radio Frequency Flowing Plasmas for Chemical Oxygen Iodine Lasers," 58th Gaseous Electronics Conference, San Jose, CA, October 2005.
6. N. Yu. Babaeva, Ramesh A. Arakoni and M. J. Kushner, "Optimization of $O_2(^1\Delta)$ Yields in Pulsed RF Flowing Plasmas For chemical Oxygen Iodine Lasers," 33rd International Conference on Plasma Science, Traverse City, MI, June 2006.
7. R. Arakoni, Natalia Y. Babaeva and M. J. Kushner, "$O_2(^1\Delta)$ Production and Oxygen-Iodine Kinetics in Flowing Afterglows for Electrically Excited Chemical-Oxygen-Iodine Lasers," 59th Gaseous Electronics Conference, Columbus, OH, October 2006.
8. N. Y. Babaeva and M. J. Kushner, "$O_2(^1\Delta)$ Production in High Pressure Flowing He/O_2 Plasmas: Scaling and Quenching", 34th International Conference on Plasma Science, Albuquerque, NM June 2007.
9. R. A. Arakoni, N. Y. Babaeva and M. J. Kushner, "$O_2(^1\Delta)$ and $I(^2P_{1/2})$ Production in Flowing Afterglows for Oxygen-Iodine Lasers: Effect of NO/NO_2 Additives", 34th International Conference on Plasma Science, Albuquerque, NM June 2007.
10. N. Y. Babaeva, L. A. Garcia, R. A. Arakoni and M. J. Kushner, "Plasma Excited Chemical-Oxygen-Iodine Lasers: Optimizing Injection and Mixing for Positive Gain", 60th Gaseous Electronics Conference, Washington, DC, October 2007.

JOURNAL OF APPLIED PHYSICS **99**, 113306 (2006)

Production of $O_2(^1\Delta)$ in flowing plasmas using spiker-sustainer excitation

Natalia Y. Babaeva[a]
Department of Electrical and Computer Engineering, Iowa State University, Ames, Iowa 50011

Ramesh A. Arakoni[b]
Department of Aerospace Engineering, University of Illinois, Urbana, Illinois 61801

Mark J. Kushner[c]
Department of Electrical and Computer Engineering, Iowa State University, Ames, Iowa 50011

(Received 3 December 2005; accepted 2 March 2006; published online 9 June 2006)

In chemical oxygen iodine lasers (COILs), oscillation at 1.315 μm in atomic iodine ($^2P_{1/2} \rightarrow {}^2P_{3/2}$) is produced by collisional excitation transfer of $O_2(^1\Delta)$ to I_2 and I. Plasma production of $O_2(^1\Delta)$ in electrical COILs (eCOILs) eliminates liquid phase generators. For the flowing plasmas used for eCOILs (He/O_2, a few to tens of torr), self-sustaining electron temperatures, T_e, are 2–3 eV whereas excitation of $O_2(^1\Delta)$ optimizes with $T_e = 1-1.5$ eV. One method to increase $O_2(^1\Delta)$ production is by lowering the average value of T_e using spiker-sustainer (SS) excitation where a high power pulse (spiker) is followed by a lower power period (sustainer). Excess ionization produced by the spiker enables the sustainer to operate with a lower T_e. Previous investigations suggested that SS techniques can significantly raise yields of $O_2(^1\Delta)$. In this paper, we report on the results from a two-dimensional computational investigation of radio frequency (rf) excited flowing He/O_2 plasmas with emphasis on SS excitation. We found that the efficiency of SS methods generally increase with increasing frequency by producing a higher electron density, lower T_e, and, as a consequence, a more efficient production of $O_2(^1\Delta)$. [DOI: 10.1063/1.2199387]

I. INTRODUCTION

Chemical oxygen iodine lasers are being investigated because of their optical fiber deliverable wavelength (1.315 μm), highly scalable continuous wave (cw) power, and favorable material interaction properties.[1–6] Operation of the chemical oxygen iodine laser (COIL) is based on an electronic transition between the spin-orbit levels of the ground state configuration of the iodine atom $I(^2P_{1/2}) \rightarrow I(^2P_{3/2})$ where the upper level is populated by near resonant energy transfer (quantum defect ~219 cm^{-1}) from $O_2(^1\Delta)$ to ground state $I(^2P_{3/2})$. The COIL generates ground state I by dissociative excitation transfer from $O_2(^1\Delta)$ to I_2.

Typically, $O_2(^1\Delta)$ is produced in an external chemical reactor by a gas-liquid reaction between gaseous chlorine and a basic hydrogen peroxide solution[7] producing yields approaching 100% of the oxygen emerging in the $O_2(^1\Delta)$ state. The long lifetime of $O_2(^1\Delta)$ (60 min) and robustness against quenching enables transport over long distances to the laser cavity. There are many system issues having to do with weight, safety, and the ability to rapidly modulate the production of the $O_2(^1\Delta)$ which have motivated investigations into methods to produce the precursor $O_2(^1\Delta)$ using flowing electric discharges and so produce a purely electrical excited laser (eCOIL).[8,9] Recent and ongoing investigations have shown that substantial yields of $O_2(^1\Delta)$ can be generated by an appropriately tailored electric discharge, typically in mixtures with rare gas diluents such as He.[10–22] Recently, positive gain was reported in atomic iodine resulting from electric discharge produced $O_2(^1\Delta)$,[23,24] followed by laser demonstrations.[25,26]

Much of the development of eCOIL has focused on efficiently generating $O_2(^1\Delta)$ by engineering the operating E/N (electric field/gas number density) of the discharge to be closer to the optimum value for exciting $O_2(^1\Delta)$. To maximize the fraction of discharge power that is directly dissipated in the electron-impact excitation of $O_2(^1\Delta)$, the electron temperature, T_e, should be near 1.2 eV, which corresponds to an E/N of ≈ 10 Townsend [1 Townsend (Td) $= 10^{-17}$ V cm^2]. Self-sustained discharges in He/O_2 mixtures operate at least a few tens of Td.[27]

One of the methods to reduce the time averaged electron temperature is to use a pulsed discharge analogous to that proposed in Refs. 12 and 17. In these devices a short, high power pulse (the spiker) is followed by a longer period of lower power (the sustainer) before applying another high power pulse. The duration of the high power pulse should be long enough for T_e to spike and for the gas to avalanche, producing an electron density in excess of the steady-state value. The high power pulse should be short enough so that the discharge does not come into a quasi-steady-state. If there is sufficient excess ionization during the period of lower power deposition, there may be an extended period where T_e falls below the self-sustaining value, T_{eo}, which for He/O_2 mixtures enables a more efficient production of $O_2(^1\Delta)$. The duty cycle of the spiker and the length of the sustainer should be chosen so that the average value of electron temperature $\bar{T}_e < T_{eo}$. The optimum length of the sus-

---

[a] Electronic mail: natalie5@iastate.edu
[b] Electronic mail: arakoni@uiuc.edu
[c] Author to whom correspondence should be addressed; electronic mail: mjk@iastate.edu

tainer is then largely determined by the time required for the electron density to decrease to its steady-state value, thereby increasing T_e towards T_{eo}. This method for engineering T_e is often referred to as spiker-sustainer (SS) excitation.

In previous work, the scaling of production of $O_2(^1\Delta)$ was computationally investigated using global-kinetics[19] one-dimensional,[20] and two-dimensional models.[21] It was found that the yield of $O_2(^1\Delta)$ generally scaled linearly with energy deposition for moderate loadings (a few eV/O_2 molecule) up to 5–8 eV/molecule. Energy deposition beyond those values produced excess dissociation which ultimately reduced yield. Initial scaling studies of SS excitation methods, discussed in Ref. 20, suggested that under ideal conditions, as are represented by global models, $O_2(^1\Delta)$ yields approaching 30% might be possible using SS methods. In this work, we computationally investigate SS methods for optimizing $O_2(^1\Delta)$ using a two-dimensional (2D) model that more realistically represents the electrical circuitry, electrode losses, uniformity and flow considerations. In particular, we investigated capacitively coupled radio frequency (rf) excited systems in He/O_2 mixtures. We found that SS methods do hold the potential for increasing $O_2(^1\Delta)$ yields above that for cw excitation for the same average power, though the amount of the increases is less than that suggested by the global models.

The model and reaction mechanism are briefly described in Sec. II. The results from our investigation are discussed in Sec. III where yields and efficiency of $O_2(^1\Delta)$ production are compared for cw and SS excitations for rf carrier frequencies of 13, 27, and 40 MHz. Optimization of $O_2(^1\Delta)$ production using the SS technique is discussed in Sec. IV. Concluding remarks are in Sec. V.

II. DESCRIPTION OF THE MODEL

The model used in this study, nonPDPSIM, is a multifluid 2D hydrodynamics simulation in which transport equations for all charged and neutral species and Poisson's equation are integrated as a function of time. nonPDPSIM is described in detail in Ref. 28. Poisson's equation [Eq. (1)], transport equations for conservation of the charged species [Eq. (2)], and the surface charge balance equation [Eq. (3)] are simultaneously integrated using a Newton iteration technique,

$$-\nabla\cdot(\varepsilon_0\varepsilon_r\nabla\Phi)=\sum_j N_j q_j+\rho_s, \tag{1}$$

$$\frac{\partial N_j}{\partial t}=-\nabla\cdot\boldsymbol{\Gamma}_j+S_j, \tag{2}$$

$$\frac{\partial\rho_s}{\partial t}=\sum_j q_j(-\nabla\cdot\boldsymbol{\Gamma}_j+S_j)-\nabla\cdot[\sigma(-\nabla\Phi)]. \tag{3}$$

Here ε_0, ε_r, Φ, ρ_s, N_j, $\boldsymbol{\Gamma}_j$, σ, S_j, and q_j are the permittivity of free space, dielectric constant, electric potential, surface charge density, conductivity of solid materials, sources, and charge, respectively. The subscripts j denote gas-phase species. Updates of the charged particle densities and electric potential are followed by an implicit update of the electron temperature by solving the electron energy equation for average energy ε,

$$\frac{\partial(n_e\varepsilon)}{\partial t}=q\boldsymbol{\Gamma}_e\cdot\mathbf{E}-n_e\sum_j N_j\kappa_j-\nabla\cdot\left(\frac{5}{2}\varepsilon\boldsymbol{\Gamma}_e-\lambda_e\nabla T_e\right), \tag{4}$$

where $\frac{3}{2}kT_e=\varepsilon$. The terms in Eq. (4) are for the contribution from Joule heating, summation of elastic and inelastic impact processes with heavy neutrals and ions with energy loss κ_j, and electron heat flux consisting of terms for electron energy flux (Γ_e) and a conduction (λ_e is the electron thermal conductivity). The electron transport coefficients and rate coefficients for bulk electrons as a function of T_e are obtained by solving the zero-dimensional Boltzmann's equation for the electron energy distribution to capture the non-Maxwellian nature of the electron swarm. These values are stored in a tabular form and interpolated during execution of the code. The tables are periodically updated to reflect changes in species densities. These updates are then followed, in a time splicing manner, with an implicit update of neutral particle densities.

The fluid averaged advective velocity $\mathbf{v}$ is obtained by solving a modified form of the compressible Navier-Stokes equations in which momentum transfer from ion and electron collisions and acceleration by the electric field are included in the momentum equation, and Joule heating is included in the energy equations,

$$\frac{\partial\rho}{\partial t}=-\nabla\cdot(\rho\mathbf{v})+(\text{inlets, pumps}), \tag{5}$$

$$\frac{\partial(\rho\mathbf{v})}{\partial t}=-\nabla p-\nabla\cdot(\rho\mathbf{v}\mathbf{v})-\nabla\cdot\boldsymbol{\tau}+\sum_j(q_jN_j-M_j\mu_jS_j)\mathbf{E}, \tag{6}$$

$$\frac{\partial(\rho c_pT)}{\partial t}=-\nabla(-\kappa\nabla T+\rho\mathbf{v}c_pT)+\sum_j\mathbf{j}_j\cdot\mathbf{E}-\sum_i R_i\Delta H_i+p\nabla\cdot\mathbf{v}. \tag{7}$$

Here ρ is the total mass density, p is the thermodynamic pressure, $\boldsymbol{\tau}$ is the viscosity tensor, c_p is the heat capacity, κ is the species averaged thermal conductivity, μ is the mobility, and M the molecular weight. The subscripts j are for summations over species. ΔH_i is the change in enthalpy due to reaction i having total rate R_i. The reactions include Frank-Condon heating from electron-impact dissociation of molecules as well as conventional chemical reactions. The sums (other than for reactions) are over all charged and neutral species. The contributions to momentum from charged particles include those of electrons. The contributions to the energy equation from Joule heating include contributions from ions. The heat transfer from electrons is included as a collisional change in enthalpy. The relationship among pressure, density, and temperature is given by the ideal-gas law. The contributions to momentum due to charged particle transport assume that the collision frequencies with electrons and ions are large compared to the time rate of change in the electric field, and so there is little momentum that is instantaneously stored in the charged particles.[29]

The reaction mechanism for He/O_2 plasmas used here is essentially the same as that described in Refs. 19–21, and involves reactions in the gas-phase discharge and afterglow as well as recombination and quenching reactions on the discharge tube walls. The species in the model are ground state neutrals O_2, O, O_3, and He; vibrationally excited $O_2(v)$ (representing the total vibrational population consisting of the first four vibrational levels of O_2); electronic states $O_2(^1\Delta)$, $O_2(^1\Sigma)$, $O(^1D)$, $O(^1S)$, and $He(^2S)$; and ions O_2^+, O^+, O_2^-, O^-, O_3^-, and He^+.

The states of primary interest, the precursors to the eCOIL, are $O_2(^1\Delta)$ (0.97 eV) and $O_2(^1\Sigma)$ (1.6 eV), which are dominantly produced in the discharge region by direct electron impact with the ground state,

$$e + O_2 \rightarrow O_2(^1\Delta) + e, \tag{8}$$

$$e + O_2 \rightarrow O_2(^1\Sigma) + e. \tag{9}$$

Production of $O_2(^1\Sigma)$ generally also results in generation of $O_2(^1\Delta)$ through rapid collisional quenching reactions with atomic oxygen O. The atomic oxygen is dominantly produced by electron-impact dissociation of O_2,

$$e + O_2 \rightarrow O + O + e, \tag{10}$$

$$O + O_2(^1\Sigma) \rightarrow O + O_2(^1\Delta). \tag{11}$$

Note that the $O_2(^1\Sigma)$ and $O_2(^1\Delta)$ states have radiative lifetimes of 12 s and approximately 1 h. These states are only nominally quenched by collisions with species other than electrons for the conditions of interest although at higher pressures quenching of $O_2(^1\Delta)$ by O_3 becomes important. These electron collisions are, in order of importance, superelastic relaxation, dissociative excitation, and ionization. Other channels for $O_2(^1\Sigma)$ production (although less important for the conditions of interest) are through production and quenching of $O(^1D)$,

$$e + O_2 \rightarrow O(^1D) + O + e, \tag{12}$$

$$e + O \rightarrow O(^1D) + e, \tag{13}$$

$$O(^1D) + O_2 \rightarrow O + O_2(^1\Sigma). \tag{14}$$

The generation of $O_2(^1\Sigma)$ in these reactions is then followed by quenching by O to $O_2(^1\Delta)$. As the density of $O_2(^1\Delta)$ increases to the many percent level, losses to upper electronic states, superelastic deexcitation to the ground state, and dissociation begin to become important.

$$e + O_2(^1\Delta) \rightarrow O_2(^1\Sigma) + e, \tag{15}$$

$$e + O_2(^1\Delta) \rightarrow O_2 + e, \tag{16}$$

$$e + O_2(^1\Delta) \rightarrow O + O + e, \tag{17}$$

$$e + O_2(^1\Delta) \rightarrow O(^1D) + O + e. \tag{18}$$

The $O_2(^1\Delta)$ then persists far into the afterglow due to its long radiative lifetime, where the most significant quenching mechanism is through collisions with O atoms,

$$O + O_2(^1\Delta) \rightarrow O_2 + O. \tag{19}$$

At this point energy pooling and quenching reactions with $O_2(^1\Delta)$ and O_3 also begin to reduce $O_2(^1\Delta)$ yields, though not significantly for our conditions. The rate of quenching $O_2(^1\Delta)$ by collisions with the walls is uncertain due to the variability of the quenching probability with temperature and conditions of the wall. Based on estimates for similar conditions, we have assigned a wall quenching coefficient of 10^{-5}, which is insignificant for typical eCOIL conditions.

The effective yield of $O_2(^1\Delta)$ is defined as the ratio of the combined $O_2(^1\Delta)$ and $O_2(^1\Sigma)$ densities to the sum of the densities of all oxygen-containing species on a molecular O_2 basis,

$$Y = \frac{[O_2(^1\Delta) + O_2(^1\Sigma)]}{\{[O_2] + [O_2(^1\Delta)] + [O_2(^1\Sigma)] + 0.5[O] + 1.5[O_3]\}}. \tag{20}$$

This choice of yield was made with the prior knowledge that the majority of $O_2(^1\Sigma)$ is quenched directly to $O_2(^1\Delta)$. As such, Eq. (20) is the most relevant for the best case energy scaling.

III. CONTINUOUS WAVE AND SPIKER-SUSTAINER EXCITATIONS

A schematic of the idealized eCOIL device we modeled is shown in Fig. 1. A $He/O_2=70/30$ mixture is flowed through a quartz tube 60 cm in length and 6 cm in diameter at 3 Torr. A rf electric discharge is operated between two ring electrodes 2 cm wide with centers separated by 13 cm. The electrodes are powered up to a few hundred watts at 13.56, 27, or 40 MHz. The flow rate of 6 lpm corresponds to an average axial inlet speed of 985 cm/s. Our investigations were limited to the region of the reactor prior to supersonic expansion and injection of I_2. The numerical grid uses an unstructured, cylindrically symmetric mesh with triangular elements. The wall temperature was held fixed at 300 K assuming active water-jacket cooling (not included in the mesh).

A. Continuous wave excitation

As a point of departure and to provide a basis of comparison, $O_2(^1\Delta)$ production in a flowing afterglow using cw rf capacitive excitation will be discussed. The base case operating conditions are $He/O_2=70/30$, 3 Torr, flow rate of 6 lpm, inlet gas temperature of 300 K, and power deposition of 40 W with a rf of 13.56 MHz.

Power deposition, electron temperature (T_e), and electron density (n_e) for the base case are shown in Fig. 2(a). Values are shown averaged over the rf cycle. Power deposition is peaked just off axis with a maximum of 0.2 W/cm^3. The peak value of T_e of 2.9 eV is near the upstream electrode where the electron density is low. T_e drops to 2.2 eV where the electron density is maximum at about 9.8×10^9 cm^{-3} and where the majority of the $O_2(^1\Delta)$ is produced. The region of elevated T_e extends significantly beyond the rf electrodes

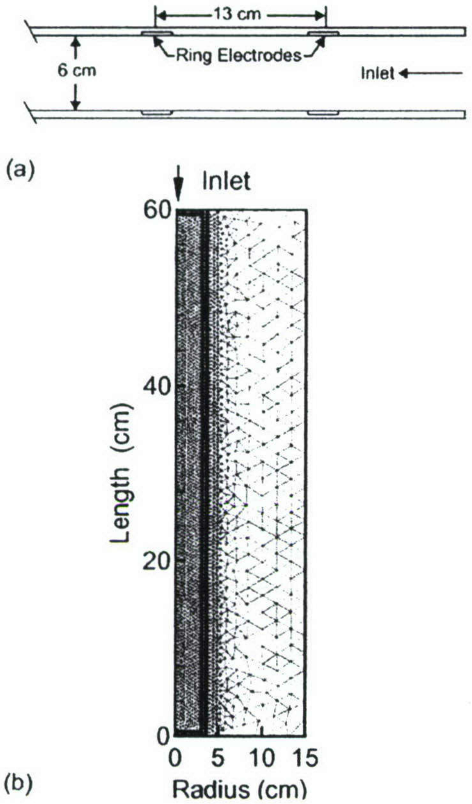

FIG. 1. Schematic of the cylindrical discharge tube. (a) Close-up showing ring electrodes and (b) complete computational domain showing the numerical mesh. The flow enters uniformly from the right (or top) where pressure, speed, and temperature are specified. The walls are held at constant temperature and mass flux is conserved at the outlet. Boundary conditions for solution of Poisson's equation require the extension of computational domain beyond the tube.

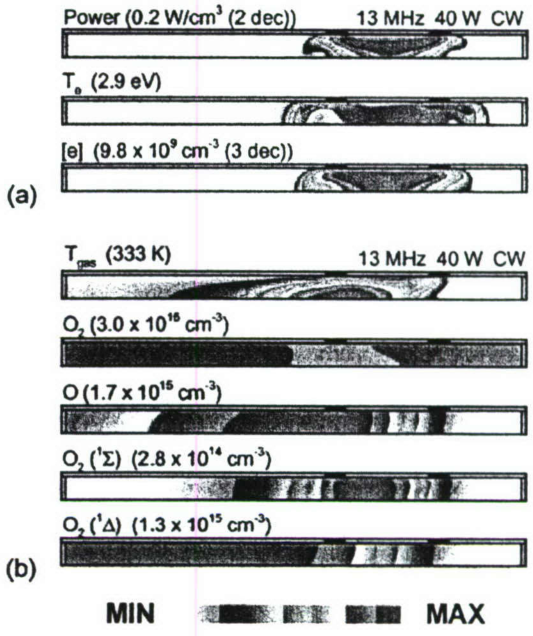

FIG. 2. (Color) Plasma properties and species densities for the base case conditions ($He/O_2=70/30$, 3 Torr, 6 lpm, 40 W) when using cw excitation at 13.56 MHz. (a) Power deposition, electron temperature, and electron densities; and (b) gas temperature and densities of O_2, O, $O_2(^1\Sigma)$, and $O_2(^1\Delta)$. All values are averaged over one rf period. The flow is from the right. The scales are linear with zero minimum values with the exception of T_{gas} unless the number of decades (i.e., "decs") is indicated for log plots. The maximum value is indicated in each figure. Depletion in ground state O_2 is due to gas heating by the localized power deposition. $O_2(^1\Delta)$ maximizes downstream in part due to quenching of $O_2(^1\Sigma)$.

(upstream and downstream) due to the large electron thermal conductivity and gas flow which entrains ions through their large momentum transfer. Although the electrons transfer little momentum to or from the gas, the electrons are pulled by the ions in the downstream direction through the ambipolar electric field. The electron density is as large as 10^9 cm^{-3}, a few centimeters ahead of the upstream electrode due to thermal conduction and diffusion of electrons against the advective flow and some local ionization. The steep rise in electron density at this point marks the front end of the reactive plasma zone. The same action occurs on the downstream side of the discharge. With diffusion now in the direction of the advective flow, the length of the afterglow is extended. The downstream extension of the plasma zone is aided by rarefaction of the gas downstream of the electrodes that provides for more rapid charge particle diffusion, and dissociation of O_2 that reduces the rate of loss of electrons by dissociative attachment.

Gas temperature, T_g, and densities of O_2, O, $O_2(^1\Sigma)$, and $O_2(^1\Delta)$ are shown in Fig. 2(b) for the base case. T_g increases by 33 K above ambient by Joule and Frank-Condon heating. The peak in the gas temperature is shifted downstream by the gas flow. Heating occurs primarily near the electrodes where the electric field is largest (see the local peak in T_g near the upstream electrode) and secondarily off axis in the bulk plasma where the ion density is largest. Thermal conduction and heat transfer at the walls shift the peak in T_g to the center of the tube. The gas returns to near ambient values at the exit.

Dissociation and excitation processes contribute to depletion of ground state O_2 in addition to that due to rarefaction by gas heating. Electron-impact dissociation produces about 6% of the depletion with an additional 5% coming from electron-impact excitation to $O_2(^1\Delta)$ and $O_2(^1\Sigma)$. The density of O atoms peaks 26 cm downstream, decreasing thereafter due to recombination on the walls, and three-body association reactions in the gas phase to form O_2 and O_3. The density of $O_2(^1\Sigma)$ peaks in the plasma zone where production is largest. As the density of O atoms increases, $O_2(^1\Sigma)$ is rapidly quenched to $O_2(^1\Delta)$ by collisions with O atoms in the flow direction after the discharge. After the $O_2(^1\Sigma)$ is converted to $O_2(^1\Delta)$, the density of $O_2(^1\Delta)$ only moderately decreases along the tube due to quenching. Excited states of O_2 and atomic O also extend 5–10 cm upstream of the electrodes, a consequence of the plasma extending upstream and back diffusion against the flow.

The combined yields of $O_2(^1\Delta)$ and $O_2(^1\Sigma)$ on axis for cw excitation are shown in Fig. 3 for different powers but for otherwise the base case conditions. The yield is maximum at the edge of the plasma zone near the downstream electrode. The yield is nearly constant thereafter, only slowly decreasing due to heavy particle quenching. Yields increase linearly with lower power deposition and begin to saturate at high powers. This is due to increased power losses to the elec-

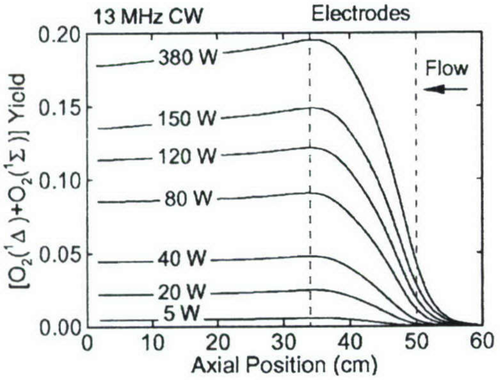

FIG. 3. Combined yield of $O_2(^1\Delta)$ and $O_2(^1\Sigma)$ along the axis of the tube ($He/O_2=70/30$, 3 Torr, 6 lpm) at 13.56 MHz for different powers. The flow is from the right. Maximum yields occur within the range of the electrodes. Yields scale linearly with lower power deposition and begin to saturate at high powers.

trodes, principally ion acceleration, typical for capacitive discharges. For example, for 40 W (specific energy deposition of 0.31 eV/O_2), the yield is about 4.5% at the exit of the tube or an efficiency of 0.15 $O_2(^1\Delta)$ molecules/eV of energy deposition. For 340 W (specific energy deposition of 2.95 eV/O_2), the yield is 19.5% at the end of the plasma zone and 18% at the exit of the tube, an efficiency of 0.04 $O_2(^1\Delta)$ molecules/eV.

B. Spiker-sustainer excitation

cw self-sustained discharges require that the sources of ionization and charged particle loss be equal. For moderate pressure mixtures of He/O_2, this translates into a balance between electron-impact ionization and electron loss by dissociative attachment to O_2 which requires $T_e=2-3$ eV. Unfortunately, the value of T_e at which power dissipation into excitation of $O_2(^1\Delta)$ and $O_2(^1\Sigma)$ is maximum is about 1–1.5 eV. This value is largely independent of gas mixtures as it is determined by the values of the excitation cross sections. As such, significant efforts have been expended in using gas additives to lower the E/N of the discharge so that T_e is 1–1.5 eV. In most cases, these values are inaccessible to self-sustained electric discharges. In SS systems for eCOIL applications, the discharge parameters are selected so that a significant fraction of the power deposition occurs at T_e below self-sustaining so that the rates of direct electron-impact excitation of $O_2(^1\Delta)$ and $O_2(^1\Sigma)$ are maximized.

Lowering the time averaged T_e to match the cross sections of desired excited states is a well known strategy. For example, externally sustained electric discharges, such as electron beam sustained discharges (EBSDs), have long been used to excite CO_2 lasers in $He/N_2/CO_2$ mixtures.[30] The self-sustaining E/N and T_e of these mixtures typically exceed that which optimizes excitation into the upper laser level, either by direct electron-impact vibrational excitation of CO_2 or through excitation transfer from $N_2(v=1)$. The external ionization provided by the electron beam enables the E/N provided by the discharge, for a given power deposition, to be below the self-sustaining value and be a better match to vibrational excitation of CO_2 and N_2. The disadvantage of this approach is the added complication and expense of the electron beam hardware. EBSD production of $O_2(^1\Delta)$ was investigated by Ionin *et al.*[13]

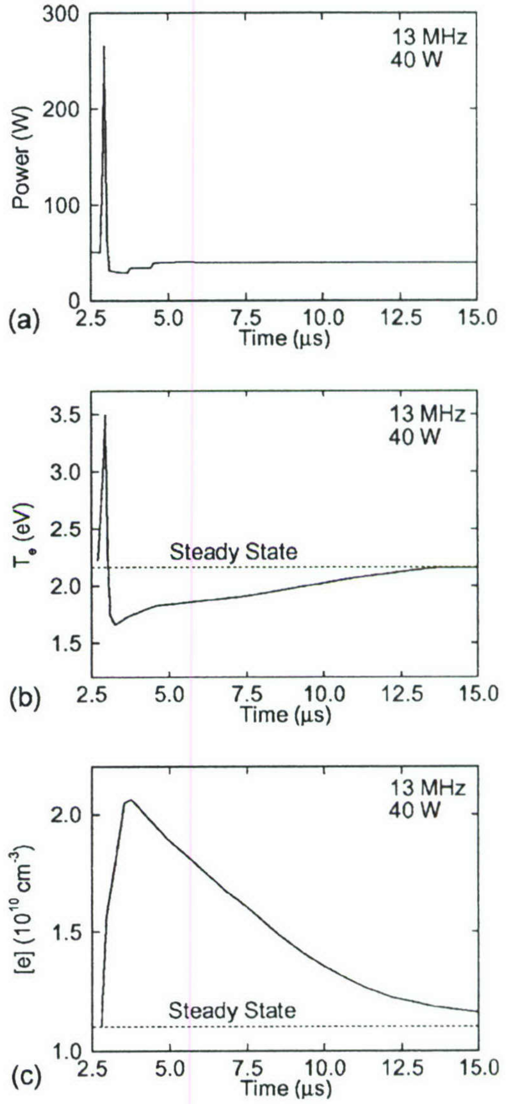

FIG. 4. Plasma properties when the He/O_2 gas mixture at 3 Torr is excited by a single spiker pulse. (a) Power deposition, (b) electron density, and (c) electron temperature. The excess electron density produced by the spiker enables the electron temperature to decrease to a more optimum value for excitation of $O_2(^1\Sigma)$. After the pulse the steady-state level is regained after 15–20 μs.

The SS technique attempts to achieve the same ends as the EBSD while using, in principle, a single discharge apparatus. Using the SS technique, the excess ionization provided by the spiker enables the E/N and T_e during the sustainer period, for a given time averaged power deposition, to be below self-sustaining similar to the EBSD. The excess ionization in the SS technique is provided *in situ* and, unlike the EBSD, is transient. That is, the discharge will eventually recover to a steady, self-sustaining state having a larger T_e.

The SS method we are investigating consists of pulsed modulated rf excitation; a series of high power rf pulses followed by a period of lower power rf excitation. As a point of departure, plasma properties during a single spiker pulse fol-

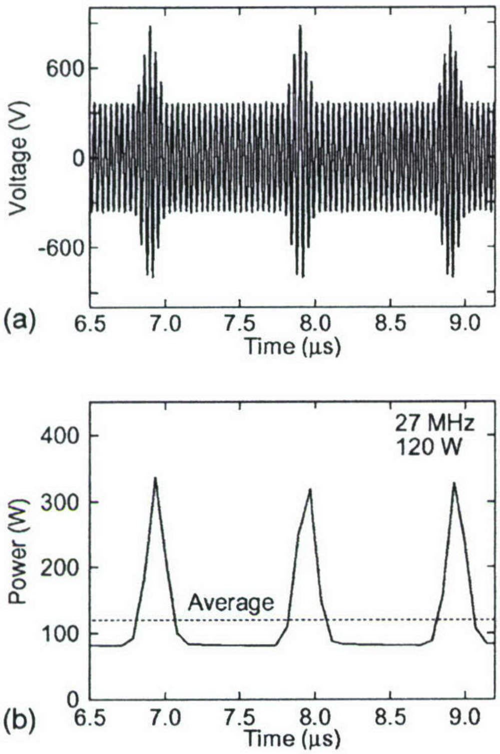

FIG. 5. Typical values of (a) voltage, and (b) power for SS excitation with 1 MHz repetition rate. The carrier frequency is 27 MHz. The V_{SS}/V_{cw} ratio is 5/2. Power is 120 W when averaged over a SS period (1 μs).

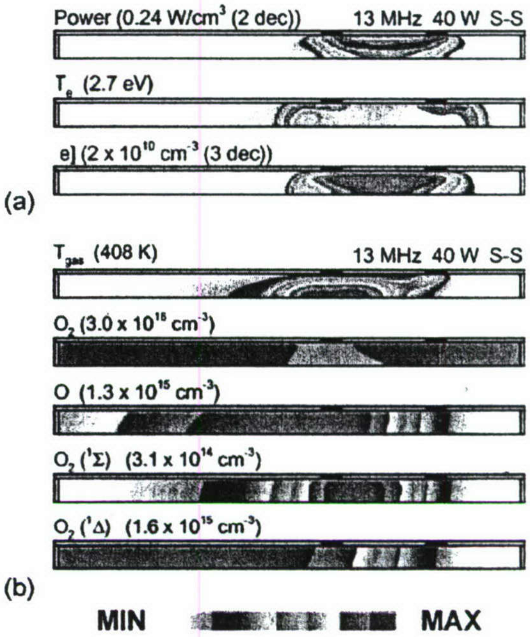

FIG. 6. (Color) Plasma properties and species densities for the base case conditions ($He/O_2=70/30$, 3 Torr, 6 lpm, 40 W) when using SS excitation at 13.56 MHz with a duty cycle of 20%. (a) Power deposition, electron temperature, and electron density; and (b) gas temperature and densities of O_2, O, $O_2(^1\Sigma)$, and $O_2(^1\Delta)$. All values are averaged over one SS period. Labeling is the same as in Fig. 2. The flow is from the right. With SS excitation the electron temperature is lower and maximum electron density higher compared with cw excitation.

lowed by a long sustainer period will be described. Using the base case conditions, the discharge, which is first operated in a steady state at 40 W, is then excited by a single short high power pulse of 270 W of duration of 200 ns and is then followed by a (sustainer) period of 40 W. The resulting power, and n_e and T_e on axis midway between the electrodes (approximately at the peak plasma density) are shown in Fig. 4 as a function of time. The spiker pulse avalanches n_e to values as high as 2.1×10^{10} cm^{-3} above the steady-state value of $n_{eo}=1.1\times10^{10}$ cm^{-3}. As recombination and attachment consume the excess ionization, n_e decreases towards n_{eo} over a period of 15–20 μs. The quasi-steady-state electron temperature is $T_{eo}=2.1$ eV. T_e increases during the spiker to avalanche the gas, thereby creating excess ionization and then decreases below T_{eo} after the spiker pulse terminates. As long as n_e is above n_{eo} then T_e is below T_{eo}, falling to as low as 1.6 eV. As the electron density decays towards n_{eo}, then T_e increases towards T_{eo}. These lower values of T_e, coupled with the excess ionization, have the potential to increase the production of $O_2(^1\Delta)$.

Typical voltage and power wave forms for a discharge operating in a SS mode for a time averaged power of 120 W are shown in Fig. 5. The conditions are otherwise the same as the base case. Excess ionization is provided by means of a high voltage spiker pulse (V_{SS}) of 200 ns duration repeated at 1 MHz at the carrier frequency of 27 MHz yielding a duty cycle of 20%. In between the spiker pulses, the plasma is sustained by a cw rf voltage (V_{cw}). The choices of $V_{SS}/V_{cw}=5/2$ and the triangular spiker pulse shape are somewhat arbitrary and have not been optimized for maximum yield of $O_2(^1\Delta)$. Power is averaged over the full SS period of 1 μs and the voltages V_{SS} and V_{cw} are adjusted to maintain the total time averaged power deposition at the specified value. Typically up to 15—20 (15–20 μs) of SS periods were simulated in order for the system to come into a pulse-periodic steady state. For the results in Fig. 5 (time averaged power of 120 W) the power during the spiker reaches 320 W with a peak $V_{SS}=900$ V resulting in the power during the sustainer being approximately 90 W with $V_{cw}=360$ V.

Time averaged plasma properties and species densities for the base case conditions when using SS (duty cycle 20%, $V_{SS}/V_{cw}=5/2$, 1 MHz repetition rate, and 13.56 MHz carrier frequency) are shown in Fig. 6 for 40 W average power. Values have been averaged over the entire 1 μs SS period. (Compare these results to Fig. 2 for cw excitation.) With SS excitation, the time averaged T_e is lower in the volume where the electron density is maximum while the time averaged n_e is larger. With SS excitation, the time averaged $T_e=1.7$ eV where n_e is maximum whereas with cw excitation, $T_e=2.2$ eV. The T_e remains near its cw value adjacent to the electrodes where sheath heating dominates. The time averaged maximum value of n_e increases from 9.8×10^9 cm with cw excitation to 2×10^{10} cm^{-3} with SS excitation. The decrease in T_e and increase in n_e are both favorable for more efficient $O_2(^1\Delta)$ production. The relative spatial distributions of species densities [O, O_2, $O_2(^1\Delta)$, and $O_2(^1\Sigma)$] do not significantly differ from the cw case. The exception is the spatial distribution of T_g that has more localized heating at the electrodes.

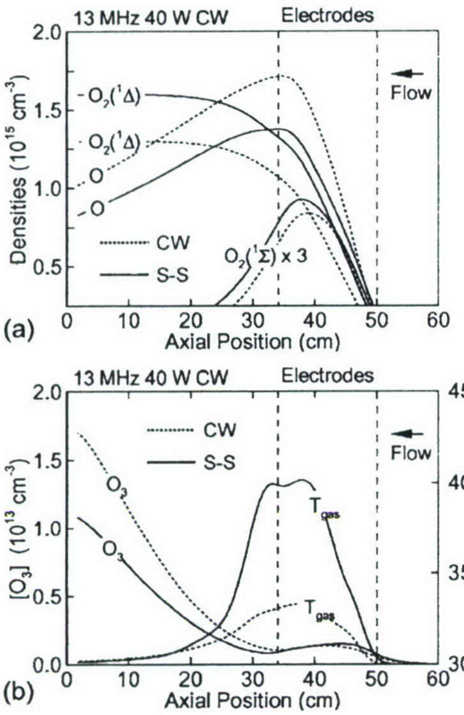

FIG. 7. Oxygen atomic and molecular densities (a) and gas temperature (b) along the axis for the base case conditions (He/O_2=70/30, 3 Torr, 6 lpm, 40 W) when using cw (dotted line) and SS (solid line) excitations. The flow is from the right. The degree of dissociation decreases and $O_2(^1\Delta)$ production increases with SS excitation.

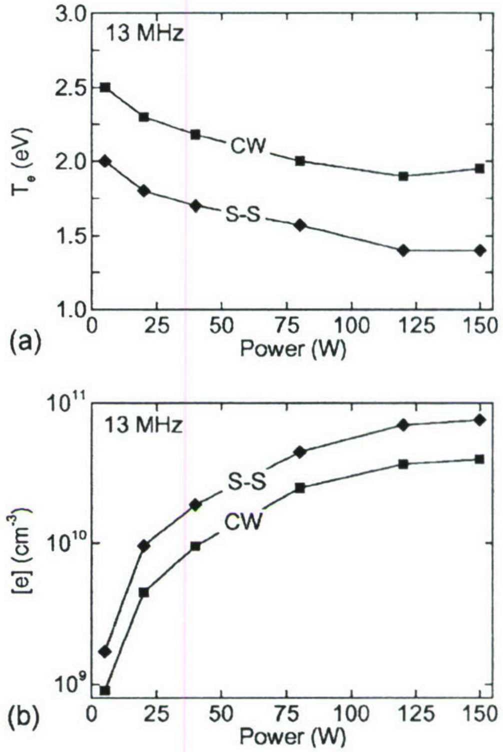

FIG. 8. Plasma parameters as a function of power for cw and SS excitations. (a) Electron temperature and (b) peak electron density. The electron temperature is measured at the location of peak electron density. The values are averaged over a SS period of 1 μs.

Time averaged species densities and gas temperature on the axis of the tube are compared for cw and SS excitations in Fig. 7. With SS excitation, the lower value of T_e results in less electron-impact dissociation of O_2, producing a smaller density of O atoms, while increasing the rate of excitation $O_2(^1\Delta)$. The contribution of quenching of $O_2(^1\Sigma)$ to production of $O_2(^1\Delta)$ by collisions with O atoms is about 20%. This quenching is somewhat more rapid in the cw case due to the larger density of O atoms. The production of O_3 is also larger in the cw case due to the larger production of O atoms, as shown in Fig. 7(b). The peak gas temperature is 400 K with SS excitation, whereas with cw excitation the peak T_g is only about 333 K. This is counterintuitive as the smaller amount of Frank-Condon heating due to there being less dissociation with SS excitation should produce a lower T_g. The larger time averaged value of n_e and lower value T_e obtained with SS excitation produce more vibrationally excited O_2 that undergoes *V-T* relaxation and more charge exchange heating. As a result, T_g increases with SS excitation.

The time averaged n_e and T_e at the location of the maximum electron density are shown in Fig. 8 as a function of power for cw and SS excitations. For powers between 10 and 150 W, T_e is approximately 0.5 eV lower with SS excitation compared to cw excitation, while the electron density is approximately a factor of 2 larger. Note that with increases in power, T_e decreases for both cw and SS excitations. This results from the larger degree of dissociation of O_2 and larger density of excited states. The larger dissociation of O_2 results in there being less dissociative attachment and fewer electron losses, and so a smaller T_e is required to sustain the discharge. The larger excited state densities enable a larger rate of multistep ionization which also allows for a smaller value of T_e.

Atomic oxygen and $O_2(^1\Delta)$ densities on axis for 40 and 120 W are shown in Fig. 9. The exit density of $O_2(^1\Delta)$ increases with SS compared to cw excitation whereas the O atom density decreases. The location of the maximum O atom density progressively moves downstream with increasing power due in large part to the increasing gas temperature, rarefaction, and extension of the plasma zone.

The combined yields of $O_2(^1\Delta)$ and $O_2(^1\Sigma)$ along the axis and at the exit of the tube for cw and SS excitations for different powers are shown in Fig. 10. The efficiency of production of $O_2(^1\Delta)$, molecules/eV of energy deposition, is also shown. For these discharge parameters, yields are typically higher for SS excitation for low powers and converge at higher powers (150 W). For example, at low power (20 W) the energy deposition required to produce one $O_2(^1\Delta)$ molecule is 7.3 eV for cw and 5.6 eV for SS excitation, netting a 30% improvement in $O_2(^1\Delta)$ yield. This improvement in yield diminishes as the total power is increased until, for these conditions, the advantage of SS excitation is lost for a power of 120 W. The decrease in improvement using the SS is likely the natural decrease in T_e that occurs when increasing power with cw excitation, as shown in Fig. 8. As T_e decreases towards 1 eV, the improvement in efficiency of exciting $O_2(^1\Delta)$ obtained by lowering T_e another 0.5 eV with SS excitation is diminished.

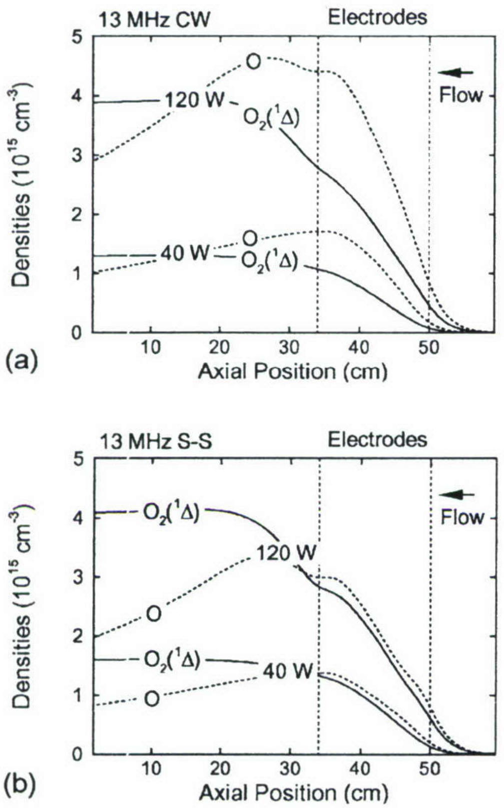

FIG. 9. Atomic oxygen and $O_2(^1\Delta)$ along the axis for 40 and 120 W. (a) cw and (b) SS. The flow is from the right. Dissociation of O_2 is significantly suppressed with SS excitation.

The choice of carrier frequency is important due to the dependence of ionization rate and T_e on frequency. For example, the combined yields of $O_2(^1\Delta)$ and $O_2(^1\Sigma)$ along the axis, exit yield, and efficiency for a carrier frequency of 27 MHz using cw and SS excitations are shown in Fig. 11 for different powers. As with 13.56 MHz, yields are typically higher for SS compared to cw excitation at low powers. The efficiency obtained with two methods also converges at high powers. At 20 W, the energy deposition required to produce an $O_2(^1\Delta)$ molecule with SS excitation decreases to 4.6 eV at 27 MHz. This enables a 42% improvement in efficiency compared to cw excitation, while at 13.56 MHz, the improvement is 30% for the same conditions.

$O_2(^1\Delta)$ production efficiency increases with increasing carrier frequency with cw excitation as well. For example, $O_2(^1\Delta)$ production efficiency as a function of power with cw excitation for 13.56 and 27 MHz is shown in Fig. 12(a). The efficiency is larger at 27 MHz for powers up to 150 W. At both frequencies, efficiency first increases with power and then saturates. The increase with power results from the decrease in T_e (more dissociation of O_2 and less dissociative attachment) that enables better matching with cross section for excitation of $O_2(^1\Delta)$. This advantage is offset by the dissociation of O_2 and rarefaction that occurs at higher power. Although increasing frequency also increases the efficiency of excitation with SS excitation, the trend with power is opposite to that with cw excitation, as shown in Fig. 12(b). Since T_e is already low [and near optimum for $O_2(^1\Delta)$ production] with SS excitation, the decrease in O_2 density that results from electron-impact dissociation with increasing power serves to lower the fractional power expended in $O_2(^1\Delta)$ excitation.

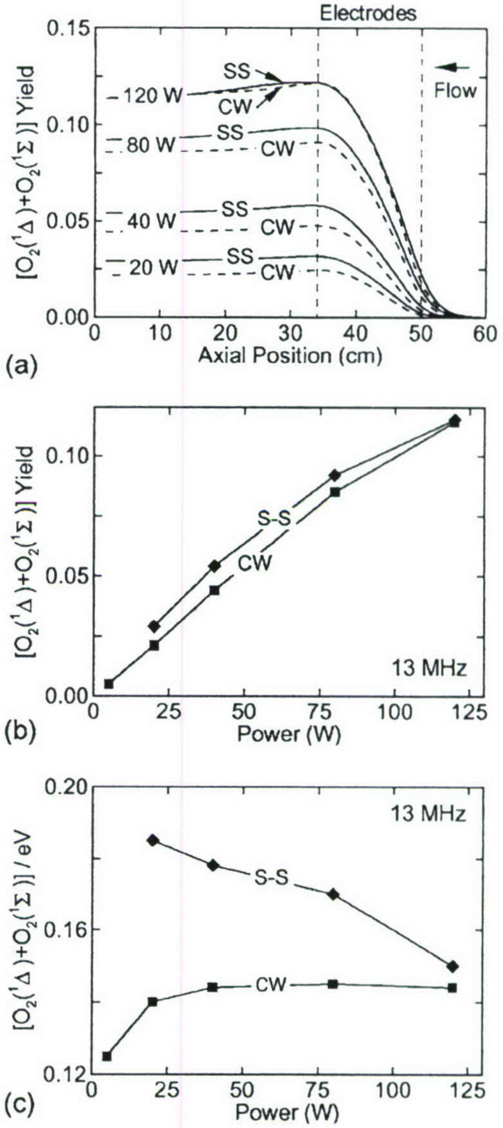

FIG. 10. Plasma parameters as a function of power for cw and SS excitations at 13.56 MHz. (He/O_2=70/30, 3 Torr, 6 lpm). (a) Combined yield of $O_2(^1\Delta)$ and $O_2(^1\Sigma)$ along the axis for flow from the right, (b) combined yields at the outlet of the tube, and (c) efficiency of $O_2(^1\Delta)$ production. Yields are typically higher for SS regime for low power but approach cw excitation at high powers.

The scaling of yield with carrier frequency depends on the method of excitation, as shown in Fig. 13(a). When increasing frequency, T_e generally decreases due to the more efficient electron ionization and reduction in power loss to ion acceleration that occurs at higher frequencies, as shown in Fig. 13(b). With cw excitation, the decrease of T_e with increasing frequency up to 40 MHz brings T_e closer to the optimum range of 1–1.5 eV. As a result, the yield of $O_2(^1\Delta)$ monotonically increases attaining a maximum at about 33 MHz. With SS excitation, T_e is lower than with cw power and near the optimum value at 27 MHz. Increasing fre-

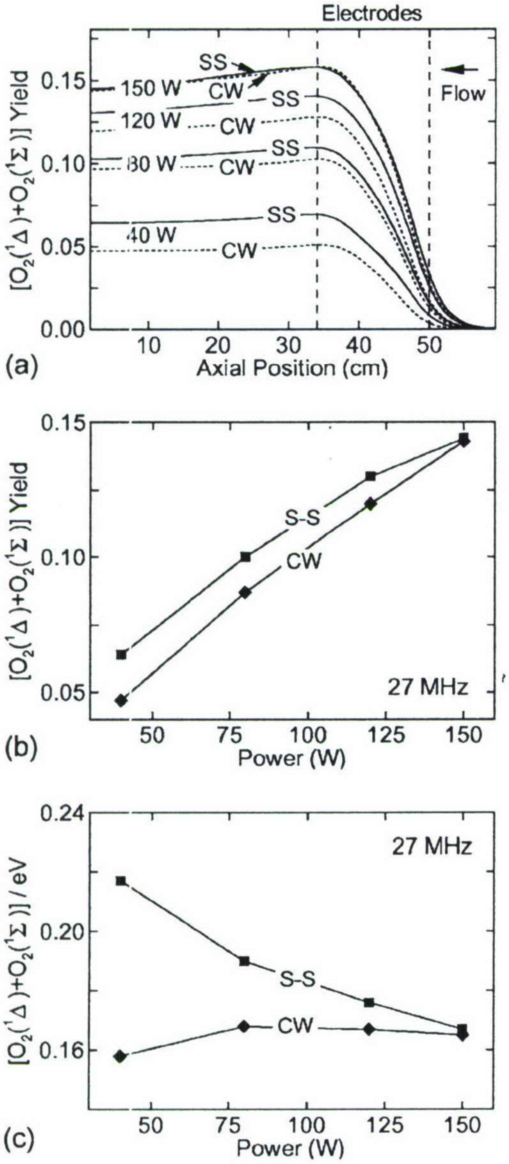

FIG. 11. Plasma parameters as a function of power for cw and SS excitations at 27 MHz. ($He/O_2=70/30$, 3 Torr, 6 lpm). (a) Combined yield of $O_2(^1\Delta)$ and $O_2(^1\Sigma)$ along the axis for flow from the right, (b) combined yields at the outlet of the tube, and (c) efficiency of $O_2(^1\Delta)$ production.

quency from 13.56 to 27 MHz decreases T_e into the optimum range producing an increase in yield. Further increases in frequency decrease T_e to being below optimum for $O_2(^1\Delta)$ production and so yield decreases.

IV. OPTIMIZING SS EXCITATION

Optimizing $O_2(^1\Delta)$ yield using SS excitation depends upon the plasma dynamics that result from the details of the pulse shape, as shown in Fig. 14(a). These characteristics include the carrier frequency, duty cycle (fraction of the SS cycle for the spiker), SS frequency (time between spiker pulses), spiker pulse shape, and value of V_{SS}/V_{cw}. For example, combined yields as function of V_{SS}/V_{cw} are shown in Fig. 14(b). Maximum yields are obtained for $V_{SS}/V_{cw}=2.5-3$. $V_{SS}/V_{cw}=1$ corresponds to cw excitation. As

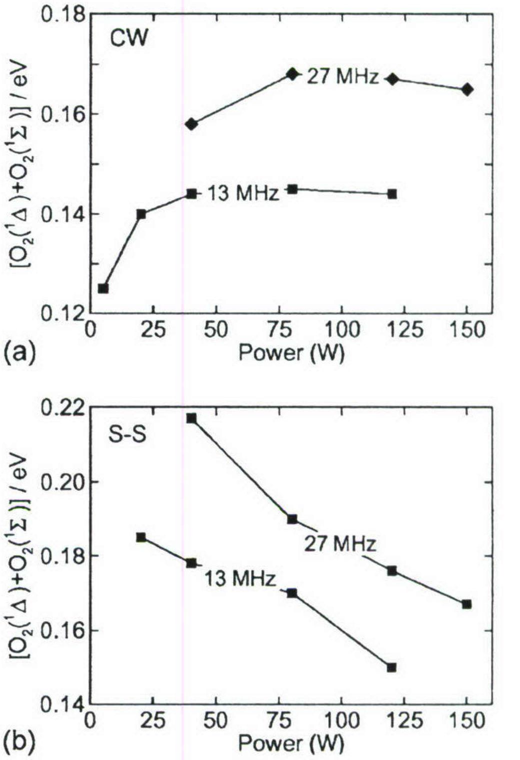

FIG. 12. Comparison of efficiency of $O_2(^1\Delta)$ production for 13.56 and 27 MHz with (a) cw and (b) SS excitations. Using higher carrier frequencies is favorable for both cw and SS excitations.

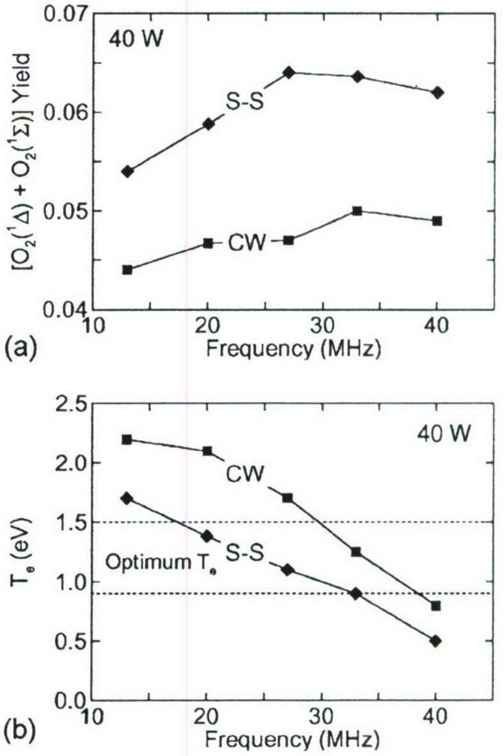

FIG. 13. Plasma parameters as a function of rf for cw and SS excitations. (a) Combined yield at the end of the tube and (b) electron temperature. Electron temperatures generally decrease with increasing carrier frequency and may become too low for optimum $O_2(^1\Delta)$ production.

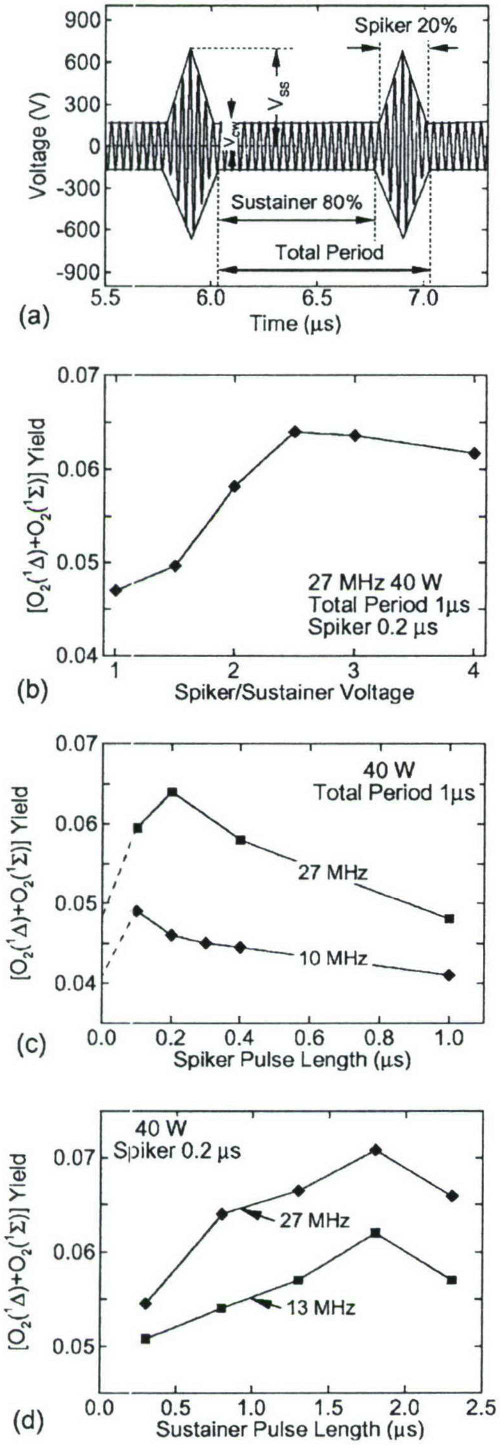

FIG. 14. Optimization of $O_2(^1\Delta)$ production with SS excitation. (a) Voltage wave form for a duty cycle of 20%. Combined yield as a function of (b) the ratio of spiker to sustainer voltage, (c) duty cycle for SS excitation at 10 and 27 MHz carrier frequencies, and (d) sustainer pulse length. Increasing the duty cycle generally decreases yield as the discharge appears to operate in a cw mode.

V_{SS}/V_{cw} increases from one, the amount of excess ionization increases, thereby enabling a lower value of T_e during the sustainer. When keeping the total power constant, as V_{SS}/V_{cw} increases a larger fraction of the power is expended during the avalanche when T_e is large and the efficiency of exciting $O_2(^1\Delta)$ is low. Therefore, very large values of V_{SS}/V_{cw} are not optimum. V_{SS}/V_{cw} should be large enough to produce sufficient excess ionization to last through the sustainer period, but small enough that the majority of the power is dissipated during the sustainer when T_e is low.

Combined yields as a function of spiker pulse length (duty cycle) for 10 and 27 MHz carrier frequencies are shown in Fig. 14(c) for a total SS period of 1 μs. Maximum yields are obtained for duty cycles of 10%–20% depending on carrier frequency. The ideal situation would be a delta-function spiker that produces a large electron temperature, efficiently creating large amounts of excess ionization and depositing little energy. The reality is that a finite time, even for large electron temperatures, is required to produce the excess ionization. For these conditions, that finite time is 100–200 ns. There are practical limitations for the length of the spiker since at least a rf cycle or two are required during the spiker. At 27 MHz and 20% duty cycle, there are five rf periods during the spiker, whereas at 10 MHz and 10% spiker duty cycle, there is only one rf period during the spiker. At the other extreme, as the duty cycle approaches unity SS excitation appears to be cw excitation as quasi-steady-state conditions are obtained during the spiker. Yield therefore decreases and approaches the cw value.

Increasing the sustainer pulse length from small values (<1 μs) increases $O_2(^1\Delta)$ production. For these conditions, $O_2(^1\Delta)$ yield optimizes for a sustainer pulse length of 1.8 μs, as shown in Fig. 14(d). The longer sustainer pulse enables a longer period of operating at low T_e. While keeping the total power constant, extending the sustainer reduces the amount of power dissipated during the spiker and so reduces the amount of excess ionization. With sufficient ionization during the spiker, the optimum sustainer length should approach the 10–15 μs typically required for the plasma to recover to a steady state.

Based on these and other scaling studies we find that $O_2(^1\Delta)$ production optimizes using SS techniques for the following conditions.

- Operate with a high carrier frequency to lower T_e and increase proportion of power dissipated by electrons.
- The spiker pulse length should be as short as possible while still providing sufficient excess ionization to last through the entire sustainer period.
- The spiker voltage should not elevate the electron temperature above that required for rapid ionization.
- The sustainer pulse length should be long enough that the majority of power is dissipated during the sustainer but not so long that the plasma fully recovers to its cw conditions.

V. CONCLUDING REMARKS

The consequences of spiker-sustain excitation on yield of $O_2(^1\Delta)$ in flowing He/O_2 plasmas were investigated with 2D plasma hydrodynamics model. SS techniques generally do lower the time averaged T_e compared to cw excitation and so improve the efficiency of excitation and yield for $O_2(^1\Delta)$. This advantage to SS excitation is diminished at higher powers where T_e is naturally lower for cw excitation. Lower duty cycles (shorter spiker pulses) are generally more advantageous for SS excitation as the limit of a delta-function spiker is approached. Increasing the frequency of excitation is also advantageous due to the lowering of T_e and increase in n_e. Again, the advantage of SS excitation is diminished as frequency increases due to the natural decrease in T_e with cw excitation. The length of the sustainer pulse should be short enough so that T_e is largely below the self-sustaining value but long enough so that T_e and n_e begin recovering towards their steady-state values. This recovery indicates a good utilization of the excess ionization produced by the spiker.

ACKNOWLEDGMENTS

This work was supported by the Air Force Office of Scientific Research and the National Science Foundation (CTS-0520368).

[1] W. E. McDermott, N. R. Pchelkin, D. J. Benard, and R. R. Bousek, Appl. Phys. Lett. **32**, 469 (1978).

[2] H. Fujii, S. Yoshida, M. Iizuka, and T. Atsuta, J. Appl. Phys. **67**, 3948 (1990).

[3] A. Elior, B. D. Barmashenko, E. Lebiush, and S. Rosenwaks, Appl. Phys. B: Lasers Opt. **B61**, 37 (1995).

[4] M. Endo *et al.*, IEEE J. Quantum Electron. **34**, 393 (1998).

[5] D. Furman, E. Bruins, V. Rybalkin, B. D. Barmashenko, and S. Rosenwaks, IEEE J. Quantum Electron. **37**, 174 (2001).

[6] J. Kodymova, O. Spalek, V. Jirasek, M. Censky, and G. D. Hager, Appl. Phys. A: Mater. Sci. Process. **77**, 331 (2003).

[7] J. Kodymova and O. Spalek, Jpn. J. Appl. Phys., Part 1 **37**, 117 (1998).

[8] D. L. Carroll and W. C. Solomon, *ElectriCOIL: An Advanced Chemical Iodine Laser Concept, Proceedings of the XIII International Symposium on Gas Flow and Chemical Lasers and High Power Laser Conference, Florence, Italy, 18–22 September 2000*, edited by A. Lapucci (SPIE, Bellingham, WA, 2000), pp. 40–44.

[9] T. L. Henshaw, T. J. Madden, G. C. M. II, B. T. Anderson, R. F. Tate, M. R. Berman, and G. D. Hager, AIAA Paper No. 2000-2424, 2000.

[10] D. L. Carroll, D. M. King, J. T. Verdeyen, B. Woodard, J. W. Zimmerman, L. Skorski, and W. C. Solomon, AIAA Paper No. 2003-4029, 2003.

[11] J. Schmiedberger, S. Hirahara, Y. Ichinoche, M. Suzuki, W. Masuda, Y. Kihara, E. Yoshitani, and H. Fujii, Proc. SPIE **4184**, 32 (2001).

[12] A. E. Hill, *The Next Generation of Controlled Avalanche Discharge Gas Lasers, International Conference on Lasers, Albuquerque, NM, 2000* (STS, McLean, VA, 2000).

[13] A. A. Ionin, Y. M. Klimachev, A. A. Kotkov, I. V. Kochetov, A. P. Napartovich, L. V. Seleznev, D. V. Sinitsyn, and G. D. Hager, J. Phys. D **36**, 982 (2003).

[14] T. V. Rakhimova *et al.*, AIAA Paper No. 2003-4306, 2003.

[15] Yu. V. Savin *et al.*, J. Phys. D **37**, 3121 (2004).

[16] A. N. Vasiljeva, K. S. Klopovskiy, A. S. Kovalev, D. V. Lopaev, Y. A. Mankelevich, N. A. Popov, A. T. Rakhimov, and T. V. Rakhimova, J. Phys. D **37**, 2455 (2004).

[17] A. Hicks, S. Norberg, P. Shawcross, W. Lempert, J. W. Rich, and I. Adamovich, J. Phys. D **38**, 3812 (2005).

[18] D. L. Carroll, J. T. Verdeyen, D. M. King, B. S. Woodard, L. W. Skorski, J. W. Zimmerman, and W. C. Solomon, IEEE J. Quantum Electron. **39**, 1150 (2003).

[19] D. S. Stafford and M. J. Kushner, J. Appl. Phys. **96**, 2451 (2004).

[20] D. S. Stafford and M. J. Kushner, J. Appl. Phys. **98**, 073303 (2005).

[21] R. Arakoni, D. S. Stafford, N. Yu. Babaeva, and M. J. Kushner, J. Appl. Phys. **98**, 073304 (2005).

[22] D. L. Carroll, J. T. Verdeyen, D. M. King, B. Woodard, L. Skorski, J. W. Zimmerman, and W. C. Solomon, *Recent Work on the Development of an Electric Discharge Oxygen Iodine Laser, XIV International Symposium on Gas Flow and Chemical Lasers and High Power Laser Conference, Wroclaw, Poland, 2002*, edited by K. Abramski, E. Plinski, and W. Wolinski (SPIE, Bellingham, 2002), pp. 316–326.

[23] D. L. Carroll *et al.*, Appl. Phys. Lett. **85**, 1320 (2004).

[24] D. L. Carroll *et al.*, IEEE J. Quantum Electron. **41**, 213 (2005).

[25] D. L. Carroll *et al.*, Appl. Phys. Lett. **86**, 111104 (2005).

[26] D. L. Carroll *et al.*, IEEE J. Quantum Electron. **41**, 1309 (2005).

[27] J. T. Verdeyen, D. M. King, D. L. Carroll, and W. C. Solomon, *Diagnostic Development for the ElectriCOIL Flow System, Proceedings of the Gas and Chemical Lasers and Intense Beam Applications III Conference, San Jose, CA, 22–24 January 2002*, edited by S. Davis and M. Heaven (SPIE, Bellingham, WA, 2002), pp. 154–160.

[28] M. J. Kushner, J. Phys. D **38**, 1633 (2005).

[29] C. C. Leiby and H. J. Oskam, Phys. Fluids **10**, 1993 (1967).

[30] M. J. Yoder, H. H. Legner, J. H. Jacob, and D. R. Ahouse, J. Appl. Phys. **49**, 3171 (1978).

IOP PUBLISHING JOURNAL OF PHYSICS D: APPLIED PHYSICS
J. Phys. D: Appl. Phys. 40 (2007) 4793–4809 doi:10.1088/0022-3727/40/16/009

$O_2(^1\Delta)$ production and gain in plasma pumped oxygen–iodine lasers: consequences of NO and NO_2 additives

Ramesh A Arakoni[1], **Natalia Y Babaeva**[2] **and Mark J Kushner**[2,3]

[1] University of Illinois, Department of Aerospace Engineering, Urbana, IL 61801, USA
[2] Iowa State University, Department of Electrical and Computer Engineering, Ames, IA, 50011, USA

E-mail: arakoni@uiuc.edu, natalie5@iastate.edu and mjk@iastate.edu

Received 27 May 2007, in final form 29 May 2007

Abstract
The 1.315 μm $[I(^2P_{1/2}) \rightarrow I(^2P_{3/2})]$ transition of atomic iodine in the chemical oxygen–iodine laser (COIL) is pumped by sequential reactions of I_2 and I with $O_2(^1\Delta)$. In electrically pumped systems (eCOILs), electron impact excitation of O_2 produces the $O_2(^1\Delta)$ and also produces O atoms through dissociative excitation. The O atoms, through reactions with I_2, $I(^2P_{1/2})$ and $I(^2P_{3/2})$, lead to dissociation of I_2, quenching of the upper laser level and removal of the lower laser level. While dissociating I_2 is potentially beneficial, quenching of the upper laser level is detrimental and so management of the O atom density is necessary to maximize laser gain. In this regard, NO and NO_2 additives have been used to manage the O atom density by cyclically reacting with O and I. In this paper, results from a computational investigation of eCOIL systems using plug flow and two-dimensional models are discussed where NO and NO_2 additives are used. The system is a flowing plasma sustained in He/O_2/NO mixtures with downstream injection of NO_2 followed by injection of I_2. We found that addition of NO and NO_2 is effective in managing the density of O atoms and maximizing gain by minimizing quenching of the upper laser level. We found that by optimizing the additives, laser gain can be maximized even though $O_2(^1\Delta)$ densities may be lower due to the management of quenching and dissociation reactions.

1. Introduction

Chemical oxygen–iodine lasers (COIL) operating on the 1.315 μm $[I(^2P_{1/2}) \rightarrow I(^2P_{3/2})]$ transition of atomic iodine are being investigated due to their high efficiency and potential for multi-kilowatt CW operation [1–3]. A series of collisional transfer reactions between $O_2(^1\Delta)$, I_2 and ground state $I(^2P_{3/2})$ (to be referred to as I) result in excitation of the upper laser level $I(^2P_{1/2})$ (to be referred to as I*). Typically $O_2(^1\Delta)$ is generated upstream of the laser cavity. I_2 is injected immediately prior to the cavity upon which the flow is supersonically expanded to lower the gas temperature as required to maximize the gain. In conventional COILs liquid-phase chemistries (reactions between basic H_2O_2 and Cl_2) produce the $O_2(^1\Delta)$ with high yields [4], although the use of liquid peroxides and Cl_2 gas to produce the $O_2(^1\Delta)$ creates challenges for storage and transport. Recently, efforts have focused on generating the $O_2(^1\Delta)$ in electrical discharges (eCOILs) due to the increased robustness and safety of the all gas-phase system [1–10]. Laser gain and oscillation have been demonstrated in eCOILs by Hicks *et al* [1] and Verdeyen *et al* [3].

A challenge in eCOILs is to produce sufficiently high yields of $O_2(^1\Delta)$, and hence laser gain, to enable the laser transition to be saturated and produce high power [5]. In

---

[3] Author to whom any correspondence should be addressed.

this regard, recent research has focused on tailoring the discharge parameters [6, 7, 10] and using additives such as CO, H_2, D_2 [8] and NO [9] to improve the excitation efficiency of $O_2(^1\Delta)$. NO and NO_2 are also used as additives to control the post-discharge chemistry [9]. In fact, all demonstrations of laser gain and oscillation to date have used flowing plasmas in He/O_2 mixtures with NO as an additive.

eCOILs differ from conventional COILs in that atomic oxygen is also produced in the electric discharge by electron impact dissociation of O_2. The O atoms flow downstream where 3-body reactions produce O_3 and the remaining O atoms may react with the injected I_2. Beneficial reactions of O with I_2 produce I atoms, thereby eliminating the expense of $O_2(^1\Delta)$ molecules for initiating the dissociating reactions. Detrimental reactions involving O atoms include quenching of I^* by O which reduces gain. As such, management of the O atom density is important to optimize these opposing effects.

Injection of NO or NO_2 through or downstream of the discharge in eCOIL systems has two goals; improving the efficiency of direct production of $O_2(^1\Delta)$ in the discharge by electron impact and management of the O atom density downstream of the plasma. Including NO in the gas stream flowing through the discharge has, in part, the goal of improving production of $O_2(^1\Delta)$. NO, having a lower ionization potential (9.26 eV) than either O_2 or He, is likely to provide more rapid ionization with the possibility of lowering the operating E/N (electric field/gas number density) and electron temperature, T_e. Lowering T_e from the values typical of self-sustained He/O_2 mixtures is advantageous in more efficiently producing $O_2(^1\Delta)$ by direct electron impact [6, 8, 11]. Discharges in NO have also been known to produce $O_2(^1\Delta)$ in relatively large amounts even though O_2 may not be present as a feedstock gas [12]. However, when flowing NO through the discharge, some of the power that would otherwise be available to excite O_2 is dissipated by excitation and ionization of NO, an unwanted consequence.

In addition to possibly improving the production of $O_2(^1\Delta)$, NO and NO_2 are potentially effective in managing the inventory of O atoms through direct and cyclic reactions which have the effect of converting O atoms back into O_2. In the context of eCOIL systems where I_2 is injected, O atoms are beneficial by dissociating I_2 (and product species IO) to form I atoms which are then pumped to I^* by collisions with $O_2(^1\Delta)$. The O atoms are detrimental by quenching I^*. Totally eliminating O atoms is therefore not necessarily beneficial. NO and NO_2 also have secondary effects in that they react with I atoms forming intermediary species such as INO, and INO_2 which further react with I to reform I_2 [13].

In this paper, we report on results from a computational investigation of the consequences of NO and NO_2 additives on flowing He/O_2 plasmas and their afterglows with I_2 injection in the context of eCOIL systems. These investigations were conducted using plug flow and 2-dimensional (2D) plasma-hydrodynamics models. Although for most conditions the addition of NO to the inlet gas stream reduced the density of $O_2(^1\Delta)$, it ultimately increased the densities of I^* downstream of the discharge through management of the O atom density. The inlet NO mole fraction also typically increased the extent of the region over which positive laser gain could be achieved. This can be particularly useful in high speed flows where mixing lengths are longer. Injection of NO_2 in the post-discharge flow can help in rapidly scavenging O atoms in two body reactions (as compared with scavenging by NO which proceeds by a 3-body mechanism). In general, addition of NO_2 in the post-discharge region improves laser gain [9]. The downside to NO_2 injection is a rise in gas temperature due to the exothermicity of the reactions between NO_2 and O.

The models used in this investigation are described in section 2 followed by a discussion of the reaction mechanism in sections 3. In section 4 the consequences of NO flowing through the discharge and its influence on downstream kinetics when I_2 is injected are described. In section 5, the post-discharge kinetics with NO_2 addition upstream of I_2 injection are discussed. Our concluding remarks are in section 6.

2. Description of models

This investigation was conducted using a plug flow model, *GlobalKIN*, and a 2D plasma hydrodynamics model, *nonPDPSIM*. *GlobalKIN* has been previously described in [11, 14] and so will only be briefly discussed here. *GlobalKIN* consists of a volume averaged plasma chemistry module and an electron energy transport module. The plasma chemistry module provides the time rate of change of species densities based on gas-phase chemistry and surface reactions. Electron temperature, T_e, and average gas temperature, T_g, are also solved for by integrating their respective conservation equations. The electron energy transport module consists of a solution of Boltzmann's equation for the electron energy distribution (EED) which provides electron impact rate coefficients based on the EEDs and fundamental cross-sections.

For plasmas flowing through cylinders having large aspect ratios, transport to the radial surfaces is taken into account by using a diffusion length. By simultaneously calculating the axial speed of the flow based on constant pressure, change in enthalpy, species densities, conservation of mass and gas temperature, the integration in time is mapped to axial position. The resulting rate equations are integrated in time using a stiff ordinary differential equation solver. To address the use of additives, *GlobalKIN* was modified to enable the downstream injection of gases into the flow. Injection nozzles were treated as point sources of mass, axial momentum and enthalpy. Power deposition as a function of axial position must be specified in *GlobalKIN*. This distribution was estimated by averaging the power deposition obtained from the *nonPDPSIM* over the cross-section of the tube.

nonPDPSIM has been discussed in detail in [15, 16], and so will only be briefly described here along with pertinent updates to the model. Continuity equations for charged gas-phase species, surface charges and Poisson's equation for the electric potential are simultaneously implicitly integrated in time. Updates of these quantities are followed, in a time splicing manner, with updates of T_e and neutral species densities using a modified form of the compressible Navier–Stokes equations for continuity, momentum and energy (gas temperature) which accounts for interactions with the plasma. A circuit model was used to interface the plasma with metal surfaces connected to a voltage source and circuit elements (e.g. ballast resistor). The power supply voltage was adjusted to deposit the specified power in the plasma.

To address the longer time scales for the injection and mixing of additives downstream the following method was used. It was determined and validated that the injected gases were sufficiently far downstream from the plasma that their presence did not affect the plasma properties. As such, plasma quantities (for example, electron density (n_e), T_e, rates of electron impact reactions, and ionization sources) were calculated until a quasi-steady state was reached after which these quantities were 'frozen' in the upstream plasma zone. Following the establishment of the plasma properties only the neutral fluid equations were integrated (accounting for injection of gases downstream) which did not affect quantities upstream in the plasma. This enabled a longer time-step downstream where the injection kinetics occurred.

3. Reaction mechanism

The species included in the reaction mechanism are e, He, He(^{2}S), He$^+$, O_2, O_2(v), $O_2(^1\Delta)$, $O_2(^1\Sigma)$, O_2^-, O_2^+, O, O(^{1}D), O(^{1}S), O^-, O^+, O_3, O_3^-, NO, NO$^+$, NO_2, NO$^-$, NO_2^-, N, N_2, I_2, I_2^*, I($^2P_{3/2}$), I($^2P_{1/2}$), IO, INO and INO_2. He(^{2}P) was included for purposes of electron energy loss in solving Boltzmann's equation but was lumped with He(^{2}S) in the chemical kinetics. O_2(v) represents the sum of the first four vibrational levels of O_2. The vibrational levels of N_2 were not included as individual species in the reaction mechanism as N_2 densities were small and predominantly produced downstream of the discharge where electron impact processes are negligible. Excitation of the first five vibrational levels of NO ($\Delta\varepsilon$ = 0.23, 0.46, 0.69, 0.91 and 1.13) and the electronic states NO($a^2\Sigma$) ($\Delta\varepsilon$ = 5.48 eV), NO($c^2\Pi$) ($\Delta\varepsilon$ = 6.5 eV) and NO($b^4\Sigma$) ($\Delta\varepsilon$ = 7.58 eV) were included for purposes of energy loss collisions with ground state NO. The densities of these states were not explicitly tracked in the model. The negative ions NO$^-$ and NO_2^- were included only in *GlobalKIN* after confirming that their exclusion does not make a significant change to the reaction kinetics in *nonPDPSIM*. Their exclusion from *nonPDPSIM* was for the purpose of speeding the calculation.

The reaction mechanism builds upon that previously developed for He/O_2 discharges and which is discussed in [14]. The processes that were added to that reaction mechanism to account for the injection of NO, NO_2 and I_2 are listed in table 1.

The majority of $O_2(^1\Delta)$ is produced by electron impact excitation of ground state O_2 in the plasma zone, and secondarily by excitation of $O_2(^1\Sigma)$ followed by quenching to $O_2(^1\Delta)$ by collisions with O atoms,

$$e + O_2 \rightarrow O_2(^1\Delta) + e, \qquad (1)$$

$$e + O_2 \rightarrow O_2(^1\Sigma) + e, \qquad (2)$$

$$O + O_2(^1\Sigma) \rightarrow O_2(^1\Delta) + O, \qquad (3)$$

$$e + O_2 \rightarrow O + O + e, \qquad (4)$$

$$e + O_2 \rightarrow O(^1D) + O + e. \qquad (5)$$

Electron impact dissociation of O_2 (equations (4) and (5)) is a significant source of O atoms and, in part, the motivation for injection of NO and NO_2 to manage the resulting flow of O atoms. For self-sustaining discharges, roughly one O atom is generated for every $O_2(^1\Delta)$ produced in the plasma zone. By lowering T_e to 1–1.5 eV from self-sustaining values of 2–3 eV by, for example, using the spiker–sustainer methods, the rate of excitation of $O_2(^1\Delta)$ can be increased relative to electron impact dissociation [11].

The negative ion chemistry of He/O_2 mixtures is initiated by dissociative attachment and 3-body reactions,

$$e + O_2 \rightarrow O^- + O, \qquad (6)$$

$$e + O_2 + M \rightarrow O_2^- + M, \; (k = 3.6 \times 10^{-31} T_e^{-0.5}\,\mathrm{cm^6\,s^{-1}}), \qquad (7)$$

where M is a third body and k is the rate coefficient. O_2^- subsequently charge exchanges with O atoms to form O^- or associatively detaches to form O_3. A similar process occurs with O^- to reform O_2,

$$O_2^- + O \rightarrow O_2 + O^-, \quad (k = 1.5 \times 10^{-10}\,\mathrm{cm^3\,s^{-1}}), \qquad (8)$$

$$O_2^- + O \rightarrow O_3 + e, \quad (k = 1.5 \times 10^{-10}\,\mathrm{cm^3\,s^{-1}}), \qquad (9)$$

$$O^- + O \rightarrow O_2 + e, \quad (k = 2 \times 10^{-10}\,\mathrm{cm^3\,s^{-1}}). \qquad (10)$$

Through dissociative detachment reactions, both O^- and O_2^- react with $O_2(^1\Delta)$ to form O_3, and to quench $O_2(^1\Delta)$,

$$O^- + O_2(^1\Delta) \rightarrow O_3 + e, \quad (k = 3 \times 10^{-10}\,\mathrm{cm^3\,s^{-1}}), \qquad (11)$$

$$O_2^- + O_2(^1\Delta) \rightarrow O_2 + O_2 + e, \quad (k = 2 \times 10^{-10}\,\mathrm{cm^3\,s^{-1}}). \qquad (12)$$

An important motivation for flowing NO through the plasma zone is that it has a smaller ionization potential than O_2 and He and so should produce more ionization at a lower T_e,

$$e + NO \rightarrow NO^+ + e + e, \quad (\Delta\varepsilon = 9.26\,\mathrm{eV}). \qquad (13)$$

This ionization does, however, come at the cost of channelling discharge power into NO (e.g. vibrational excitation and dissociation), power that might otherwise be deposited into O_2. This power therefore does not directly lead to generation of $O_2(^1\Delta)$. Since NO$^+$ has the smallest ionization potential among all the atoms and molecules in this mechanism, significant amounts of NO$^+$ are formed by charge-exchange reactions with He$^+$, O^+ and O_2^+. Dissociative recombination of NO$^+$ with electrons can produce N, O and O(^{1}D), as well as contribute to gas heating through Frank–Condon processes,

$$e + NO^+ \rightarrow N + O, \qquad (k = 3.4 \times 10^{-7} T_e^{-0.5}\,\mathrm{cm^3\,s^{-1}}, \; \Delta H = -2.77\,\mathrm{eV}), \qquad (14)$$

$$\rightarrow N + O(^1D) \qquad (k = 6.0 \times 10^{-8} T_e^{-0.5}\,\mathrm{cm^3\,s^{-1}}, \; \Delta H = -0.8\,\mathrm{eV}), \qquad (15)$$

where ΔH is the change in enthalpy of the recombination event.

NO also intercepts the negative ion chemistry through charge-exchange reactions and associative attachment,

$$O^- + NO \rightarrow NO_2 + e, \quad (k = 2.8 \times 10^{-10}\,\mathrm{cm^3\,s^{-1}}), \qquad (16)$$

$$O^- + NO_2 \rightarrow NO_2^- + O, \quad (k = 1.2 \times 10^{-9}\,\mathrm{cm^3\,s^{-1}}). \qquad (17)$$

These reactions are potentially beneficial in two ways. They increase the electron density which can lower T_e into a more favourable range for exciting $O_2(^1\Delta)$ and they reduce the density of O^- which would otherwise quench $O_2(^1\Delta)$ to form

Table 1. Processes added to He/O_2 reaction mechanism with NO, NO_2 and I_2.

Species		
He	NO	e
He^*	NO_2	He^+
O	N	O_2^+
$O(^1D)$	N_2	O_2^-
$O(^1S)$	I_2	O^+
O_2	I	O^-
$O_2(v)$	I^*	O_3^-
$O_2(^1\Delta)$	IO	NO^+
$O_2(^1\Sigma)$	INO	NO^-
O_3	INO_2	NO_2^-

Reaction	Rate coefficient[a]	Reference
$e + NO \rightarrow N + O^-$	[b]	[18]
$e + NO \rightarrow N + O + e$	[b]	[19]
$e + NO \rightarrow NO^+ + e + e$	[b]	[20]
$e + NO \rightarrow N + O^+ + e + e$	[b]	[20]
$e + NO^+ \rightarrow N + O$	$3.4 \times 10^{-7}\ T_e^{-0.5}$	[21]
$e + NO^+ \rightarrow N + O(^1D)$	$6.0 \times 10^{-7}\ T_e^{-0.5}$	[21]
$e + NO + He \rightarrow NO^- + He$	$1.0 \times 10^{-32}\ T_e^{-0.5}$	[22]
$e + NO + NO \rightarrow NO^- + NO$	$6.5 \times 10^{-31}\ T_e^{-0.5}$	[22]
$He^* + NO \rightarrow He + NO^+ + e$	2.5×10^{-10}	[c]
$He^+ + NO \rightarrow He + NO^+$	1.6×10^{-9}	[23]
$He^+ + NO \rightarrow He + N + O^+$	4.2×10^{-10}	[23]
$O^+ + NO \rightarrow O + NO^+$	1.7×10^{-12}	[23]
$O_2^+ + NO \rightarrow O_2 + NO^+$	4.5×10^{-10}	[23]
$O_2^+ + N \rightarrow NO^+ + O$	1.2×10^{-10}	[23]
$NO^-, NO_2^- + M^+ \rightarrow NO, NO_2 + M$[d]	$2.0 \times 10^{-7}\ (T_g/300)^{-1}$	[c]
$NO^+ + M^- \rightarrow NO + M$[e]	$2.0 \times 10^{-7}\ (T_g/300)^{-1}$	[c]
$O^- + NO \rightarrow NO_2 + e$	$2.8 \times 10^{10}\ (T_g/300)^{0.5}$	[23]
$O^- + N \rightarrow NO + e$	$2.2 \times 10^{-10}\ (T_g/300)^{0.5}$	[23]
$O^- + NO_2 \rightarrow NO_2^- + e$	$1.2 \times 10^{-9}\ (T_g/300)^{0.5}$	[23]
$O_2^- + N \rightarrow NO_2 + e$	$4.0 \times 10^{-10}\ (T_g/300)^{0.5}$	[23]
$O_2^- + NO_2 \rightarrow NO_2^- + O_2$	$7.0 \times 10^{-10}\ (T_g/300)^{0.5}$	[23]
$O_3^- + NO \rightarrow NO_2^- + O_2$	$2.2 \times 10^{-12}\ (T_g/300)^{0.5}$	[23]
$NO^- + NO \rightarrow NO + NO + e$	$5.0 \times 10^{-12}\ (T_g/300)^{0.5}$	[23]
$NO^- + He \rightarrow NO + He + e$	$2.4 \times 10^{-13}\ (T_g/300)^{0.5}$	[23]
$NO^- + NO_2 \rightarrow NO + NO_2^-$	$7.4 \times 10^{-10}\ (T_g/300)^{0.5}$	[23]
$NO^- + O_2 \rightarrow NO + O_2^-$	$5.0 \times 10^{-10}\ (T_g/300)^{0.5}$	[23]
$NO_2^- + O_3 \rightarrow O_3^- + NO_2$	$9.4 \times 10^{-12}\ (T_g/300)^{0.5}$	[23]
$NO + O_3 \rightarrow NO_2 + O_2$	$1.4 \times 10^{-12}\ e^{-1310/T_g}$	[24]
$NO + O_2(^1\Delta) \rightarrow NO + O_2$	3.5×10^{-17}	[25]
$NO + O(^1D) \rightarrow N + O_2$	5.0×10^{-15}	[26]
$NO + O(^1D) \rightarrow NO + O$	4.0×10^{-11}	[27]
$NO + O + M \rightarrow NO_2 + M$[f]	$1.0 \times 10^{-31}\ (T_g/300)^{-1.6}$	[24]
$NO_2 + O \rightarrow NO + O_2$	$4.2 \times 10^{-12}\ e^{273/T_g}$	[24]
$NO_2 + O(^1D) \rightarrow NO_2 + O$	3.2×10^{-10}	[28]
$NO_2 + O(^1D) \rightarrow NO + O_2$	3.0×10^{-10}	[28]
$N + O_2 \rightarrow NO + O$	$2.4 \times 10^{-11}\ e^{-5320/T_g}$	[29]
$N + NO_2 \rightarrow NO + NO$	6.1×10^{-12}	[30]
$N + NO_2 \rightarrow N_2 + O + O$	2.4×10^{-12}	[30]
$N + NO_2 \rightarrow N_2 + O_2$	1.8×10^{-12}	[30]
$N + O + M \rightarrow NO + M$[f]	$5.5 \times 10^{-33}\ e^{155/T_g}$	[31]
$O_2(^1\Delta) + O_2 + O \rightarrow O_2 + O_2 + O$	1.0×10^{-32}	[10]
$O_2(^1\Sigma) + I_2 \rightarrow O_2 + I + I$	2.8×10^{-11}	[9]
$O_2(^1\Sigma) + I_2 \rightarrow O_2(^1\Delta) + I_2$	2.3×10^{-11}	[9]
$O_2(^1\Sigma) + I_2 \rightarrow O_2 + I_2$	6.0×10^{-12}	[9]
$O_2(^1\Delta) + I_2 \rightarrow O_2 + I_2^*$	7.0×10^{-15}	[9]
$O_2(^1\Delta) + I_2 \rightarrow O_2 + I_2$	5.0×10^{-16}	[9]
$O + I_2 \rightarrow IO + I$	1.4×10^{-10}	[9]
$He + I_2^* \rightarrow He + I_2$	9.8×10^{-12}	[9]
$O_2 + I_2^* \rightarrow O_2 + I_2$	4.9×10^{-12}	[9]
$O_2(^1\Delta) + I_2^* \rightarrow O_2 + I + I$	3.0×10^{-10}	[9]
$O_2(^1\Delta) + I \rightarrow O_2 + I^*$	$7.7 \times 10^{-11}\ (T_g/300)^{-1.0}$	[9]
$O_2(^1\Delta) + I \rightarrow O_2 + I$	1.0×10^{-15}	[9]
$O_3 + I \rightarrow O_2 + IO$	$2.0 \times 10^{-11}\ e^{-890/T_g}$	[9]
$He + I^* \rightarrow He + I$	5.0×10^{-18}	[9]
$O_2(^1\Delta) + I^* \rightarrow O_2(^1\Sigma) + I$	$8.4 \times 10^{-15}\ (T_g/300)^{3.8}\ e^{700/T_g}$	[9]

Table 1. Continued.

Reaction	Rate coefficient[a]	Reference
$O_2(^1\Delta) + I^* \rightarrow O_2 + I$	1.10×10^{-13}	[9]
$O_2 + I^* \rightarrow O_2^* + I$	$1.0 \times 10^{-10}\ (T_g/300)^{-1.0}\ e^{-403/T_g}$	[9]
$O + I^* \rightarrow O + I$	8.0×10^{-12}	[9]
$NO + I^* \rightarrow NO + I$	1.2×10^{-13}	[9]
$NO_2 + I^* \rightarrow NO_2 + I$	8.5×10^{-14}	[9]
$I_2 + I^* \rightarrow I_2^* + I$	$1.40 \times 10^{-13}\ e^{1600/T_g}$	[9]
$IO + IO \rightarrow O_2 + I + I$	8.2×10^{-11}	[9]
$NO + IO \rightarrow NO_2 + I$	$4.3 \times 10^{-12}\ e^{-397/T_g}$	[32]
$O + IO \rightarrow O_2 + I$	1.4×10^{-10}	[9]
$O + IO \rightarrow O_2(^1\Delta) + I$	1.5×10^{-11}	[9]
$I + INO \rightarrow I_2 + NO$	1.6×10^{-10}	[13]
$I + INO_2 \rightarrow I_2 + NO_2$	8.3×10^{-11}	[13]
$INO + INO \rightarrow I_2 + NO + NO$	$8.4 \times 10^{-11}\ e^{-2620/T_g}$	[13]
$INO_2 + INO_2 \rightarrow I_2 + NO_2 + NO_2$	$2.9 \times 10^{-11}\ e^{-2600/T_g}$	[13]
$I + I + I_2 \rightarrow I_2 + I_2$	3.6×10^{-30}	[9]
$I + I + He \rightarrow I_2 + He$	3.8×10^{-33}	[9]
$I + I + O_2 \rightarrow I_2 + O_2$	3.3×10^{-32}	[9]
$I + I^* + I_2 \rightarrow I + I + I_2$	3.6×10^{-30}	[9]
$I + I + O_2 \rightarrow I_2 + O_2(^1\Delta)$	3.7×10^{-33}	[9]
$I + NO + He \rightarrow INO + He$	$6.0 \times 10^{-33}\ (T_g/300)^{-1.0}$	[13]
$I + NO + O_2 \rightarrow INO + O_2$	1.6×10^{-32}	[13]
$I + NO_2 + He \rightarrow INO_2 + He$	$1.5 \times 10^{-31}\ (T_g/300)^{-1.0}$	[13]
$I + NO_2 + O_2 \rightarrow INO_2 + O_2$	2.6×10^{-31}	[13]
$I^* \rightarrow I$	10	[33]

[a] Rate coefficient in $cm^3\ s^{-1}$ for 2-body reactions, and $cm^6\ s^{-1}$ for 3-body reactions and s^{-1} for radiation reactions.

[b] Rate coefficients calculated using cross-section data from the indicated reference.

[c] Estimated.

[d] Where M is one of the cations O^+, O_2^+, He^+ or NO^+.

[e] Where M is one of the anions O^-, O_2^- or O_3^-.

[f] Where M is one of the major neutral species He, O_2, $O_2(v)$, $O_2(^1\Delta)$, O or O_3.

O_3. The negative ions NO^- and NO_2^- were not included in the 2D model (to increase computational speed), whereas they were included in the plug flow model. Computational experiments were conducted using the plug flow model to quantify the effects of the NO^- and NO_2^- and are discussed below.

One of the primary motivations of injecting NO and NO_2 is in their potential for managing of the O atom inventory. Much of this chemistry is cyclic. NO reacts with O to form NO_2 which then further reacts with O to regenerate O_2,

$$NO + O + M \rightarrow NO_2 + M, \quad (k = 1.0 \times 10^{-31}(T_g/300)^{-1.6}, \quad \Delta H = -3.18\,\text{eV}), \tag{18}$$

$$NO_2 + O \rightarrow NO + O_2, \quad (k = 4.2 \times 10^{-12}\exp(273/T_g), \quad \Delta H = -2.0\,\text{eV}). \tag{19}$$

This is an important reaction chain that can reduce the inventory of O atoms and so eliminate a quencher of the upper laser level, I^*. At low pressures where the 3-body density is low, the rate of reaction of O with NO_2 occurs at a higher rate than with NO. Hence addition of NO_2 in the downstream region may be preferred over that of NO if the residence time in the flow tube is a limiting factor. These reactions are, however, exothermic and so can increase the gas temperature which is generally not beneficial.

Laser gain is ultimately achieved by injection of I_2 downstream of the plasma zone, and by its reacting with O, $O_2(^1\Delta)$, and $O_2(^1\Sigma)$ to create I atoms and to pump the upper laser level. In a conventional COIL there is a negligible inventory of O atoms and $O_2(^1\Sigma)$, and so the dissociation of I_2 is dominantly by $O_2(^1\Delta)$ in a two-step process,

$$O_2(^1\Delta) + I_2 \rightarrow O_2 + I_2^*, \quad (k = 7 \times 10^{-15}\,\text{cm}^3\,\text{s}^{-1}), \tag{20}$$

$$O_2(^1\Delta) + I_2^* \rightarrow O_2 + I + I, \quad (k = 3 \times 10^{-10}\,\text{cm}^3\,\text{s}^{-1}). \tag{21}$$

In eCOIL, the presence of $O_2(^1\Sigma)$ and O helps in dissociating I_2 and producing I atoms. A reaction intermediate IO is also helpful in this regard,

$$O_2(^1\Sigma) + I_2 \rightarrow O_2 + I + I, \quad (k = 2.8 \times 10^{-11}\,\text{cm}^3\,\text{s}^{-1}), \tag{22}$$

$$O + I_2 \rightarrow IO + I, \quad (k = 1.4 \times 10^{-10}\,\text{cm}^3\,\text{s}^{-1}), \tag{23}$$

$$O + IO \rightarrow I + O_2, \quad (k = 1.4 \times 10^{-10}\,\text{cm}^3\,\text{s}^{-1}). \tag{24}$$

The laser pumping reaction by $O_2(^1\Delta)$ in collisions with I is favoured at lower temperatures over its endothermic back reaction,

$$O_2(^1\Delta) + I \rightarrow O_2 + I^*, \quad (k = 7.7 \times 10^{-11}(T_g/300)^{-1}\,\text{cm}^3\,\text{s}^{-1}), \tag{25}$$

$$O_2 + I^* \rightarrow O_2(^1\Delta) + I, \quad (k = 1.0 \times 10^{-10}(T_g/300)^{-1}e^{-403/T_g}). \tag{26}$$

To suppress the back reaction, the laser cavity is typically placed in a supersonically expanded flow to lower the translational temperature. As such, the threshold yield, Y_{th}, of $O_2(^1\Delta)$ required for positive optical gain in an undissociated flow of O_2 is [17],

$$Y_{th} = \frac{[O_2(^1\Delta)]}{[O_2]} = \frac{1}{1 + 1.5\exp(401/T_g)}. \tag{27}$$

For example, in an undissociated flow of O_2, the threshold yield at room temperature is 15% whereas at 180 K the threshold yield is 6%.

Quenching of I^* occurs dominantly by reactions with O and O_2 (the backward reaction), and to a lesser extent with $O_2(^1\Delta)$ and NO,

$$O + I^* \rightarrow O + I, \qquad (k = 8.0 \times 10^{-12}\,\mathrm{cm^3\,s^{-1}}), \tag{28}$$

$$NO + I^* \rightarrow NO + I, \qquad (k = 1.2 \times 10^{-13}\,\mathrm{cm^3\,s^{-1}}). \tag{29}$$

NO and NO_2 also help in removing ground state I atoms and so aid in maintaining the inversion,

$$I + NO + O_2 \rightarrow INO + O_2, \quad (k = 1.6 \times 10^{-32}\,\mathrm{cm^6\,s^{-1}}), \tag{30}$$

$$I + NO + He \rightarrow INO + He, \quad (k = 6.0 \times 10^{-33}\,\mathrm{cm^6\,s^{-1}}), \tag{31}$$

$$I + NO_2 + O_2 \rightarrow INO_2 + O_2, \quad (k = 2.6 \times 10^{-31}\,\mathrm{cm^6\,s^{-1}}), \tag{32}$$

$$I + NO_2 + He \rightarrow INO_2 + He, \quad (k = 6.0 \times 10^{-33}\,\mathrm{cm^6\,s^{-1}}). \tag{33}$$

The INO_x species in turn abstract I atoms to release I_2 and NO_x back into the flow,

$$INO + I \rightarrow I_2 + NO, \quad (k = 1.6 \times 10^{-10}\,\mathrm{cm^3\,s^{-1}}), \tag{34}$$

$$INO_2 + I \rightarrow I_2 + NO_2, \quad (k = 8.3 \times 10^{-11}\,\mathrm{cm^3\,s^{-1}}). \tag{35}$$

Typically, the injection of I_2 occurs during or following a supersonic expansion of the gas to velocities equivalent to Mach 2 or Mach 3 to lower T_g to decrease the yields of $O_2(^1\Delta)$ required to achieve positive gain. Accurately simulating a supersonic expansion is difficult in our modelling platform. In order to provide a best case estimate for laser gain we used for the temperature of the reactions in equations (25) and (26) a value appropriate for a Mach 2 flow. This temperature can be approximated from

$$\frac{T_0}{T_g} = \left(1 + \frac{\gamma - 1}{2} M^2\right), \tag{36}$$

where T_0 is the stagnation (or tank) temperature, γ is the ratio of specific heats and M is the Mach number. For $M = 2$ and $T_0 = 300$ K, this ratio is ≈2.18, and would lead to a gas temperature of 137 K. The reaction mechanism was validated by comparing with experimental data from Carroll *et al* [34], as discussed below.

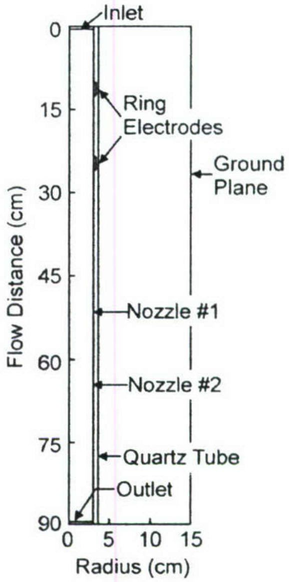

Figure 1. Geometry of the cylindrically symmetric reactor. The flow enters from the top and is pumped from the bottom. Discharge power at 25 MHz is capacitively coupled through ring electrodes. Two nozzles downstream of the discharge inject mixtures of He, NO, NO_2 and/or I_2.

4. Consequences of NO in the inlet flow

A schematic of the cylindrically symmetric, 6 cm diameter flow tube used in this study is shown in figure 1. In the base case, a power of 40 W was capacitively coupled using ring electrodes operated at 25 MHz. A mixture of He/O_2/NO at 3 Torr entered through the inlet at a flow rate of 6 slpm which corresponds to an axial speed of $\approx 890\,\mathrm{cm\,s^{-1}}$. The flow consisted of 30% O_2 with the balance divided between He and NO. The NO mole fraction was varied from 0–10%. Two injection nozzles are located downstream. (In the 2D cylindrically symmetric geometry these nozzles appear to be rings.) The first nozzle at 51.5 cm was used to inject a mixture of He/NO/NO_2. The second nozzle at 64.5 cm injected a mixture of He/I_2. At the outlet, axial gradients were assumed to be zero and the exit speeds were adjusted to maintain constant pressure and mass flux.

Plasma characteristics (n_e, T_e, negative total negative ion density M^-, total positive ion density M^+ and power density) obtained with *nonPDPSIM* are shown in the vicinity of the electrodes in figure 2 for the base case having an inlet flow of He/O_2/NO = 67/30/3. T_e in the bulk of the discharge was 2.3 eV and the peak electron density was $9.0 \times 10^9\,\mathrm{cm^{-3}}$. Since NO and O_2 are attaching species, the negative ion density (maximum of $1.1 \times 10^{10}\,\mathrm{cm^{-3}}$) is commensurate with n_e. The electron density is fairly symmetric between the electrodes and relatively uniform. The power deposition is moderately higher near the upstream electrode due to gas heating which reduces the neutral densities downstream. This is not a general result as higher power deposition and more rarefaction can produce regions of locally intense power deposition near the downstream electrode.

The densities of the neutral species O, $O_2(^1\Delta)$, I and I^* and T_g for the base case are shown in figure 3. A flow of 36 sccm of pure NO was injected through the first nozzle and a flow of 100 sccm of He/I_2 = 99/1 was injected through the second nozzle. Having few quenchers at these pressures, the $O_2(^1\Delta)$ accumulates as the gas flows through the discharge reaching a maximum value of $1.35 \times 10^{15}\,\mathrm{cm^{-3}}$. The $O_2(^1\Delta)$ density remains nearly constant thereafter until the injection point for I_2. Reactions of $O_2(^1\Delta)$ with I_2 and I (the latter being the laser pumping reaction producing I^*) reduce its density by a factor of five to $2.7 \times 10^{14}\,\mathrm{cm^{-3}}$.

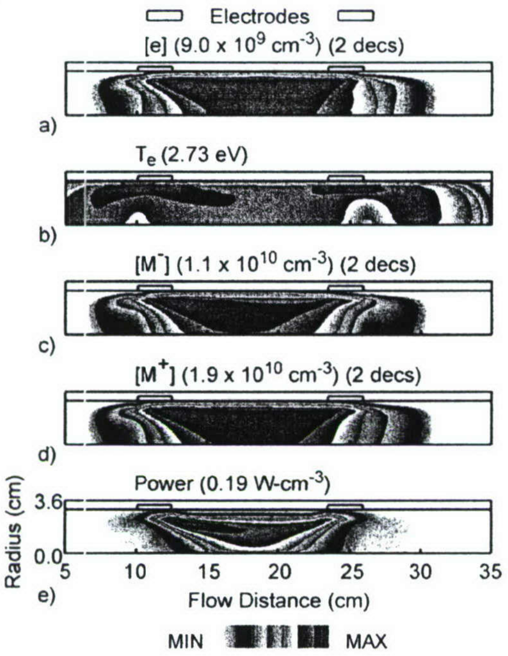

Figure 2. Base case plasma characteristics from the 2D model for 3 Torr, 40 W, $He/O_2/NO = 67/30/3$ and a flow rate of 6 slpm. (*a*) Electron density, (*b*) electron temperature, (*c*) sum of negative ion densities, (*d*) sum of positive ion densities and (*e*) power density. The scales are linear for T_e and power (0 to maximum), and the densities are plotted on a 2-decade log scale.

Similar to $O_2(^1\Delta)$, the density of O atoms accumulate from electron impact dissociation of O_2 passing through the discharge (with a small amount of depletion of the O in forming O_3) until the injection point of NO at the first nozzle. The O densities decrease from a peak value of 1.4×10^{15} to 4.0×10^{14} cm^{-3} downstream of the NO injection due to its reaction with NO. The remaining O atoms flow to the injection point of I_2 where they are further depleted in dissociating reactions with I_2. The I_2 is nearly completely dissociated by reactions with the O atoms to form I. Pumping reactions between $O_2(^1\Delta)$ and I produce I*. The region of positive gain (where the inversion density $G = [I^*] - 1/2[I] > 0$) is a narrow band downstream of the I_2 injection point, with a peak value of $G = 2.6 \times 10^{11}$ cm^{-3}.

T_g has two local maxima. The first is due to discharge Joule heating, Frank–Condon heating and exothermic reactions of NO with O reaching 340 K adjacent to the downstream electrode. As the walls are held at 300 K, the gas rapidly cools by thermal conduction. A second local maximum occurs downstream of the first injection nozzle (up to 348 K) due to additional exothermic reactions of O and the newly injected NO.

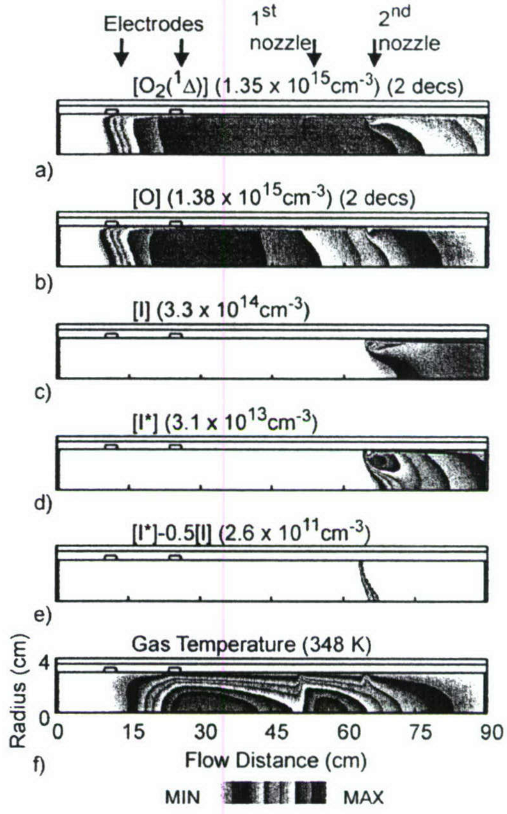

Figure 3. Neutral species densities and T_g for the base case. 36 sccm of pure NO was injected through the first nozzle and 100 sccm of $He/I_2 = 99/1$ was injected through the second nozzle. Densities of (*a*) $O_2(^1\Delta)$, (*b*) O, (*c*) I, (*d*) I*, (*e*) inversion density ([I*]-0.5[I]) and (*f*) gas temperature. The scales are linear except for $O_2(^1\Delta)$ and O which are plotted on a 2-decade log scale. Injection of NO decreases the flow of O and injection of I_2 consumes $O_2(^1\Delta)$. Exothermic reactions at both injection points produce local maxima in T_g.

To investigate the consequences of NO in the inlet flow over a wider parameter space, the plug flow model *GlobalKIN* was used. We first addressed the importance of NO^- and NO_2^- in the reaction mechanism and their effects on the densities of electrons, $O_2(^1\Delta)$ and $O_2(^1\Sigma)$. The densities of these species are shown along the axis of the discharge in figure 4 for a 3 Torr mixture of $He/O_2/NO = 60/30/10$ with 40 W power deposition. A high mole fraction of NO was used as an extreme case. When including NO^- and NO_2^- the peak electron density decreased approximately 10% from 1.4×10^{10} cm^{-3}. The reduction in n_e results in large part from the attachment of electrons to NO through 3-body reactions similar to those for O_2^- formation (equation (7)) and dissociative attachment to NO. The changes in densities of $O_2(^1\Delta)$ and $O_2(^1\Sigma)$ were relatively small (<5%) and could be attributed to the fact that n_e decreases and T_e increases modestly (0.05–0.1 eV from ≈2.0 eV) with the inclusion of NO^- and NO_2^-. (Recall that electron impact excitation of $O_2(^1\Delta)$ is maximum for T_e = 1–1.5 eV.) The density of O atoms was relatively independent on the inclusion of NO^- and NO_2^-. Based on these trends, we can expect results from *nonPDPSIM* (which do not include NO^- and NO_2^- in the reaction mechanism) to over-predict $O_2(^1\Delta)$ densities by a few per cent.

The consequences of NO in the inlet flow on the maximum densities of charged species, T_g, T_e, and power deposition into different species by electron impact are shown in figure 5 for 3 Torr and 40 W. A modest increase in n_e, from 1.1×10^{10} cm^{-3} to 1.25×10^{10} cm^{-3}, occurs as the NO mole fraction is increased from 0 to 10% due to the higher rates of ionization with NO in spite of a decrease in the positive and negative

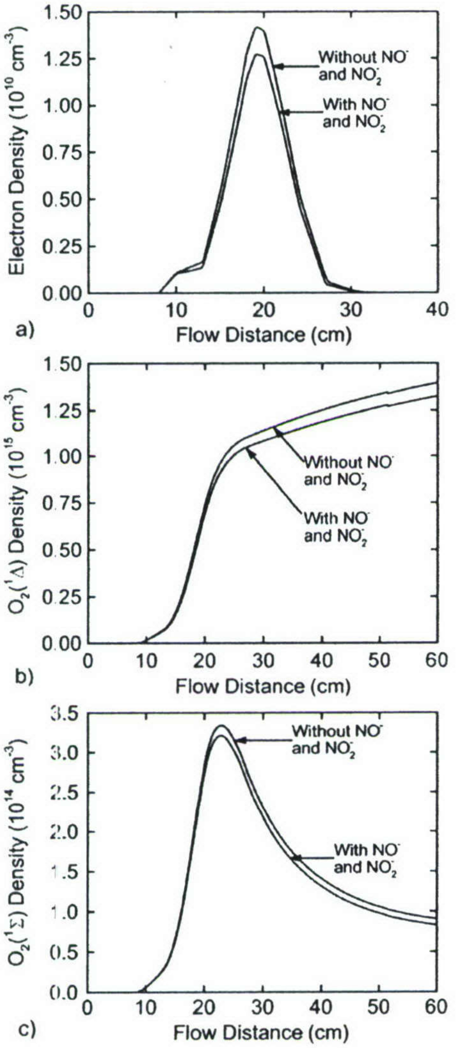

Figure 4. Dependence of plasma characteristics on the inclusion of NO^- and NO_2^- for 3 Torr, 40 W, He/O_2/NO = 60/30/10 and 6 slpm. Densities of (*a*) electrons, (*b*) $O_2(^1\Delta)$ and (*c*) $O_2(^1\Sigma)$. The densities of O did not show any noticeable variation. These results are from the plug flow model. Inclusion of these negative ions produces nominal changes in excited state densities.

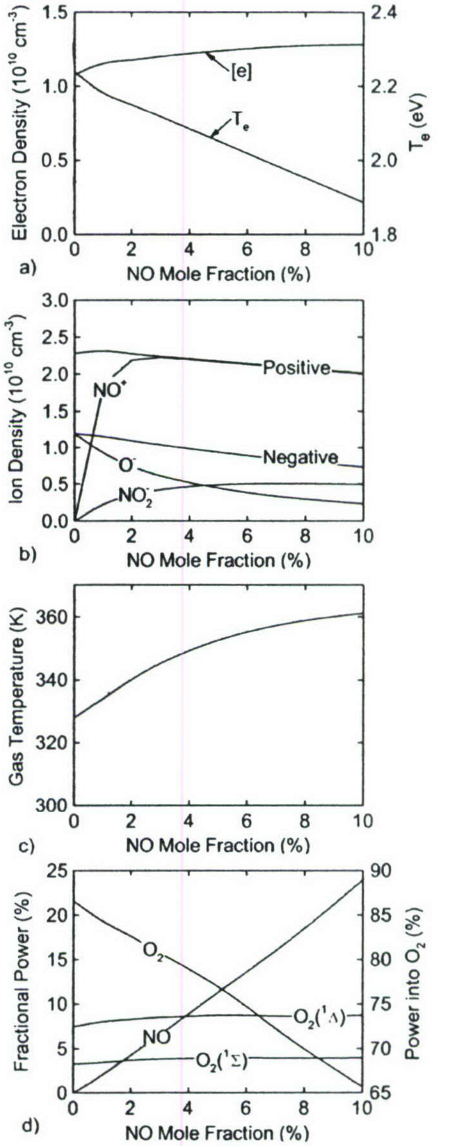

Figure 5. Plasma and gas characteristics while varying the NO mole fraction for 3 Torr, 40 W and a 6 slpm flow of He/O_2/NO = 70 − x/30/x. (*a*) Maximum n_e, (*b*) maximum positive- and negative-ion densities, (*c*) maximum T_g and (*d*) fractional power deposition into O_2 and NO, and in producing $O_2(^1\Delta)$ and $O_2(^1\Sigma)$. These results are from the plug flow model and from calculations of EEDs. In spite of NO consuming a large fraction of the power, the decrease in T_e increases the rate of excitation of $O_2(^1\Delta)$ and so there is not a large change in power dissipated in exciting $O_2(^1\Delta)$.

ion densities. The increase in n_e results from the density of negative ions decreasing more rapidly than the positive ions when increasing the mole fraction of NO. The positive ion density decreases from $2.3 \times 10^{10}\,\mathrm{cm}^{-3}$ to $2.0 \times 10^{10}\,\mathrm{cm}^{-3}$ while the decrease in negative ion density is $1.2 \times 10^{10}\,\mathrm{cm}^{-3}$ to $0.75 \times 10^{10}\,\mathrm{cm}^{-3}$. T_e decreases from 2.2 to 1.9 eV as the NO mole fraction is increased from 0 to 10%. The reduction in T_e is due to the additional power loss resulting from electron impact on NO when substituting NO for He and the reduction in the average ionization potential thereby enabling the discharge to be self-sustained with a lower value of T_e. This trend is partially offset by the additional attachment probability represented by NO.

While the total ion densities gradually decrease with increasing NO mole fraction, the densities of individual ions show more variation. In the absence of NO, O_2^+ forms the majority (>99%) of the positive ions. However with as little as 1–2% of NO, the majority ion is NO^+. This is due to charge exchange reactions between O_2^+ and NO. The dominant negative ion in the absence of NO is O^-, and as the NO mole fraction is increased, the density of NO_2^- ions increases, a result of charge exchange between O^- and NO_2 (equation (17)).

T_g increases with NO mole fraction primarily due to the exothermicity of reactions between O, NO and NO_2

(equations (18) and (19)). In the absence of NO, the maximum value of T_g is 328 K (increasing from the inlet value of 300 K). This value increases to 362 K with 10% NO. The peak gas temperatures occur just downstream of the discharge region. With large NO mole fractions, the contribution of Frank–Condon gas heating due to dissociation of NO can be more than a few per cent.

The fractional power deposited into NO increases nearly linearly with the NO mole fraction, increasing to 25% for an NO mole fraction of 10%. (Note that these values were computed using the actual mole fractions of species in the discharge and not the inlet conditions.) Correspondingly, the power deposition into O_2 decreases, from more than 85% in the absence of NO to 66% for an NO mole fraction of 10%. (Little power is dissipated by He.) In spite of the fraction of discharge power dissipated in O_2 decreasing, the power expended in exciting $O_2(^1\Delta)$, α, was relatively constant, reaching a shallow maximum of 8.7% for a NO mole fraction of 5%. As the NO mole fraction increases, T_e decreases from 2.2 to 1.9 eV thereby increasing the efficiency of $O_2(^1\Delta)$ production by electron impact [11]. Fortuitously, a combination of decreasing power dissipated by O_2 and an increase in the efficiency of exciting of $O_2(^1\Delta)$ maintains the total power expended in exciting $O_2(^1\Delta)$ relatively constant. This is not necessarily a general result but lowering T_e is generally beneficial. Similar trends are seen for $O_2(^1\Sigma)$ as the fractional power expended in exciting $O_2(^1\Sigma)$ increases slightly from 3.2% to 3.9% as the NO mole fraction increases to 10%.

The consequences of NO mole fraction in the inlet flow on the densities of O, $O_2(^1\Delta)$ and $O_2(^1\Sigma)$, and the yield of $O_2(^1\Delta)$ along the axis of the discharge are shown in figure 6 for the base case of 3 Torr, 40 W and 30% O_2. (Note that this yield is based on the mole fraction equivalent of O_2 for all oxygen species [11].) A flow of 100 sccm of $He/I_2 = 99/1$ is injected through the second nozzle. In the absence of NO, the density of $O_2(^1\Delta)$ increases to $1.2 \times 10^{15}\ \mathrm{cm}^{-3}$ due to electron impact excitation as the inlet flow passes through the plasma zone. The increase in the density of $O_2(^1\Delta)$ to $1.75 \times 10^{15}\ \mathrm{cm}^{-3}$ after the discharge zone results largely from quenching of a density of $0.4 \times 10^{15}\ \mathrm{cm}^{-3}$ of $O_2(^1\Sigma)$ by O atoms and excitation transfer from $O(^1D)$. The density of $O_2(^1\Delta)$ upstream of the I_2 injection point monotonically decreases with the addition of NO, from $1.75 \times 10^{15}\ \mathrm{cm}^{-3}$ without NO to $1.1 \times 10^{15}\ \mathrm{cm}^{-3}$ with 10% NO. A portion of this decrease results from an increase in the T_g when adding NO though the yield of $O_2(^1\Delta)$ also decreases from 5.9% when adding NO.

The production of $O_2(^1\Delta)$ is dominated by electron impact on O_2 and so is dependent on T_e and n_e. Since the power deposition producing $O_2(^1\Delta)$ is nearly constant, secondary processes must be responsible for the decrease in the yield of $O_2(^1\Delta)$ with increasing NO. One such secondary process is the production of $O_2(^1\Delta)$ by excitation transfer between $O(^1D)$ and O_2. The majority of $O(^1D)$ is produced by dissociative excitation of O_2 (equation (5)). Reactions of $O(^1D)$ with O_2 produces its excited states,

$$O(^1D) + O_2 \rightarrow O + O_2(^1\Sigma),\quad (k = 2.6 \times 10^{-11} \exp(67/T_g)\ \mathrm{cm}^3\ \mathrm{s}^{-1}), \tag{37}$$

$$O(^1D) + O_2 \rightarrow O + O_2(^1\Delta),\quad (k = 1.5 \times 10^{-12} \exp(67/T_g)\ \mathrm{cm}^3\ \mathrm{s}^{-1}). \tag{38}$$

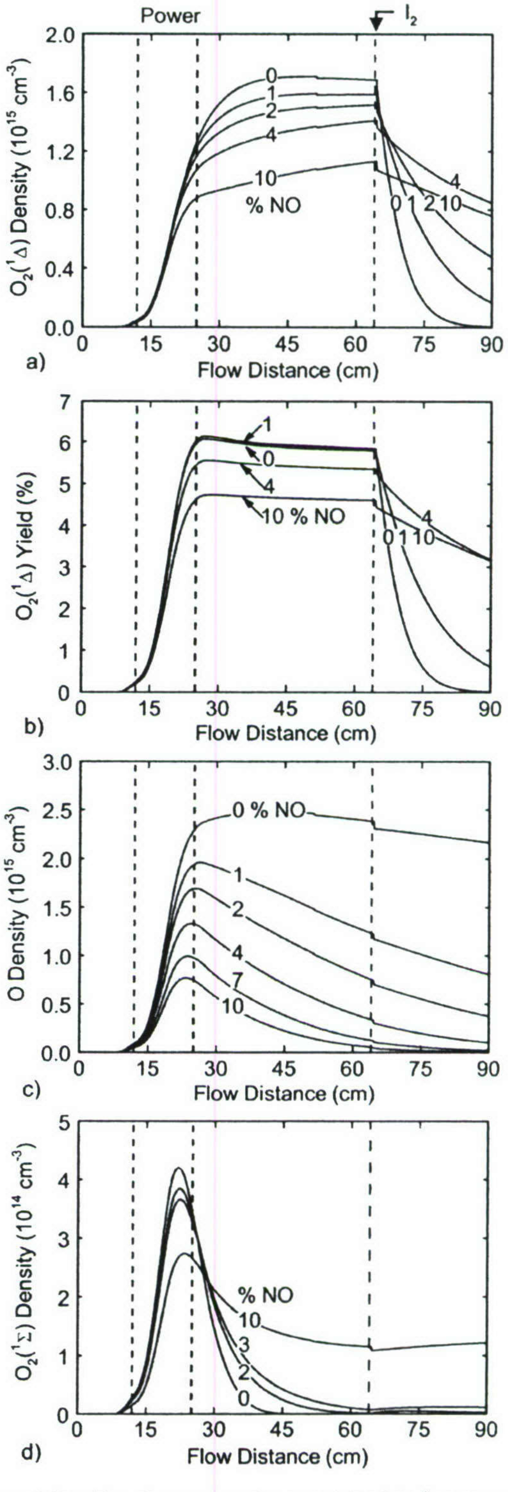

Figure 6. Densities of oxygen species and yield of $O_2(^1\Delta)$ along the axis of the tube while varying NO mole fraction for 3 Torr and 40 W for a 6 slpm flow of $He/O_2/NO = 70 - x/30/x$. 100 sccm of $He/I_2 = 99/1$ is injected through the second nozzle. (*a*) $O_2(^1\Delta)$, (*b*) yield of $O_2(^1\Delta)$, (*c*) O and (*d*) $O_2(^1\Sigma)$. These results are from the plug flow model. Increasing flows of NO decrease the flow of O atoms.

With the decrease in T_e with addition of NO, the production of $O(^1D)$ by electron impact dissociation of O_2 decreases and so these secondary sources of $O_2(^1\Delta)$ and $O_2(^1\Sigma)$ also decrease. Furthermore, both NO and NO_2 are quenchers of $O(^1D)$,

$$NO + O(^1D) \rightarrow NO + O, \quad (k = 4.0 \times 10^{-11}\,cm^3\,s^{-1}), \tag{39}$$

$$NO_2 + O(^1D) \rightarrow NO + O_2, \quad (k = 3.0 \times 10^{-10}\,cm^3\,s^{-1}), \tag{40}$$

$$NO_2 + O(^1D) \rightarrow NO_2 + O, \quad (k = 3.2 \times 10^{-10}\,cm^3\,s^{-1}). \tag{41}$$

So the addition of NO reduces the production of $O(^1D)$ and increases its rate of quenching, thereby reducing the production of $O_2(^1\Delta)$ by excitation transfer. The importance of the quenching reactions of $O(^1D)$ is demonstrated by excluding the reactions in equations (39)–(41) from the mechanism. For 10% NO in the flow, the yield of $O_2(^1\Delta)$ improved from 4.6% to 5.3% when quenching of $O(^1D)$ is eliminated. The quenching of $O_2(^1\Delta)$ by NO has a small rate coefficient ($3.5 \times 10^{-17}\,cm^3\,s^{-1}$) and so does not significantly contribute to the loss of $O_2(^1\Delta)$.

The density of O atoms increases monotonically through the discharge zone to a maximum value of $2.5 \times 10^{15}\,cm^{-3}$ in the absence of NO. (The small increase in the density of O after the discharge is mainly due to gas cooling.) With the addition of NO, the density of O atoms decreases throughout the flow-tube and, in particular, downstream of the discharge. This decrease is due to both the reduction in the rate of electron impact dissociation of O_2 by the decrease in T_e and the formation of NO_2 in reactions with NO. In the post-discharge region in the absence of NO, the majority of $O_2(^1\Sigma)$ is converted to $O_2(^1\Delta)$ through collisions with O and O_3. Due to the reduction of O atoms with increasing NO, the rates of quenching of $O_2(^1\Sigma)$ to $O_2(^1\Delta)$ are also smaller, leading to higher densities of $O_2(^1\Sigma)$ in the afterglow. Higher $O_2(^1\Sigma)$ densities are not necessarily bad since they help in dissociating I_2 but maintaining those densities does result in lower densities of $O_2(^1\Delta)$ that directly pump I^*.

The densities of I and I^*, and the optical gain at 1.315 μ are shown in figure 7 for the conditions of figure 6 (1 sccm of I_2 injected in a 100 sccm, $He/I_2 = 99/1$ flow). The gain was given by $\sigma([I^*] - 0.5[I])$ where σ is the stimulated emission cross-section. At pressures of less than tens of Torr, Doppler broadening dominates over pressure broadening, and so the stimulated emission cross-section can be approximated by [35],

$$\sigma = 1.33 \times 10^{-16} T_g^{-1/2}\,cm^2. \tag{42}$$

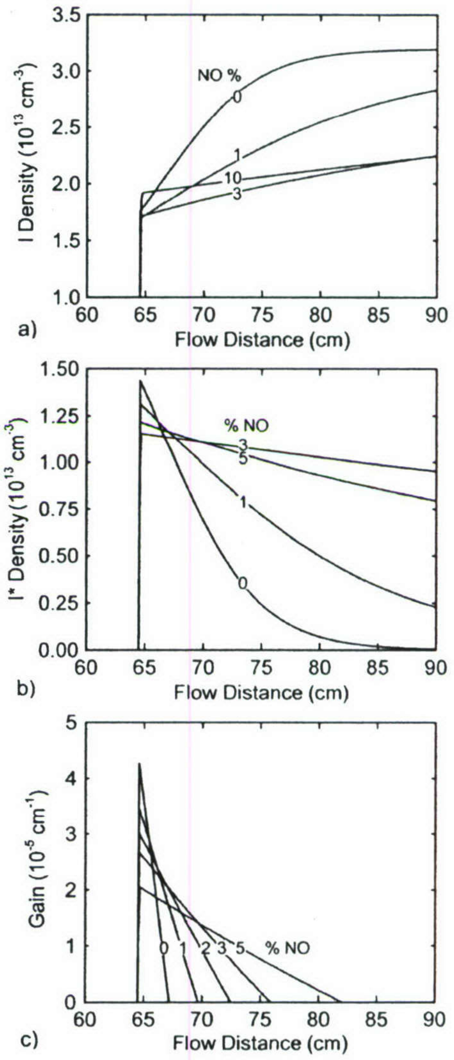

Figure 7. Densities of atomic iodine species as a function of inlet NO mole fraction for 3 Torr, 40 W, $He/O_2/NO = 70 - x/30/x$ and 6 slpm. 100 sccm of $He/I_2 = 99/1$ is injected through the second nozzle. Densities of (*a*) I, (*b*) I^* and (*c*) optical gain. These results are from the plug flow model. Low flows of NO produce the maximum peak gain whereas high flows of NO produce larger plumes of positive gain.

In the absence of NO, the density of I increases from $1.75 \times 10^{13}\,cm^{-3}$ at the I_2 injection point to $3.2 \times 10^{13}\,cm^{-3}$ downstream due in large part to the reaction of O atoms with I_2. The density of I^* is maximum at the injection point at $1.45 \times 10^{13}\,cm^{-3}$ and decreases to negligible values by the end of the flow tube due to the depletion of $O_2(^1\Delta)$ (the species responsible for the pumping reaction) and quenching by O atoms. Since the lifetime of I^* (125 μs for quenching by O) is short compared with flow times, the density of I^* does not appreciably accumulate in the discharge and its density is a reflection of instantaneous production and quenching rates. The end result is a peak gain of $4.2 \times 10^{-5}\,cm^{-1}$ within a centimetre of the I_2 injection point. Note that the rate of quenching of I^* by O is faster than that due to spontaneous emission (0.1 s) [33].

With injection of I_2 the density of $O_2(^1\Delta)$ decreases by virtue of excitation transfer and dissociative excitation of I_2, and reactions with I which pumps I^*. In the absence of NO, the density of $O_2(^1\Delta)$ is fully depleted by the reactions. In the absence of NO there is also a large density of O atoms at the injection point which react with I_2 producing IO and I. Since the rate of dissociation of I_2 by $O_2(^1\Delta)$ and $O_2(^1\Sigma)$ is slower than by O atoms there is a larger density of I available for $O_2(^1\Delta)$ to react with, and so the $O_2(^1\Delta)$ is rapidly depleted.

As the flow of NO is increased, the flow of O atoms decreases, resulting in a lower rate of dissociation of I_2 and fewer I atoms. With the lower density of I the reactivity of $O_2(^1\Delta)$ is lower; and so its density decreases less rapidly after injection of I_2.

The production of I^* results from reactions of $O_2(^1\Delta)$ with I while the quenching of I^* is largely due to collisions with O atoms. Increasing the NO mole fraction decreases the O atom density downstream thereby lowering the rates of quenching of I^* and extending its plume beyond the I_2 injection point. However, having too large an NO mole fraction results in too low rates of dissociation of I_2 and hence poor utilization of $O_2(^1\Delta)$. The end result is that the region over which positive gain can be sustained is maximum for an intermediate mole fraction of NO of 3%.

The purpose of flowing NO (or injecting NO_2) is largely to manage the O atom density and so control the quenching of I^* by O. A sensitivity study was conducted of the rate coefficient for this quenching reaction from the nominal value of $8 \times 10^{-12}\,\mathrm{cm^3\,s^{-1}}$. The densities of $O_2(^1\Delta)$ and I^*, and gain are shown in figure 8 while varying this rate coefficient from 0 to $1.0 \times 10^{-11}\,\mathrm{cm^3\,s^{-1}}$. In the absence of quenching, the densities of I^* and $O_2(^1\Delta)$ do not significantly decrease downstream of the I_2 injection point. In the absence of quenching by O, the predominant quencher of I^* is O_2 and this quenching produces $O_2(^1\Delta)$. The forward and backward pumping reactions (equations (25) and (26)) reach an equilibrium where the I^* and $O_2(^1\Delta)$ densities gradually decrease due to minor quenchers of I^* (such as NO and $O_2(^1\Delta)$) and radiative relaxation. When increasing the rate coefficient for quenching I^*, the density of I^* decreases proportionately. By removing I^* in this manner the rate of the backward reaction with O_2 decreases and so does the density of $O_2(^1\Delta)$. The extent of positive gain is progressively limited to the few cm beyond the I_2 injection point as the quenching of I^* increases, though the peak value of gain is not particularly sensitive to the rate coefficient.

The densities of $O_2(^1\Delta)$ and O, and T_g 2 cm upstream of the second nozzle are shown in figure 9 as a function of power deposition and NO mole fraction in the inlet flow. In general, T_g increases with power deposition and with NO addition reaching a maximum of 480 K with 400 W power deposition and 10% NO in the inlet flow. Increasing power deposition produces more electron impact dissociation of O_2 and NO, producing larger densities of O atoms. However, increasing NO mole fractions decreases the density of O atoms by virtue of scavenging by NO and NO_2 and decreasing T_e.

The density of $O_2(^1\Delta)$ decreases with NO addition, as discussed above, and increases with power deposition. The saturation in the density $O_2(^1\Delta)$ at $6.5 \times 10^{15}\,\mathrm{cm^{-3}}$ at higher powers is due in part to the depletion of O_2 by electron impact dissociation and in part to gas heating. For example, with 400 W and 0% NO, the fractional dissociation of O_2 is 68%. The addition of NO reduces the depletion of O_2 by both reducing the rate of O_2 dissociation and by recycling O atoms back to O_2. For example, for 10% NO addition and 400 W, the fractional dissociation decreases to 36%. The yield of $O_2(^1\Delta)$ saturates with power at 18% due to the depletion of O_2.

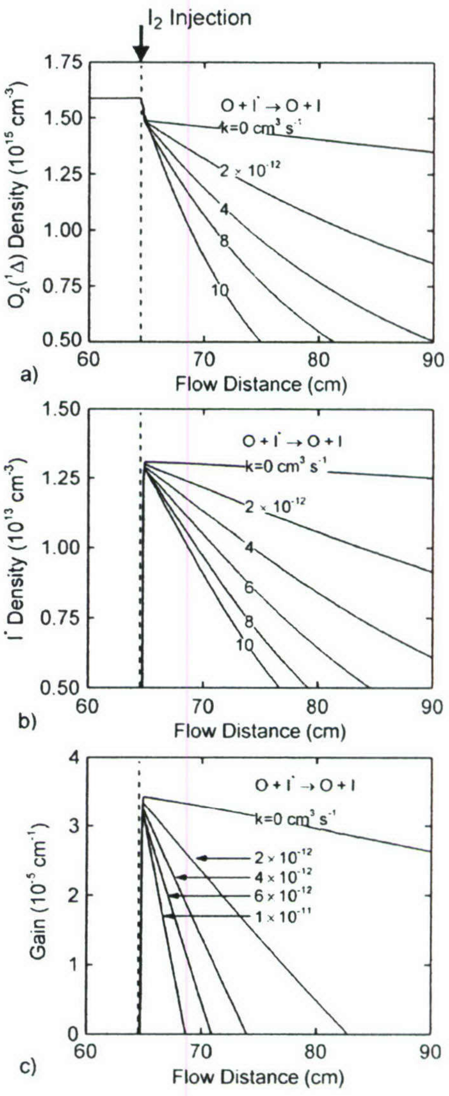

Figure 8. Sensitivities of the value of the rate coefficient for the quenching reaction between O and I^* on the post-discharge kinetics for 3 Torr, 40 W, $He/O_2/NO = 69/30/1$ and 6 slpm. 100 sccm of $He/I_2 = 99/1$ is injected through the second nozzle. Densities of (*a*) $O_2(^1\Delta)$, (*b*) I^* and (*c*) optical gain. These results are from the plug flow model.

The densities of I and I^*, and gain as function of power deposition and NO mole fraction are shown in figure 10 at a location of 2 cm downstream from the I_2 injection point. This mixing length of 2 cm was chosen based on previous studies for similar flow conditions [36]. The inlet flow has 30% O_2 and the flow injected through the second nozzle is 1 sccm of I_2 in a 100 sccm flow of $He/I_2 = 99/1$. At low power deposition, the density of I is large, $(2.2–2.3) \times 10^{13}\,\mathrm{cm^{-3}}$, because the yields of $O_2(^1\Delta)$ are low enough that the pumping of I to I^* is slow. As the yield of $O_2(^1\Delta)$ increases at higher powers, the pumping reactions reduce the density of I and increase that of I^*, leading to an increase in gain. However, at large power deposition, the density of O increases whereas that of $O_2(^1\Delta)$ saturates. This leads to an increased rate of quenching of I^* by O which reduces the density of I^* and increases that of I. The end result is a reduction in gain.

Increasing NO in the inlet flow reduces the density of O atoms at the injection point, thereby reducing the rate of

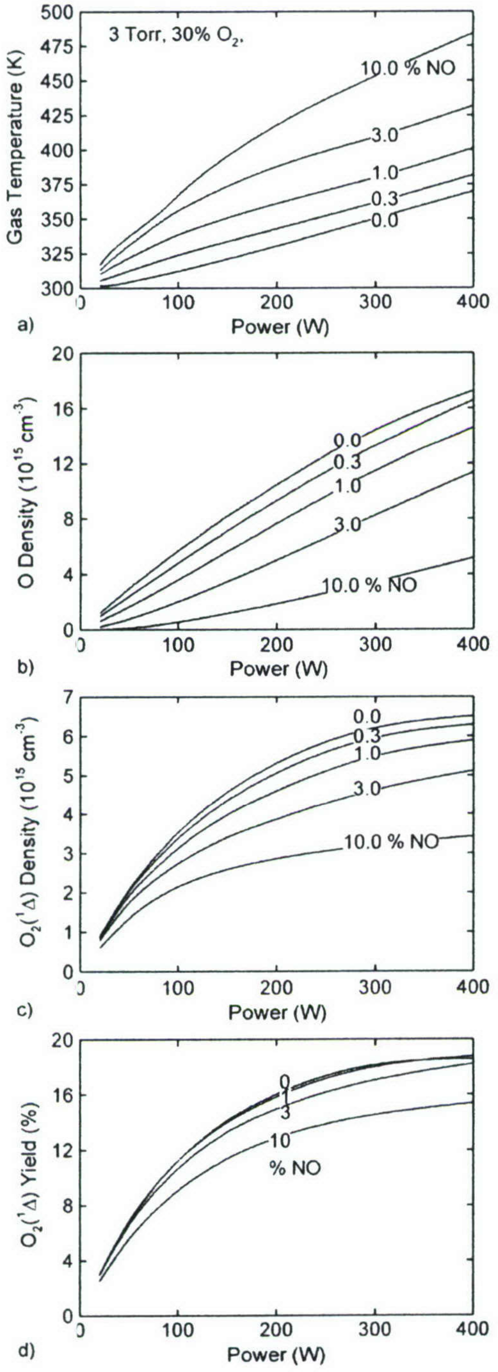

Figure 9. Consequences of power deposition and NO mole fraction on the neutral gas properties for 3 Torr, He/O$_2$/NO $= 70 - x/30/x$ and 6 slpm. (*a*) T_g, (*b*) density of O, (*c*) density of O$_2(^1\Delta)$ and (*d*) yield of O$_2(^1\Delta)$. O$_2(^1\Delta)$ densities saturate with power due to a high degree of dissociation of O$_2$. These results are from the plug flow model and the values are for 2 cm upstream of the second nozzle.

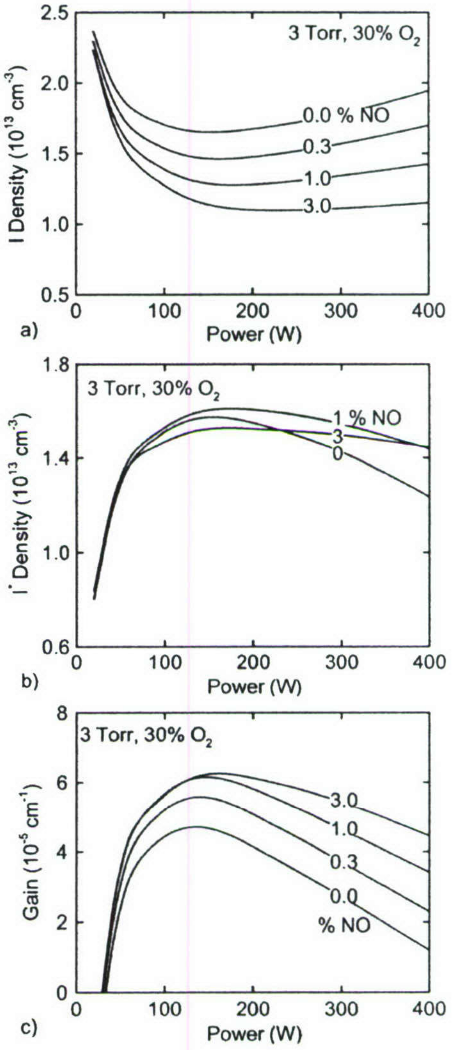

Figure 10. Consequences of power deposition and NO mole fraction on iodine species and gain for 3 Torr, He/O$_2$/NO $= 70 - x/30/x$ and 6 slpm. Densities of (*a*) I and (*b*) I* and (*c*) optical gain. These results are from the plug flow model and the values are for 2 cm downstream of the second nozzle. Gain is maximum at high power only with high flow rates of NO.

dissociation of I$_2$ and the density of I atoms. The reduction in O by addition of NO also reduces the quenching of I* by O, making the gain predominantly dependent on the yield of O$_2(^1\Delta)$. As a result, for 3% NO, the gain decreases from 6.0 $\times 10^{-5}$ to 4.3×10^{-5} cm^{-1} between 150 and 400 W, whereas in the absence of NO, the gain reduces by nearly a factor of 3.

The eCOIL system may operate in either power limited or iodine limited modes. In the iodine limited mode, the flow of O$_2(^1\Delta)$ and O generated by the discharge fully utilizes the injected flow of I$_2$, and so gain saturates with increasing power. To some degree (quenching of I* and depletion of O$_2$ aside), this is the mode that applies to the results shown in figure 10. In the power limited mode, the flow of O$_2(^1\Delta)$ and O is insufficient to fully utilize the injected flow of I$_2$, and so gain saturates with flow of I$_2$.

These modes of operation are demonstrated by varying power deposition and I$_2$ flow rate. The densities of I and I*, and gain are shown 2 cm downstream of the I$_2$ injection point in figure 11 for a 6 slpm inlet flow of He/O$_2$/NO $= 67/30/3$

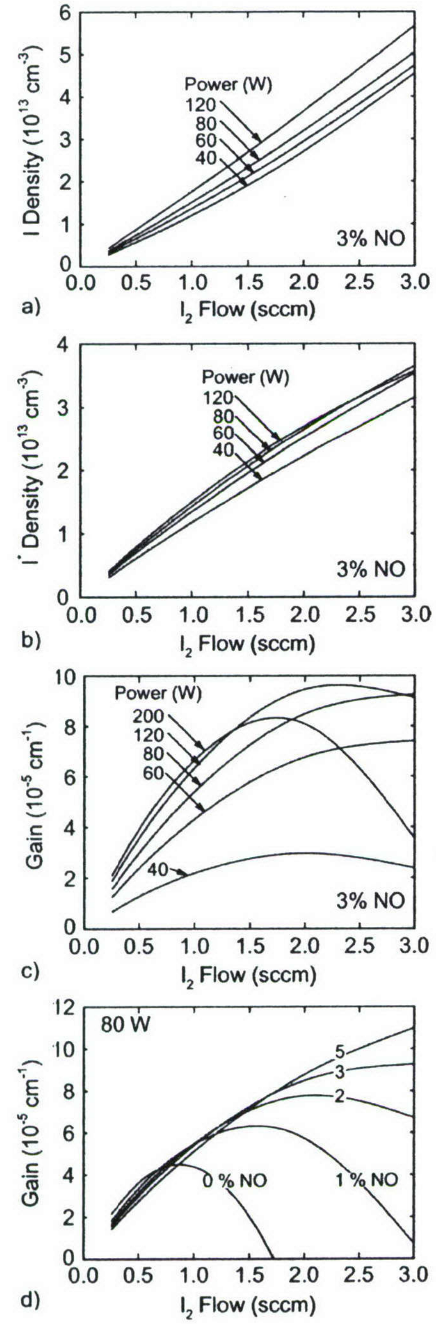

Figure 11. Iodine species densities and gain while varying the I_2 flow rate through the second nozzle. Densities of (*a*) I and (*b*) I*, and (*c*) optical gain for 3% NO in the inlet flow and (*d*) gain for 80 W power deposition. These results are from the plug flow model and the values are for 2 cm downstream of the second nozzle. Varying power and I_2 flow rate switches between the power limited and I_2 limited regimes.

while varying power and I_2 flow rate. The densities of I and I* increase nearly linearly with the flow of I_2 and increase sub-linearly with power deposition. For example, with a flow of 3 sccm of I_2, the density of I is $4.6 \times 10^{13}\ \text{cm}^{-3}$ with 40 W and only $5.6 \times 10^{13}\ \text{cm}^{-3}$ with 120 W. For these conditions the production of I is limited by the availability of I_2 as the injected I_2 is nearly completly dissociated by reactions with O, $O_2(^1\Delta)$ and $O_2(^1\Sigma)$ for all power depositions. The production of I* is limited by the yield of $O_2(^1\Delta)$ which does not scale linearly with power at higher power depositions. As a consequence the density of I* saturates with power deposition with large flows of I_2. This saturation is exacerbated at high power depositions (or low NO mole fractions) by large densities of O which quench I*.

With a power deposition of 40 W, gain increases with flow rate of I_2 (shown in figure 11(*c*)) saturating at $3 \times 10^{-5}\ \text{cm}^{-1}$ at 2 sccm, a consequence of being in a power limited regime. As the power increases the gain increases, and the I_2 flow rate at which the maximum gain is obtained also increases. For example, for 80 W, the gain saturates at $9 \times 10^{-5}\ \text{cm}^{-1}$ for an I_2 flow rate of 3 sccm. The higher power deposition is able to better utilize the increased flow of I_2. As the power further increases, the peak gain increases only moderately and decreases above 200 W as the system transitions to an I_2 limited regime and the densities of $O_2(^1\Delta)$ saturate.

The consequences of flow rates of NO and I_2 on gain are shown for 80 W in figure 11(*d*). For a fixed power, increasing the mole fraction of NO at the inlet reduces the density of O atoms which reduces the quenching of I*. Increasing the NO mole fraction increases the range of I_2 flow rates over which the positive gain can be achieved and increases the flow rate of I_2 at which the maximum gain is obtained. For example, the maximum gain in the absence of NO is $4.2 \times 10^{-5}\ \text{cm}^{-1}$ for an I_2 flow rate of 0.8 sccm. As the rate of quenching of I* decreases with increasing NO flow, gain increases to more than $1.2 \times 10^{-4}\ \text{cm}^{-1}$ for an inlet mole fraction of 5% NO and flow rate of 3 sccm of I_2.

The consequences of flow dynamics on the densities of $O_2(^1\Delta)$ and I* are shown in figure 12 with results from *nonPDPSIM*. The densities of $O_2(^1\Delta)$ and I* are shown for 80 W and a 6 slpm inlet flow of $He/O_2/NO = 68/30/2$. A 100 sccm flow of He/I_2 was injected from the second nozzle with the I_2 flow varied from 0.5 to 3 sccm. As the flow passes through the discharge zone, electron impact produces $O_2(^1\Delta)$ at large radius first where the plasma density is highest. Diffusion homogenizes the density of $2.5 \times 10^{15}\ \text{cm}^{-3}$ across the radius by 10–12 cm downstream of the plasma zone. At and after the I_2 injection point, the densities of $O_2(^1\Delta)$ decrease due to excitation transfer to I_2 and pumping of I*, first at the outer radius where the I_2 is injected and on axis 4–5 cm downstream. With low flow rates of I_2 ($\leqslant$0.5 sccm), the $O_2(^1\Delta)$ is not significantly depleted whereas with flow rates $\geqslant$1 sccm, the flow of $O_2(^1\Delta)$ is largely consumed by reactions with I_2 and I.

The densities of I* are maximum adjacent to the second nozzle where densities of both $O_2(^1\Delta)$ and I_2 are largest. The I* diffuses radially to the centre of the discharge 4–5 cm downstream of the injection point. For small flow rates of I_2, the densities of I are smaller, and hence consumption of $O_2(^1\Delta)$ in pumping the I* is gradual, leading to a longer distance over which significant amounts of I* are present. At high flow rates of I_2, $O_2(^1\Delta)$ is largely consumed in the vicinity of the injection point and so I* does not extend appreciably beyond that point.

The densities of I and I*, and the gain obtained with *nonPDPSIM* at a radius of 1.5 cm are shown in figure 13 for

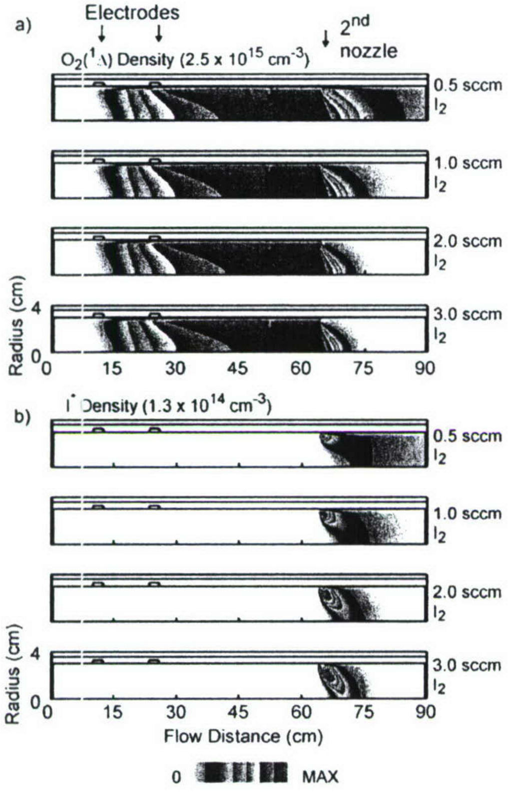

Figure 12. Excited state densities while varying the I_2 flow rate through the second nozzle. (*a*) $O_2(^1\Delta)$ and (*b*) I^*. These results, obtained with *nonPDPSIM*, are for 3 Torr, 80 W power deposition, and 6 slpm flow of He/O_2/NO = 68/30/2.

the conditions of figure 12. Similar to the results obtained with *GlobalKIN*, the densities of I increase with increasing flow rate of I_2 indicating that the system is in an I_2 limited regime. The densities of I^* also increase with increasing I_2 mole fraction reaching a maximum 3–4 cm downstream of the injection point. I^* is rapidly quenched by the O atoms whose densities are commensurate with $O_2(^1\Delta)$. At lower I_2 mole fractions, the densities of I^* do not decrease rapidly downstream of the injection point due to the availability of $O_2(^1\Delta)$ to continue to pump I to I^*.

The maximum gain (at a radius of 1.5 cm) is 10^{-4} cm^{-1} for an I_2 flow of 3 sccm. The axial extent of positive gain is limited by the depletion of $O_2(^1\Delta)$. Lower flow rates of I_2 produce lower gain but the axial extent of gain is greater. A comparison of maximum gain obtained with *GlobalKIN* and *nonPDPSIM* as a function of flow rate of I_2 is shown in figure 13(*d*). The predicted gains are commensurate except at large flow rates of I_2 where the gain with *GlobalKIN* is significantly higher than with the 2d model. The lack of axial transport in the plug flow model produces artificially high rates of reaction between O and $O_2(^1\Delta)$ with I and I_2, which increases predicted gain.

5. NO_2 injection

In experimental demonstrations of laser oscillation and significant gain in eCOIL systems, NO_2 was usually injected downstream of the plasma zone and prior to the addition of I_2 [9, 34]. Comparisons between predictions from *GlobalKIN* and experiments by Carroll *et al* [34] using this strategy are shown in figure 14. The conditions are a 10 Torr, 26.9 slpm

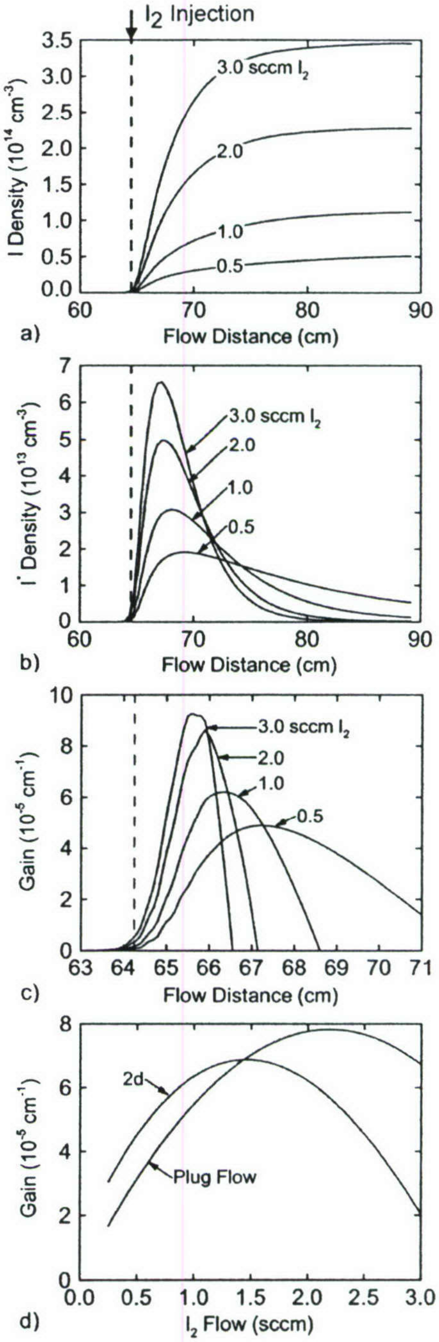

Figure 13. Iodine species densities and gain at a radius of 1.5 cm as a function of the flow rate of I_2 through the second nozzle. Densities of (*a*) I and (*b*) I^*, (*c*) gain and (*d*) comparison of the plug flow and 2D models for gain 2 cm downstream of the second nozzle. These results are from *nonPDPSIM* for 3 Torr, 80 W power deposition and 6 slpm flow of He/O_2/NO = 68/30/2. 100 sccm of He/I_2 is flowed through the second nozzle.

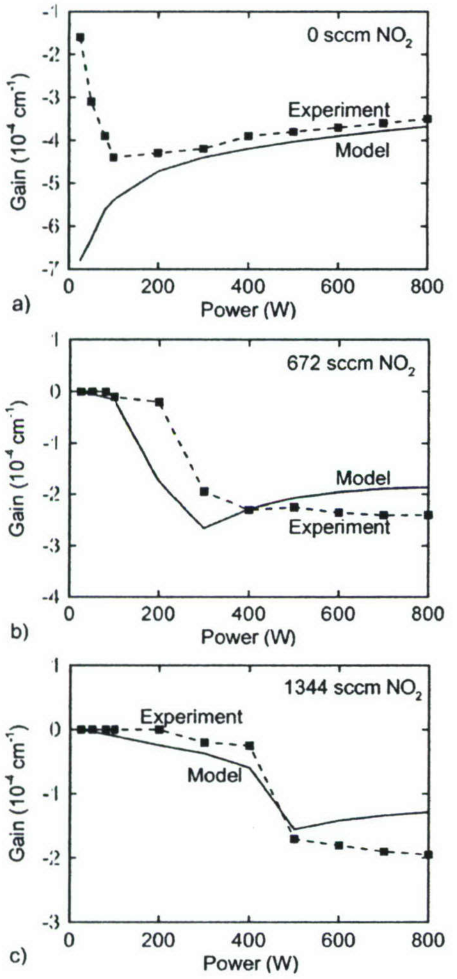

Figure 14. Gain in a subsonic flow for 10 Torr, 26.9 slpm of $He/O_2 = 80/20$, 25–800 W, with 10.8 sccm of I_2 injected through the second nozzle. (a) 0 sccm NO_2, (*b*) 672 sccm NO_2 and (*c*) 1344 sccm NO_2 through the first nozzle. Experimental values are from [34].

(20 mmol s^{-1}) inlet flow of $He/O_2 = 80/20$ and 25–800 W followed by injection of 0–1344 sccm (0–1 mmol s^{-1}) NO_2 and injection of 10.7 sccm (0.008 mmol s^{-1}) of I_2, equivalent to few per cent of the $O_2(^1\Delta)$ flow rate. The diameter of the reactor is 4.9 cm and I_2 injection is 20 cm downstream of the NO_2 injection point. The power deposition spans nearly 25 cm due to a larger separation between electrodes in the experiment. The experimental measurements were made 10 cm downstream of the I_2 injection point in a subsonic (high gas temperature flow) and so gains are negative.

With the exception of low powers and low flow rates of NO_2, the experimental trends are captured by *GlobalKIN*. Addition of NO_2 prior to injection of I_2 scavenges some of the O atoms in the flow and so reduces the quenching of I* by O atoms. Higher powers produce larger flows of O atoms as well as more $O_2(^1\Delta)$ but the quenching of I* dominates. Increasing the NO_2 flow rate increases the scavenging of O atoms and extends the power prior to transitioning to large negative gain.

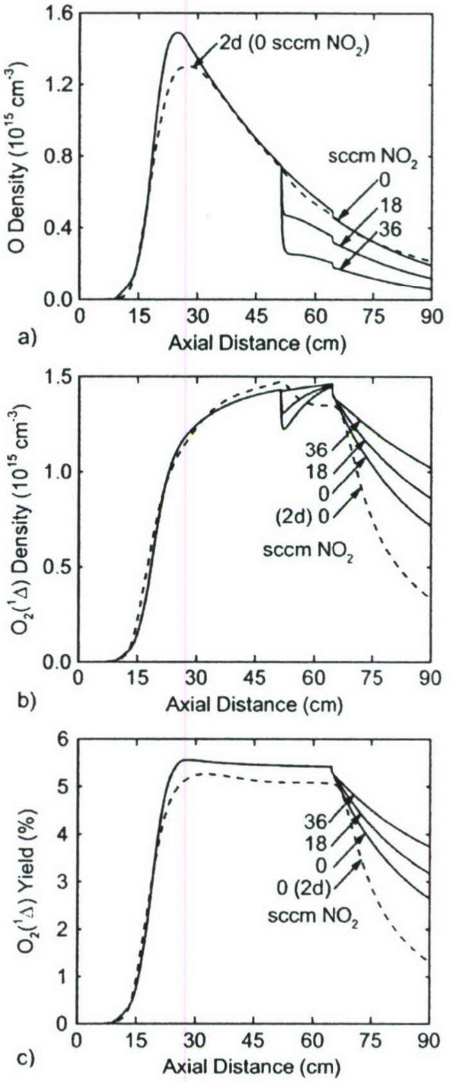

Figure 15. Consequences of injection of NO_2 through the first nozzle for 3 Torr, 40 W, $He/O_2/NO = 67/30/3$ and 6 slpm. 36 sccm of He/NO_2 mixture is injected through the first nozzle. Densities of (*a*) O and (*b*) $O_2(^1\Delta)$ and (*c*) yield of $O_2(^1\Delta)$. Addition of NO_2 rapidly consumes the O atoms. These results are from the *GlobalKIN*, the plug flow model. Values from the 2D *nonPDPSIM* are shown without NO_2 injection.

Since NO_2 is more effective than NO in scavenging of O atoms, we investigated NO_2 injection through the first nozzle. The conditions are a 3 Torr, 6 slpm inlet flow of $He/O_2/NO = 67/30/3$ and discharge power of 40 W. A He/NO_2 flow of 36 sccm was injected through the first nozzle with the fraction of NO_2 being varied. As before a 100 sccm flow of $He/I_2 = 99/1$ was injected through the second nozzle.

The consequences of NO_2 flow rate through the first nozzle on the densities of O and $O_2(^1\Delta)$, and yield of $O_2(^1\Delta)$ are shown in figure 15. These results are from *GlobalKIN* with a result from *nonPDPSIM* without NO_2 injection for comparison. The injection of NO_2 produces a decrease in the O atom density due to the titration of O by NO_2 and the

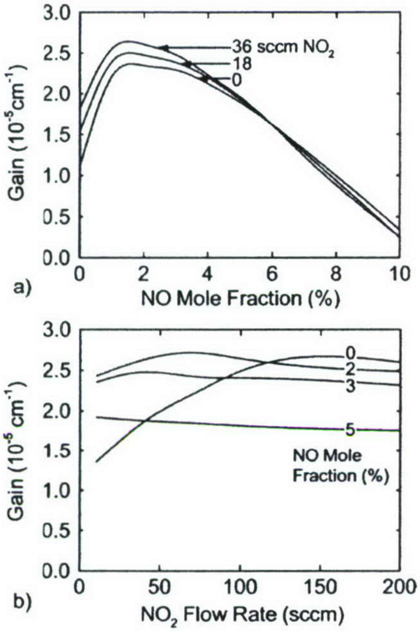

Figure 16. Gain when including NO in the inlet flow and injecting NO_2 through the first nozzle for 3 Torr, 40 W, $He/O_2/NO = 70 - x/30/x$ and 6 slpm. 100 sccm of $He/I_2 = 99/1$ is injected through the second nozzle. (*a*) Gain as a function of NO mole fraction and (*b*) gain as a function of NO_2 flow rate. These results are from the plug flow model. Maximum gain is obtained at low NO flow rates and high NO_2 injection.

conversion of O to O_2, respectively. As the NO_2 flow rate increases to 36 sccm the O atom densities decrease by a factor of 3–4 just downstream of the injection point due to the more rapid rate of reaction with O (compared with that of NO). The heat of reaction between NO_2 and O locally increases the gas temperature leading to a reduction in the density of $O_2(^1\Delta)$ near the first nozzle due to rarefaction. Note, however, that the yield of $O_2(^1\Delta)$ is not affected by NO_2 injection because NO_2 does not appreciably quench $O_2(^1\Delta)$. The reduction in the densities of O with NO_2 injection implies that the quenching of I^* by O is reduced. This produces a reduction in the amount of $O_2(^1\Delta)$ used in pumping the I^*. Hence, downstream of the second nozzle, the yield of $O_2(^1\Delta)$ is higher for larger NO_2 mole fractions. Results from *GlobalKIN* and *nonPDPSIM* are in general agreement except downstream of the I_2 injection point due to the artificially higher rates of reaction upon injection of I_2.

Gain is shown in figure 16 for 2 cm downstream from the second nozzle as a function of NO mole fraction in the inlet flow and flow rate of NO_2 through the second nozzle. The flow conditions are 3 Torr and 40 W power deposition. Having NO in the inlet flow affects the production of $O_2(^1\Delta)$ as discussed above as well as managing the O atoms density. Injection of NO_2 downstream of the discharge largely only affects the density of O atoms (and gas temperature). As such, at low values of NO flow, injection of NO_2 is effective in managing the O atom density and larger flow rates tend to maximize gain by reducing quenching of I^* by O atoms. At large flow rates of NO, the management of O atoms is dominated by reactions with NO, and so the injection of NO_2 is less effective. Since there is a deleterious effect on $O_2(^1\Delta)$ production by having large flows of NO through the discharge, managing the O atom density with injection of NO_2 is likely the optimum strategy.

6. Concluding remarks

The consequences of NO in the inlet flow of a He/O_2 plasma and its flowing afterglow, and NO_2 and I_2 injection on the post-discharge kinetics of the eCOIL were investigated using plug flow and 2D models. The addition of NO to the inlet flow through the discharge produces a reduction in T_e and a modest increase in n_e resulting in the densities and yields of $O_2(^1\Delta)$ being generally lower with NO. Including NO in the flow reduces the density of O atoms both by a reduction in the electron impact dissociation of O_2 and by exothermic reactions of O with NO. This proves beneficial to improving optical gain by reducing the quenching of I^* by O atoms. At higher power deposition, the dissociation of O_2 saturates the yield of $O_2(^1\Delta)$. By virtue of adding NO to the inlet flow, the reduction in T_e reduces the rate of dissociation of O_2. Even though the yields of $O_2(^1\Delta)$ were generally lower, the optical gain was generally higher when the NO mole inlet mole fraction was between 1% and 3%.

The eCOIL system can operate in power limited and I_2 limited regimes. At low flow rates, I_2 is nearly totally dissociated and so the densities of I depend largely on the I_2 flow rate. Upon increasing the flow rate of I_2, the system transitions to a power limited regime and higher powers are required to optimize gain. Small flows of NO_2 in the post-discharge region can be used to fine tune the gain. The addition of NO_2 rapidly consumes O atoms without significantly changing other parameters (other than T_g) and so increases the optical gain. The injection of NO_2 was most effective at low flow rates of NO. In general, management of the O atom density is critical to optimizing gain due to its rapid rate of quenching of I^*.

Acknowledgment

This work was supported by the Air Force Office of Scientific Research and the National Science Foundation (CTS-0520368).

References

[1] Hicks A, Utkin Yu G, Lempert W R, Rich J W and Adamovich I V 2006 *Appl. Phys. Lett.* **89** 241131
[2] Braginsky O V *et al* 2006 *J. Phys. D: Appl. Phys.* **39** 5183
[3] Verdeyen J T *et al* 2006 *Appl. Phys. Lett.* **89** 101115
[4] Kodymová J and Spalek O 1998 *Japan. J. Appl. Phys.* **37** 117
[5] Fujii H, Yoshida S, Iizuka M and Atsuta T 1990 *J. Appl. Phys.* **67** 3948
[6] Hill A 2000 The next generation of controlled avalanche discharge gas lasers *Int. Conf. on Lasers (Albuquerque, NM)*
[7] Hicks A *et al* 2005 *J. Phys. D: Appl. Phys.* **38** 3812
[8] Ionin A A *et al* 2003 *J. Phys. D: Appl. Phys.* **36** 982
[9] Palla A D, Carroll D L, Verdeyen J T and Solomon W C 2006 Effects of mixing on post-discharge modeling of ElectricOIL experiments *Proc. SPIE.* **6101** 610125
[10] Vasiljeva A N *et al* 2004 *J. Phys. D: Appl. Phys.* **37** 2455
[11] Stafford D S and Kushner M J 2005 *J. Appl. Phys.* **98** 073303
[12] Cook T J and Miller T A 1974 *Chem. Phys. Lett.* **25** 396

[13] Atkinson R *et al* 2000 *J. Phys. Chem. Ref. Data* **29** 167

[14] Stafford D S and Kushner M J 2004 *J. Appl. Phys.* **96** 2451

[15] Lay B, Moss R S, Rauf S and Kushner M J 2003 *Plasma Sources Sci. Technol.* **12** 8

[16] Kushner M J 2004 *J. Appl. Phys.* **95** 846

[17] Hon J *et al* 1994 *A Heuristic Method for Evaluating COIL Performance* AIAA Paper 94-2422

[18] Rapp D and Briglia D D 1965 *J. Chem. Phys.* **43** 1480

[19] Josic L, Wroblewski T, Petrovic Z Lj, Mechlinska-Drewko J and Karwasz G P 2001 *Chem. Phys. Lett.* **350** 318

[20] Lindsay B G, Mangan M A, Straub H C and Stebbings R F 2000 *J. Chem. Phys.* **112** 9404

[21] Vejby-Christensen L, Kella D, Pedersen H B and Andersen L H 1998 *Phys. Rev.* A **57** 3627

[22] Shimamori H and Hotta H 1988 *J. Chem. Phys.* **89** 2938

[23] Ikezoe Y, Matsuoka S, Takebe M and Viggiano A 1987 *Gas Phase Ion-Molecule Reaction Rate Constants Through 1986* (Ion Reaction Research Group of the Mass Spectroscopy Society of Japan, Tokyo, Japan)

[24] Atkinson R *et al* 2004 *Atmos. Chem. Phys.* **4** 1461

[25] Boodaghians R B, Borrell P M and Borrell P 1983 *Chem. Phys. Lett.* **97** 193

[26] Blais N C 1985 *J. Phys. Chem.* **89** 4156

[27] Doroshenko V M, Kudryavtsev V M and Smetanin V V 1992 *High Energy Chem.* **26** 227

[28] Gauthier M J E and Snelling D R 1975 *J. Photochem.* **4** 27

[29] Valli G S, Orru R, Clementi E, Lagana A and Crocchianti S 1995 *J. Chem. Phys.* **102** 2825

[30] Phillips L F and Schiff H I 1965 *J. Chem. Phys.* **42** 3171

[31] Campbell I M and Gray C N 1973 *Chem. Phys. Lett.* **18** 607

[32] Holscher D and Zellner R 2002 *Phys. Chem. Chem. Phys.* **4** 1839

[33] Husain D, Slater N K H and Weisenfeld J R 1977 *Chem. Phys. Lett.* **51** 201

[34] Carroll D L *et al* 2005 *IEEE J. Quantum Electron.* **41** 213

[35] Zagidullin M V, Nikolaev V D, Svistun M I, Khvatov N I and Hager G D 2005 *Appl. Phys. A: Mater. Process.* **81** 311

[36] Muruganandam T M *et al* 2002 *AIAA J.* **40** 1388

JOURNAL OF APPLIED PHYSICS **101**, 123306 (2007)

$O_2(^1\Delta)$ production in high pressure flowing He/O_2 plasmas: Scaling and quenching

Natalia Y. Babaeva[a]
Department of Electrical and Computer Engineering, Iowa State University, Ames, Iowa 50011

Ramesh Arakoni[b]
Department of Aerospace Engineering, University of Illinois, Urbana, Illinois 61801

Mark J. Kushner[c]
Department of Electrical and Computer Engineering, Iowa State University, Ames, Iowa 50011

(Received 24 February 2007; accepted 17 April 2007; published online 22 June 2007)

Chemical oxygen-iodine lasers (COILs) oscillate on the $^2P_{1/2} \rightarrow ^2P_{3/2}$ transition of atomic iodine at 1.315 μm by a series of excitation transfers from $O_2(^1\Delta)$. In electrically excited COILs (eCOILs), the $O_2(^1\Delta)$ is produced in a flowing plasma, typically He/O_2, at a few to tens of Torr. Many system issues motivate operating eCOILs at higher pressures to obtain larger absolute densities of $O_2(^1\Delta)$ for a given yield and to provide higher back pressure for expansion. In this paper, we discuss results from a computational investigation of $O_2(^1\Delta)$ production in flowing plasmas sustained at moderate pressures ($\leq$50 Torr). Power deposition and flow rates were scaled such that in the absence of second order effects, yield should be constant and absolute $O_2(^1\Delta)$ production should scale linearly with pressure. We found in many cases that absolute $O_2(^1\Delta)$ production scaled sublinearly with pressure. Ozone is found to be one of the major quenchers of $O_2(^1\Delta)$ and its production increases with pressure. Gas heating also increases with increasing pressure due to exothermic three-body reactions. The gas heating reduces O_3 production, increases O_3 destruction and, for certain conditions, restores yields. With increasing pressure and increasing absolute densities of atomic oxygen and pooling reactions of $O_2(^1\Delta)$, quenching by these species also becomes important, though the influence of O-atom quenching can be controlled by managing the density of O atoms with additives. The yield of $O_2(^1\Delta)$ is also determined by discharge stability which becomes problematic at higher pressure. © *2007 American Institute of Physics*. [DOI: 10.1063/1.2743878]

I. INTRODUCTION

Chemical oxygen-iodine lasers are being investigated because of their ability to be delivered through optical fibers (1.315 μm), their highly scalable continuous wave power, and favorable material interaction properties.[1–6] Operation of the chemical oxygen-iodine laser (COIL) is based on an electronic transition between the spin-orbit levels of the ground state configuration of the iodine atom, $I(^2P_{1/2}) \rightarrow I(^2P_{3/2})$. The upper level is populated by near resonant energy transfer (quantum defect ~219 cm^{-1}) from $O_2(^1\Delta)$ to ground state $I(^2P_{3/2})$. The COIL generates ground state I atoms by dissociative excitation transfer from $O_2(^1\Delta)$ to I_2. Typically, $O_2(^1\Delta)$ is produced in an external chemical reactor by a gas-liquid reaction between gaseous chlorine and a basic hydrogen peroxide solution[7] producing yields approaching 100% of the oxygen emerging in the $O_2(^1\Delta)$ state. The long lifetime of $O_2(^1\Delta)$ (spontaneous lifetime of about 60 min) and robustness against quenching enables transport over long distances to the laser cavity.

In electrically excited COILs (eCOILs), the $O_2(^1\Delta)$ is produced in a flowing plasma, typically He/O_2, at a few to tens of Torr. Helium is often used as a buffer gas to lower the discharge gas temperature and to provide a more optimum electron temperature for excitation of $O_2(^1\Delta)$. Unlike the conventional COIL, the electric discharge variant also produces atomic oxygen by electron-impact dissociation of molecular oxygen. Although the atomic oxygen is a quencher of the upper laser level, it can also aid in the dissociation of I_2. Recent and ongoing investigations have shown that substantial yields of $O_2(^1\Delta)$ can be generated by an appropriately tailored electric discharge[8–17] in mixtures of O_2 with rare gas diluents. Scaling studies of non-self-sustained discharges where ionization is supported by an external source suggest that $O_2(^1\Delta)$ yields approaching 25%–30% might be possible. This is accomplished by tailoring the electron temperature to more closely match the energy range where the excitation cross sections for $O_2(^1\Delta)$ are largest.[12–14]

The three main components of COIL devices are the $O_2(^1\Delta)$ generator, a supersonic nozzle, and the laser cavity. The primary purpose of the supersonic nozzle is to lower the temperature in the laser cavity, thereby reducing the likelihood of the energy transfer process from $O_2(^1\Delta)$ to $I(^2P_{1/2})$ proceeding in the reverse direction. Recently, positive gain and laser oscillation in atomic iodine in a supersonic flow optical cavity have been reported resulting from electric discharge produced $O_2(^1\Delta)$.[18–21] An overview of $O_2(^1\Delta)$ generation in plasmas is given in Ref. 22.

---

[a] Electronic mail: natalie5@iastate.edu

[b] Electronic mail: arakoni@uiuc.edu

[c] Author to whom correspondence should be addressed; electronic mail: mjk@iastate.edu

Many system issues motivate operating eCOILs at higher pressures to obtain larger densities of $O_2(^1\Delta)$ for a given yield and to provide higher back pressure for expansion. If higher order effects are not important, and parameters such as energy deposition per molecule are maintained constant, it is expected that absolute $O_2(^1\Delta)$ production [that is, the total number of $O_2(^1\Delta)$ molecules produced] should scale linearly with pressure, thereby providing additional motivation for higher pressure operation.

In previous work, the scaling of production of $O_2(^1\Delta)$ was computationally investigated using global-kinetics, one-dimensional, and two-dimensional (2D) models.[13,14] It was found that the yield of $O_2(^1\Delta)$ generally scaled linearly with energy deposition at low pressures (<10 Torr) until the ground state O_2 is depleted. In this work, we report on results from a computational investigation of radio frequency (rf) excited flowing He/O_2 plasmas using plug-flow and two-dimensional (2D) models. The emphasis is on developing scaling laws for $O_2(^1\Delta)$ production in eCOIL systems when operating at higher pressures. We found that although yields may decrease with increasing pressure, absolute densities of $O_2(^1\Delta)$ typically do increase. Ground state and vibrationally excited ozone are major quenchers of $O_2(^1\Delta)$, and production of these species increase with pressure. With increasing absolute densities of atomic oxygen and pooling reactions of $O_2(^1\Delta)$, quenching by these species also become important, though the influence of O-atom quenching can be minimized by managing the O-atom density with additives. The yield of $O_2(^1\Delta)$ is also determined by discharge stability which becomes problematic at higher pressures.

The models and reaction mechanism are briefly described in Sec. II. The results from our investigations using the plug-flow model are discussed in Sec. III, followed by a discussion of results obtained from the 2D model in Sec. IV. Concluding remarks are in Sec. V.

II. DESCRIPTION OF THE MODELS

This investigation was performed with plug-flow and 2D models. The plug-flow model GLOBAL_KIN addresses gas-phase chemistry and transport, solution of Boltzmann's equation for the electron energy distribution, and equations for axial fluxes of mass, momentum, gas energy, and electron energy. The model is described in detail in Ref. 13 and so will be only briefly discussed here.

GLOBAL_KIN is a volume averaged, global-kinetics model for plasma chemistry. When operated in a plug-flow mode, axial transport is also approximated. GLOBAL_KIN contains a plasma chemistry module, a surface kinetics module, and an electron energy transport module. In the plasma chemistry module, the time rate of change of species and temperatures (electron and gas) are obtained integrating their respective conservation equations. Assuming a linear axial flow in a cylindrical tube, transport to radial surfaces is included by using a diffusion length. The reaction of fluxes on surfaces is addressed by the surface kinetics module which utilizes a surface site-balance model. Electron-impact rate coefficients are provided by the electron energy transport module where the electron energy distributions are obtained by solving Boltzmann's equation. By simultaneously calculating the axial speed of the flow based on constant pressure, change in enthalpy, species densities, and gas temperature, the integration in time is mapped to axial position. Although computationally fast, the weakness of this method is neglecting axial transport by diffusion.

The 2D model used in this study, nonPDPSIM, is a multifluid hydrodynamics simulation, described in detail in Ref. 14, in which transport equations for all charged and neutral species and Poisson's equation are integrated as a function of time. Poisson's equation [Eq. (1)], transport equations for conservation of the charged species [Eq. (2)], and the surface charge balance equation [Eq. (3)] are simultaneously integrated using a Newton iteration technique,

$$-\nabla\cdot(\varepsilon_0\varepsilon_r\nabla\Phi)=\sum_j N_j q_j+\rho_s, \qquad (1)$$

$$\frac{\partial N_j}{\partial t}=-\nabla\cdot\mathbf{\Gamma}_j+S_j, \qquad (2)$$

$$\frac{\partial\rho_s}{\partial t}=\sum_j q_j(-\nabla\mathbf{\Gamma}_j+S_j)-\nabla\cdot(\sigma[-\nabla\Phi)], \qquad (3)$$

where ε_0, ε_r, Φ, ρ_s, N_j, $\mathbf{\Gamma}_j$, σ, S_j, and q_j are the permittivity of free space, dielectric constant, electric potential, surface charge density, species density and flux, conductivity of solid materials, sources, and charge, respectively. The subscripts j denote gas-phase species. Updates of the charged particle densities and electric potential are followed by an implicit update of the electron temperature by solving the electron energy equation for average energy, ε,

$$\frac{\partial(n_e\varepsilon)}{\partial t}=q\mathbf{\Gamma}_e\cdot\mathbf{E}-n_e\sum_j\Delta\varepsilon_j N_j\kappa_j-\nabla\cdot\left(\frac{5}{2}\varepsilon\mathbf{\Gamma}_e-\lambda_e\nabla T_e\right), \qquad (4)$$

where $\frac{3}{2}kT_e=\varepsilon$. The terms in Eq. (4) are for the contribution from Joule heating, elastic and inelastic impact processes with heavy neutrals and ions with energy loss κ_j, and electron heat flux consisting of terms for electron energy flux (Γ_e) and a conduction (λ_e is the electron thermal conductivity). The electron transport coefficients and rate coefficients for bulk electrons as a function of T_e are obtained by solving the zero-dimensional Boltzmann's equation for the electron energy distribution to capture the non-Maxwellian nature of the electron swarm.

The fluid averaged advective velocity $\mathbf{v}$ is obtained by solving a modified form of the compressible Navier-Stokes equations in which momentum transfer from ion and electron collisions; and acceleration by the electric field are included in the momentum equation, and Joule heating is included in the energy equations.

$$\frac{\partial\rho}{\partial t}=-\nabla\cdot(\rho\mathbf{v})+P, \qquad (5)$$

$$\frac{\partial(\rho\mathbf{v})}{\partial t}=-\nabla p-\nabla\cdot(\rho\mathbf{v}\mathbf{v})-\nabla\cdot\bar{\bar{\tau}}+\sum_j(q_jN_j-M_j\mu_jS_j)\mathbf{E}, \qquad (6)$$

$$\frac{\partial(\rho c_p T)}{\partial t} = -\nabla(-\kappa\nabla T + \rho \mathbf{v} c_p T) + \sum_j \mathbf{j}_j \cdot \mathbf{E} - \sum_i R_i \Delta H_i + p\nabla\cdot\mathbf{v}, \tag{7}$$

where P represents the inlet and outlet flows (the inlet flow is specified while the output flow is adjusted to maintain a constant mass flux), ρ is the total mass density, p is the thermodynamic pressure, $\bar{\bar{\tau}}$ is the viscosity tensor, c_p is the heat capacity, κ is the species averaged thermal conductivity, μ is the mobility, and M the molecular weight. ΔH_i is the change enthalpy due to reaction i having total rate R_i. The reactions include Frank-Condon heating from electron-impact dissociation of molecules as well as conventional chemical reactions. The sums (other than for reactions) are over all charged and neutral species. The contributions to momentum from charged particles include those of electrons. The contributions to the energy equation from Joule heating include contributions from ions. The heat transfer from electrons is included as a collisional change in enthalpy. The relationship between pressure, density, and temperature is given by the ideal-gas law. The numerical grid in nonPDPSIM uses an unstructured, cylindrically symmetric mesh with triangular elements.

The reaction mechanism for He/O_2 plasmas used here is essentially the same as that described in Refs. 13 and 14, and involves reactions in the gas-phase discharge and afterglow as well as recombination and quenching reactions on the discharge tube walls. The species in the model are ground-state neutrals O_2, O, O_3, and He; $O_2(v)$ (the first four vibrational levels of O_2), electronic states $O_2(^1\Delta)$, $O_2(^1\Sigma)$, $O(^1D)$, $O(^1S)$, and $He(^2S)$; and the ions O_2^+, O^+, O_2^-, O^-, O_3^-, and He^+.

The precursors to the eCOIL laser, $O_2(^1\Delta)$ (0.98 eV) and $O_2(^1\Sigma)$ (1.63 eV), are dominantly produced in the discharge by direct electron impact with the ground state,

$$e + O_2 \rightarrow O_2(^1\Delta) + e, \tag{8}$$

$$e + O_2 \rightarrow O_2(^1\Sigma) + e, \tag{9}$$

and in reactions of electronic excitation transfer from metastable $O(^1D)$ atoms,

$$O(^1D) + O_2 \rightarrow O_2(^1\Sigma) + O. \tag{10}$$

Production of $O_2(^1\Sigma)$ generally also results in generation of $O_2(^1\Delta)$ through rapid collisional quenching reactions with atomic oxygen and ozone. The atomic oxygen is dominantly produced by electron-impact dissociation of O_2,

$$e + O_2 \rightarrow O + O + e, \tag{11}$$

$$e + O_2 \rightarrow O(^1D) + O + e. \tag{12}$$

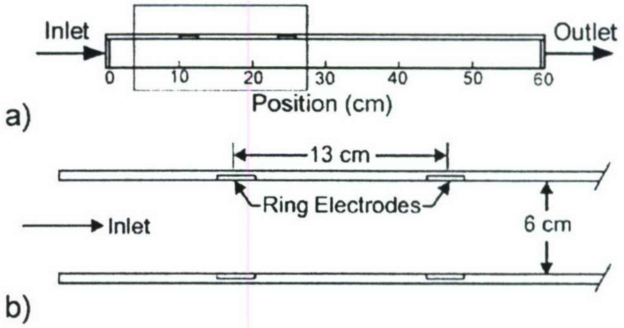

FIG. 1. Schematic of the discharge tube. (a) Computational domain. The flow enters uniformly from the left where pressure, speed, and temperature are specified. The walls are held at constant temperature and mass flux is conserved at the outlet. (b) Close-up showing ring electrodes.

The $O_2(^1\Delta)$ persists far into the afterglow due to its long radiative lifetime, where the most significant quenching reactions are collisions with O atoms and O_3, and energy pooling with $O_2(^1\Delta)$. The rate of quenching of $O_2(^1\Delta)$ by collisions with the walls is uncertain due to the variability of the quenching probability with temperature and conditions of the wall. Based on estimates for similar conditions, we have assigned a wall quenching coefficient of 10^{-5}, which results in insignificant wall quenching for typical eCOIL conditions.

The effective yield of $O_2(^1\Delta)$ is defined as the ratio of the combined $O_2(^1\Delta)$ and $O_2(^1\Sigma)$ densities to the sum of the densities of all oxygen-containing species on a molecular O_2 basis,

$$Y = \frac{[O_2(^1\Delta)] + [O_2(^1\Sigma)]}{([O_2]+[O_2(v)]+[O_2(^1\Delta)]+[O_2(^1\Sigma)] + 0.5[O] + 1.5[O_3])}. \tag{13}$$

This choice of yield was made with the prior knowledge that the majority of $O_2(^1\Sigma)$ is quenched directly to $O_2(^1\Delta)$. Typically in the afterglow region, the density of $O_2(^1\Sigma)$ is negligibly small. As such, Eq. (13) is most relevant for best case energy scaling.

In our model, the first four vibrational states of O_2 are lumped into a single effective vibrational state $O_2(v)$ having excitation energy of 0.19 eV. In addition to superelastic electron collisions with $O_2(v)$, all electron impact processes included for ground state O_2 were also included for $O_2(v)$ with the threshold energy shifted by 0.19 eV. In a similar manner, in addition to collisional quenching of $O_2(v)$ which contributes to gas heating, all heavy particle reactions included for ground state O_2 were also included for $O_2(v)$. Although we acknowledge that rate coefficients for these processes may depend on the vibrational state, there is limited kinetic available to account for those effects and so they have not been included here. Since the density of $O_2(v)$ is typically only $10^{-2}-10^{-3}$ that of ground state O_2 we expect that the error resulting from those omissions is small.

A schematic of the idealized eCOIL device addressed in this study is shown in Fig. 1. A He/O_2=70/30 mixture is flowed through a cylindrically symmetric quartz tube 60 cm in length and 6 cm in diameter. A rf electric discharge is operated between two ring electrodes 2 cm wide with centers separated by 13 cm. The electrodes are powered up to a few kW at 25 MHz. The flow rate for each pressure corresponds to an average axial inlet speed of 985 cm/s. Thus the species residence time is approximately the same for each pressure provided we neglect gas heating. Our investigations were limited to the region of the reactor prior to supersonic expansion and injection of I_2. The wall temperature was held fixed at 300 K assuming active water-jacket cooling.

III. SCALING OF $O_2(^1\Delta)$ PRODUCTION WITH PRESSURE: PLUG-FLOW MODELING

The basic scaling laws of $O_2(^1\Delta)$ generation as a function of pressure in flowing He/O_2 plasmas were first investigated using the plug-flow model GLOBAL_KIN for the geometry shown in Fig. 1. To eliminate as many systematic trends as possible while changing pressure, two parameters were kept constant: energy deposition per inlet oxygen molecule α (eV/molecule) and flow residence time in the discharge tube, τ. To keep τ constant, the flow rate is increased in proportion to pressure. To keep α constant, power is increased in proportion to pressure provided τ is constant. Computationally, this is accomplished by computing the power deposition as a cycle averaged product of voltage times current and comparing that power to the value required to keep α constant. Every few rf cycles the voltage is adjusted (increased or decreased by a maximum of a few percent) in the direction to deliver the desired power. This process is continued until a quasi-steady-state is reached.

Keeping these parameters constant, if there are no second order effects, yield should remain constant and absolute $O_2(^1\Delta)$ production should scale linearly with pressure. We also expect that the electron temperature T_e and gas temperature T_g should weakly depend upon pressure. The former insensitivity results from electron losses being dominated by volumetric processes (i.e., attachment and dissociative recombination) and so the rate of loss by diffusion does not significantly affect the electron accounting. The latter insensitivity results from thermal conduction, which is the dominant temperature regulating loss process, not being a sensitive function of pressure in the range we investigated.

At least two second order effects will be seen to be important: three-body reactions and discharge stability. The three-body reactions which produce quenchers of $O_2(^1\Delta)$, such as O_3, are detrimental due to the resulting reduction in $O_2(^1\Delta)$ density. Three-body reactions of the sort $A+B+M \rightarrow AB+M$ are typically exothermic and can be a significant heating source as these reactions begin to dominate at higher pressures. The resulting increase in gas temperature usually has a negative effect. The onset of discharge instabilities at higher pressures is potentially harmful due to the nonuniform power deposition that results.

Plasma parameters obtained with the plug-flow model for pressures from 3 to 50 Torr for He/O_2=70/30 and α=0.3 eV/molecule (40–670 W) are shown in Figs. 2–5. The power profile is specified based on the results from the 2D model. When keeping α constant, the electron density weakly depends upon pressure, increasing in peak value from 1×10^{10} to 1.9×10^{10} cm^{-3} from 3 to 50 Torr. There is a small decrease in T_e (from 2.7 to 2.4 eV) when increasing pressure due to a reduction in diffusion losses of electrons. The decrease in T_e then reduces the power dissipation per electron which necessitates an increase in electron density.

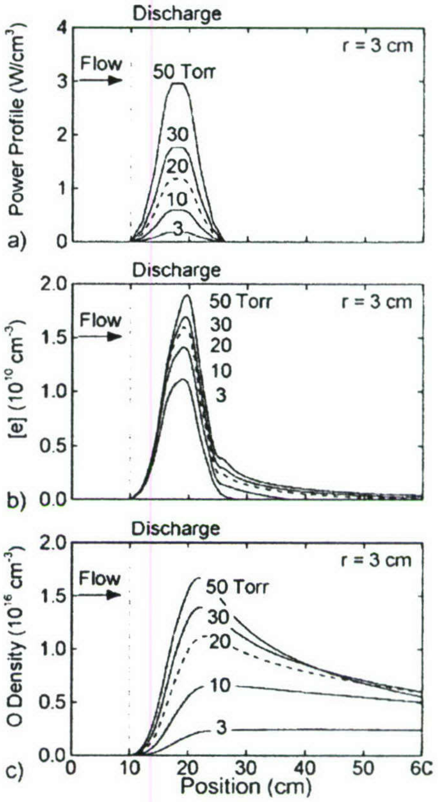

FIG. 2. Plasma and flow parameters for 3–50 Torr (α=0.3 eV/molecule, He/O_2=70/30, r=3 cm). (a) Power, (b) electron density, and (c) atomic oxygen density. In the discharge region up to 10% of the molecular oxygen is dissociated.

Electron-impact dissociative excitation of O_2 results in approximately 10% dissociation, producing peak O-atom densities of 2.2×10^{15} to 1.6×10^{16} cm^{-3} from 3 to 50 Torr. This increase in O-atom density is sublinear with respect to pressure due to the increased efficiency of consumption of O atoms by the three-body collisions that form ozone,

$$O + O_2 + M \rightarrow O_3 + M. \quad (14)$$

This reaction has a rate coefficient of $6\times10^{-34}(T_g/300)^{-2.8}$ cm^6 s^{-1} which decreases the formation of ozone with increasing gas temperature. The main reaction for ozone destruction,

$$O + O_3 \rightarrow O_2 + O_2, \quad (15)$$

has a rate coefficient, $8\times10^{-12}\exp(-2060/T_g)$ cm^3 s^{-1}. The increase in exothermic three-body reactions, such as Eq. (14), with increasing pressure results in significant gas heating. In spite of α being a constant, the result is that the peak gas temperature increases from 330 to 520 K when increasing pressure from 3 to 50 Torr. Note that at 3 Torr, the peak in T_g occurs in the discharge region where plasma heating (mostly ion Joule heating) is the dominant heating mechanism. At 50 Torr, T_g peaks downstream, a consequence of heating from exothermic three-body reactions which occur dominantly outside the plasma zone.

The combination of increasing production of O_3 due to three-body processes and increasing destruction of O_3 due to an increase in gas temperature results in the axial dependence of O_3, as shown in Fig. 3(a). At low pressure, the peak in O_3 density occurs downstream. The low rate of three-body

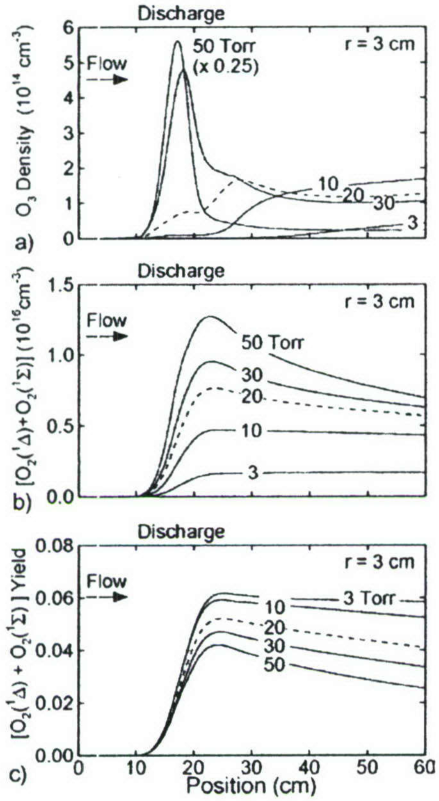

FIG. 3. Density of oxygen species for 3–50 Torr (α=0.3 eV/molecule, He/O_2=70/30, r=3 cm). (a) O_3, (b) $O_2(^1\Delta)+O_2(^1\Sigma)$ and (c) combined $O_2(^1\Delta)+O_2(^1\Sigma)$ yield. The peak of ozone production is in the upstream side of the discharge region where the gas temperature is lower.

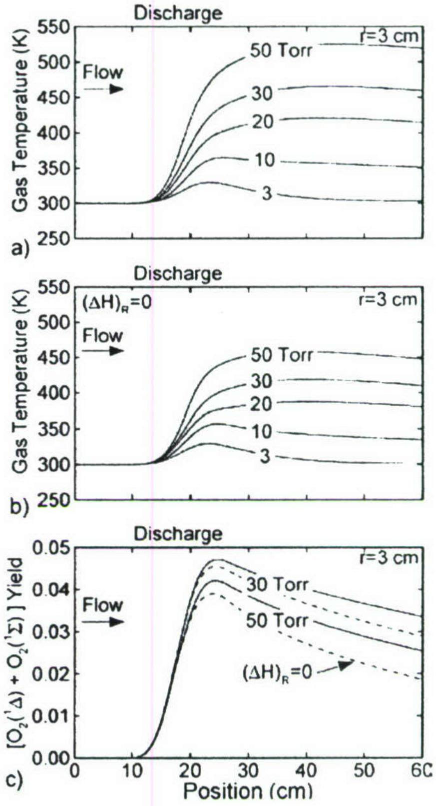

FIG. 5. Gas temperature and yield for 3–50 Torr (α=0.3 eV/molecule, He/O_2=70/30, r=3 cm). (a) Enthalpy from three-body recombination heating is included, (b) recombination heating is excluded, and (c) combined $O_2(^1\Delta)+O_2(^1\Sigma)$ density for 30 and 50 Torr with and without recombination heating. For these conditions there is a decrease in yield when the gas becomes colder due to the increased production of O_3.

reactions and low gas temperature (low rates of O_3 destruction) result in most of the O_3 being produced only after a finite flow time and this density accumulates in the discharge. (The average residence time in the flow tube is 60 ms.) At higher pressures, the rate of three-body reactions is proportionally higher resulting in large rates of formation of O_3 in the discharge prior to there being significant gas heating. For example, the peak O_3 density is 2.2 $\times 10^{15}$ cm^{-3} at 50 Torr. The accompanying increase in gas temperature downstream results in increased rates of destruction of O_3 by collisions with O atoms which ultimately reduces its density. The end result is that the downstream density of O_3 is maximum at $(1-2)\times 10^{14}$ cm^{-3} at pressures of 10–20 Torr.

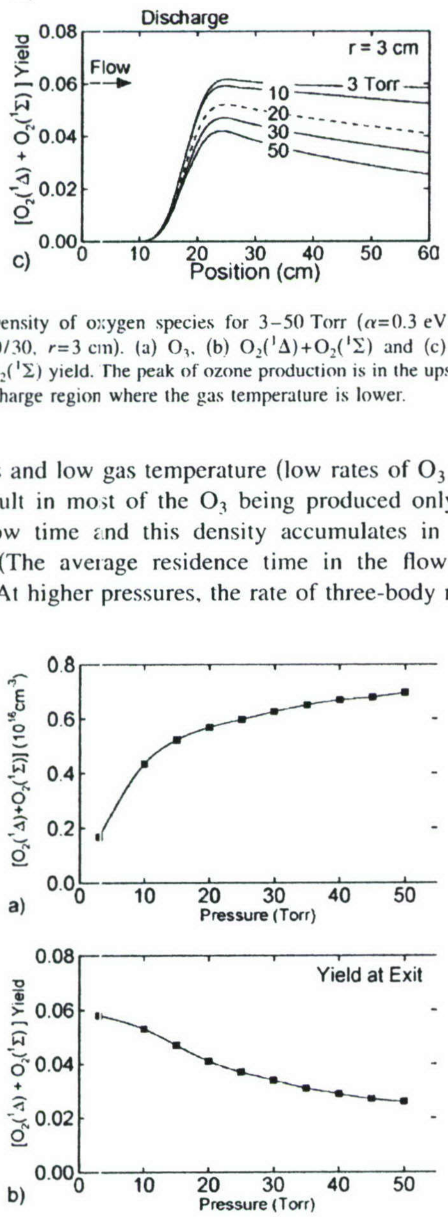

FIG. 4. Density of oxygen species (α=0.3 eV/molecule, He/O_2=70/30, r=3 cm) as a function of pressure at the exit of the tube. (a) $O_2(^1\Delta)+O_2(^1\Sigma)$ and (b) combined $O_2(^1\Delta)+O_2(^1\Sigma)$ yield.

The O_3 density is an important consideration due to its being an efficient quencher of $O_2(^1\Delta)$,

$$O_2(^1\Delta) + O_3 \rightarrow O_2 + O_2 + O. \quad (16)$$

With a rate coefficient of $5.2\times 10^{-11}\exp(-2840/T_g)$ cm^3 s^{-1}, the rate of quenching increases with the increase in gas temperature occurring at higher pressures. [Note that the rate coefficient for quenching of $O_2(^1\Delta)$ by vibrationally excited O_3 is more than an order of magnitude larger than for the ground state.[23]] The increase in O_3 and the increase in gas temperature both increase quenching rates. This results in the density of O_2^* [denoting the sum of the densities of $O_2(^1\Delta)$ and $O_2(^1\Sigma)$] increasing sublinearly with increasing pressure and in the decrease of total yield as a function of pressure, as shown in Fig. 4. At low pressure ($\leq$10 Torr) with constant α, the yield is nearly constant and so the absolute production of O_2^* scales with pressure. At higher pressures, the production and yield of O_2^* peak in the plasma zone. The density of O_2^* decreases thereafter, a consequence of downstream quenching at the higher gas temperatures in the presence of O_3. The result is sublinear scaling with pressure.

At higher pressures contributions to gas heating are dominated by three-body recombination heating and Frank-Condon heating due to dissociative electronic excitation. To distinguish between these two contributions, we artificially excluded contributions to gas heating from changes in enthalpy ΔH from three-body recombination reactions. The resulting gas temperatures, shown in Fig. 5(b), are lower by 50–70 K at higher pressures (30 and 50 Torr). For lower pressures (3–10 Torr) the differences in gas temperature are small and heating is dominated by Frank-Condon and Joule heating in the plasma zone. Decreasing the temperature in this manner increases the O_3 density which translates directly into higher quenching and lower exit densities of O_2^*. This results in lower O_2^* yields, as shown in Fig. 5(c).

The hierarchy of the main quenchers of $O_2(^1\Delta)$ for 10, 30, and 50 Torr is shown in Fig. 6 for the base case conditions. Quenching times are determined by $1/(k[M])$, where $[M]$ is density of the quencher and k is the rate constant. More rapid and important quenching reactions are denoted by shorter quenching times. By the exit of the discharge tube, O_3 is the primary quencher for pressures >10 Torr. For pressures higher than 30 Torr, quenching times by O_3 become comparable to the gas residence time which is about 60 ms. Atomic oxygen is the second most important quencher. Quenching times for O_2 and $O_2(^1\Delta)$ are of the order of a few seconds and not important. Note that the O_3 density, especially at high pressures, is two orders of magnitude smaller than atomic oxygen but it is the dominant quencher.

Another second order effect that complicates pressure scaling when changing the tube size is heat transfer to the walls. For example, plasma and flow parameters for tubes having radii of 3 and 1 cm while keeping other conditions equal (α=0.9 eV/molecule and 60 ms residence time) are shown in Figs. 7 and 8. In the larger tube and with the larger diffusion length for heat transfer to the walls, gas heating at 50 Torr produces temperatures of nearly 800 K. As a consequence, O_3 produced in large quantities upstream in the discharge is rapidly depleted in the afterglow. The prior dominance of O_3 as a quencher is reduced to be comparable to that of atomic oxygen. Yield for O_2^* at the end of the tube for 50 Torr is 10%, down from 14% at 3 Torr.

Reducing the tube radius results in more efficient gas cooling due to the shorter radial diffusion length. For example, the gas temperature at the tube exit at 50 Torr drops from 750 K for a radius of 3 cm to 430 K for a radius of 1 cm. As a result, there is increasing production of O_3 downstream as the temperature decreases, ozone again becomes the main quencher of $O_2(^1\Delta)$, and yield decreases to 7%.

Ozone and gas temperature management are clearly important considerations in pressure scaling. For example, pressure scaling for a tube with a radius of 1 cm was repeated keeping α=0.9 eV/molecule while increasing the flow rate to reduce the residence time by a factor of 9 to approximately 7 ms. The results are shown in Fig. 9. Since α is constant the maximum gas temperature is nearly the same as the prior case. However, the shorter residence time downstream reduces the amount of conductive cooling and so the exit gas temperature increases to 610 K for 50 Torr. The higher gas temperature increases the rate of O_3 destruction and decreases the rate of its formation, thereby reducing O_3 densities. The lower O_3 densities and shorter residence times reduce the likelihood that quenching of $O_2(^1\Delta)$ will occur. As a result, yield is restored to 13.3% at 50 Torr.

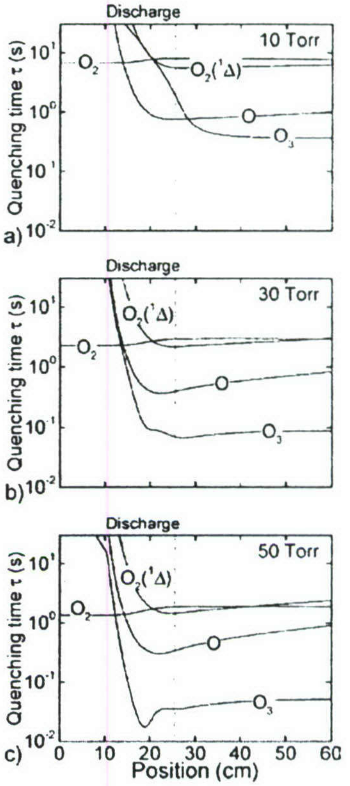

FIG. 6. Quenching times for $O_2(^1\Delta)$ for (a) 10, (b) 30, and (c) 50 Torr (α =0.3 eV/molecule, He/O_2=70/30, r=3 cm). Ozone is the main quencher in the postdischarge downstream region. For pressures higher than 30 Torr the ozone quenching time becomes comparable with the gas residence time.

Another factor that is potentially important to pressure scaling is the possibility of three-body quenching of $O_2(^1\Delta)$ by O atoms. Previous studies of excited state kinetics in discharges sustained in oxygen[11,15,16] indicated lower than expected yields of $O_2(^1\Delta)$ at higher pressures where the O-atom density is high. The authors[11] proposed that oxygen atoms in a three-body collision were responsible for the quenching,

$$O_2(^1\Delta) + O + O_2 \rightarrow O_2 + O_2 + O. \tag{17}$$

Good agreement was obtained between modeling and experiments with a rate coefficient of 1×10^{-32} cm^6 s^{-1}. This process is in addition to the two-body quenching of $O_2(^1\Delta)$ by O atoms,

$$O_2(^1\Delta) + O \rightarrow O_2 + O, \tag{18}$$

having a rate coefficient of 1.1×10^{-10} cm^3 s^{-1}.

The densities of O_2^* and yields for 10 and 50 Torr with and without three-body O-atom quenching of $O_2(^1\Delta)$ are

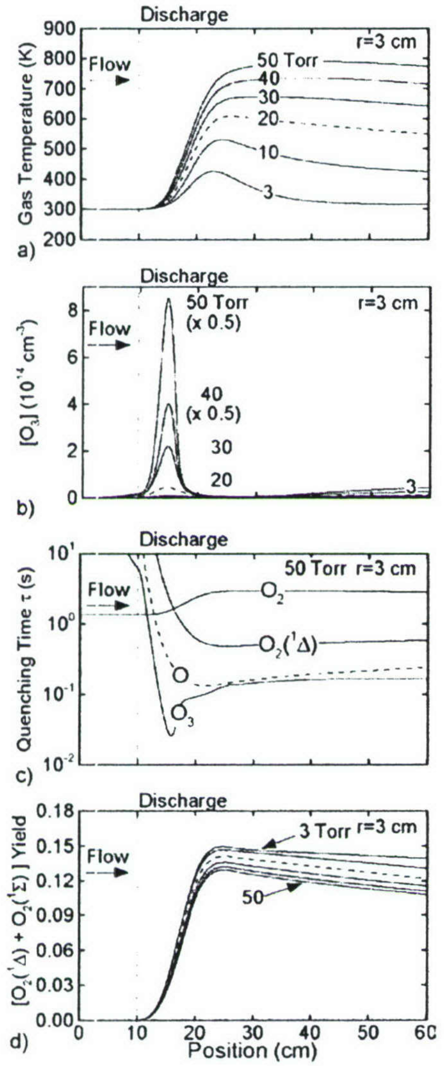

FIG. 7. Plasma and flow parameters for 3–50 Torr ($\alpha=0.9$ eV/molecule, He/O_2=70/30) for a radius of 3 cm and a residence time of 60 ms. (a) Gas temperature, (b) O_3 density, (c) quenching times at 50 Torr, and (d) combined $O_2(^1\Delta)+O_2(^1\Sigma)$ yield. A long residence time results in higher gas temperature and lower ozone density.

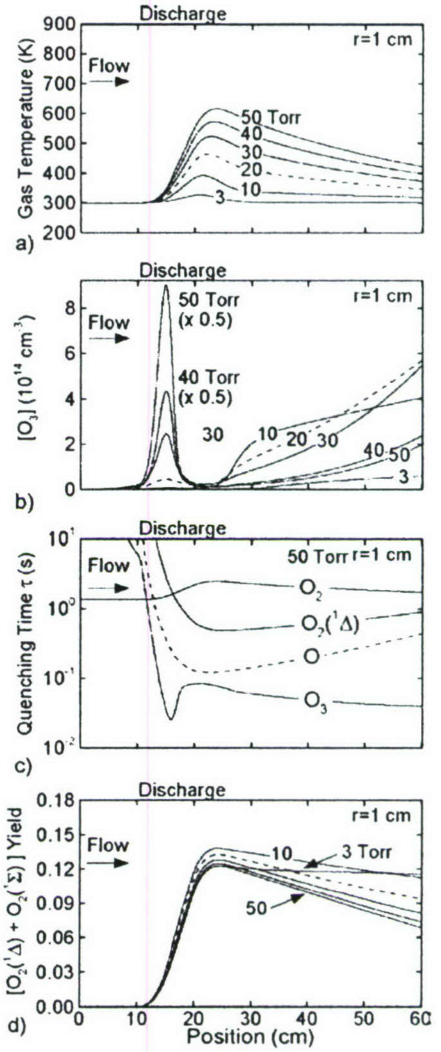

FIG. 8. Plasma and flow parameters for 3–50 Torr ($\alpha=0.9$ eV/molecule, He/O_2=70/30) for a radius of 1 cm and a residence time of 60 ms. (a) Gas temperature, (b) O_3 density, (c) quenching times at 50 Torr, and (d) combined $O_2(^1\Delta)+O_2(^1\Sigma)$ yield. The smaller tube radius provides for higher rates of gas cooling which restores the ozone density in the afterglow. As such the yield for 50 Torr decreases from 10.8% to 7% compared to a 3 cm tube.

shown in Fig. 10. Yields and O_2^* densities decrease by approximately a factor of 2 at 50 Torr when including three-body quenching. For pressures greater than 20 Torr, three-body quenching by O atoms is commensurate with that by O_3, as shown in Fig. 10(d). Resolution of the value and temperature dependence of three-body quenching of $O_2(^1\Delta)$ by O atoms is clearly important to the pressure scaling of eCOIL devices. Alternatively, gas mixtures can be selected in which O atoms created by the discharge are scavenged and so minimize the influence of O atoms on quenching of $O_2(^1\Delta)$. Oxygen atoms are also efficient quenchers of the $I(^2P_{1/2})$ upper laser level, and so minimizing the O-atom density also directly aids in maintaining the inversion.

Many methods have been proposed to scavenge O atoms and so improve laser performance, such as coating of the tube walls with a HgO.[15] A practical and recently implemented method is to use small amounts of NO or NO_2 either in the initial gas flow or as additives downstream.[20] NO and NO_2 both rapidly react with O atoms in a chain reaction that has the net effect of converting O atoms to O_2. These reactions are

$$NO + O + M \rightarrow NO_2 + M, \qquad (19)$$

$$NO_2 + O \rightarrow NO + O_2, \qquad (20)$$

with rate constants of $1\times10^{-31}(T_g/300)^{-1.6}$ cm^6 s^{-1} and $4.21\times10^{-12}\exp(-273/T_g)$ cm^3 s^{-1}, respectively. By controlling the O-atom density in this manner, quenching by O_3 is also regulated as O atoms are the precursor to O_3 formation. NO addition has the added benefit of removing O_3 by

$$NO + O_3 \rightarrow O_2 + NO_2, \qquad (21)$$

having a rate coefficient of $1.4\times10^{-12}\exp(-1310/T_g)$ cm^3 s^{-1}.

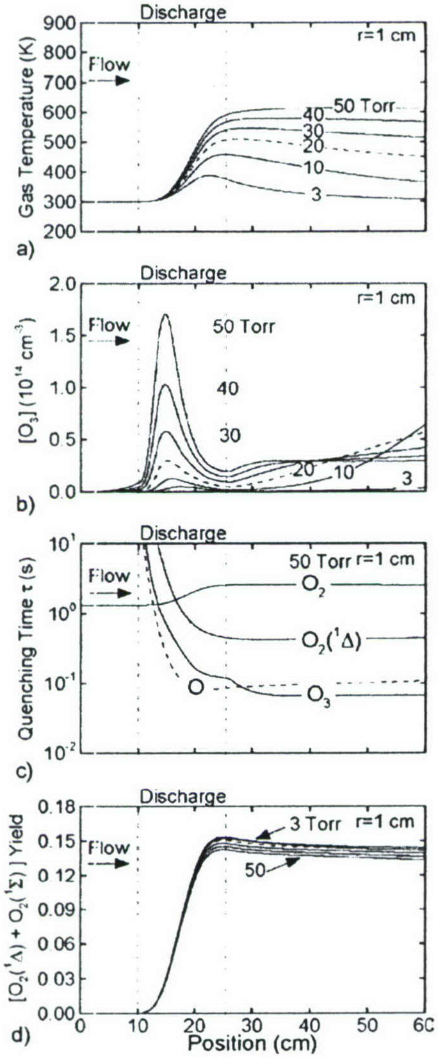

FIG. 9. Plasma and flow parameters for 3–50 Torr (α=0.9 eV/molecule, He/O_2=70/30) for a radius of 1 cm and a residence time of 7 ms. (a) Gas temperature. (b) O_3 density. (c) quenching times at 50 Torr, and (d) combined $O_2(^1\Delta)+O_2(^1\Sigma)$ yield. A smaller residence time results in lower gas temperature in the discharge region, but prevents rapid cooling in the afterglow. Yield is restored to 13.3%.

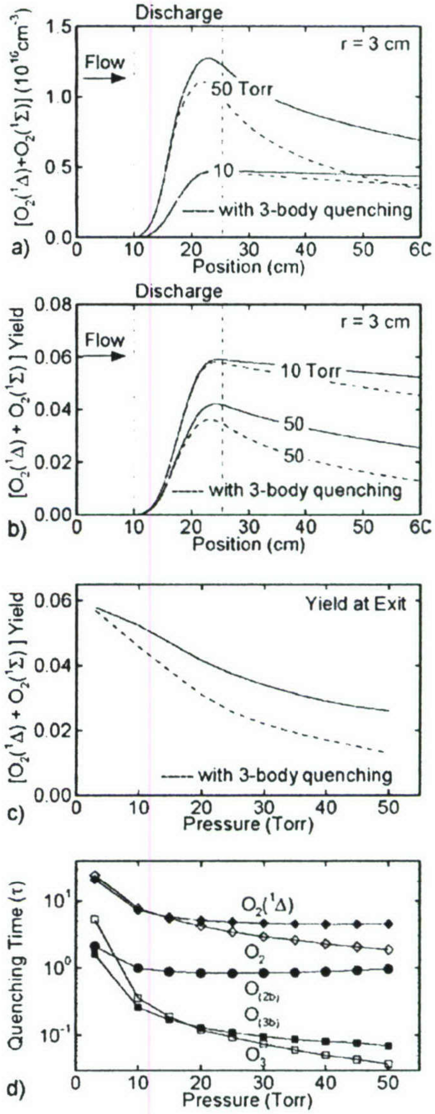

FIG. 10. Density of oxygen species (α=0.3 eV/molecule, He/O_2=70/30, r=3 cm) with and without three-body quenching with O atoms. (a) $O_2(^1\Delta)+O_2(^1\Sigma)$ for 10 and 50 Torr, (b) combined $O_2(^1\Delta)+O_2(^1\Sigma)$ yield for 10 and 50 Torr, (c) combined $O_2(^1\Delta)+O_2(^1\Sigma)$ yield as a function of pressure at the exit, and (d) quenching times. Accounting for three-body quenching results in substantial decrease in yield (dashed lines). Symbols $O_{(2b)}$ and $O_{(3b)}$ indicate atomic oxygen in two-body and three-body reactions.

The effect of NO addition in high pressure scaling when including three-body quenching by O atoms was investigated using the plug-flow model. Densities of oxygen species (O, O_3, and O_2^* and yield are shown in Fig. 11 as a function of pressure and inlet NO mole fraction. These quantities are at the exit of the flow tube. In the absence of NO, O and O_3 densities increase with pressure and saturate around 10–20 Torr. With these large densities of O and O_3 as quenchers, the density of O_2^* reaches a maximum between 10 and 20 Torr and slowly decreases at higher pressures. This quenching results in a monotonic decrease in yield.

With addition of up to 1% of NO, the exit densities of O and O_3 at pressures above 20–30 Torr are essentially eliminated. The reduction in these densities directly translates into less quenching and higher exit densities of $O_2(^1\Delta)$. With 1% NO, the absolute densities of $O_2(^1\Delta)$ increase with pressure and yields are largely restored. Although three-body quenching of $O_2(^1\Delta)$ is potentially an important process at high pressures, the consequences of this process can be minimized by managing the density of O atoms with small amounts of additives, such as NO or NO_2.

IV. CONSEQUENCES OF HYDRODYNAMICS ON PRESSURE SCALING

The results obtained using the plug-flow model provide insights into the kinetic processes that affect $O_2(^1\Delta)$ yields when increasing pressure. In this section additional considerations will be discussed with results from the 2D model that more realistically represent the electrical circuitry, electrode losses, uniformity, and flow considerations.

Another second order effect that may influence $O_2(^1\Delta)$ production is the discharge constriction commonly observed at higher pressures due to the smaller mean-free path of elec-

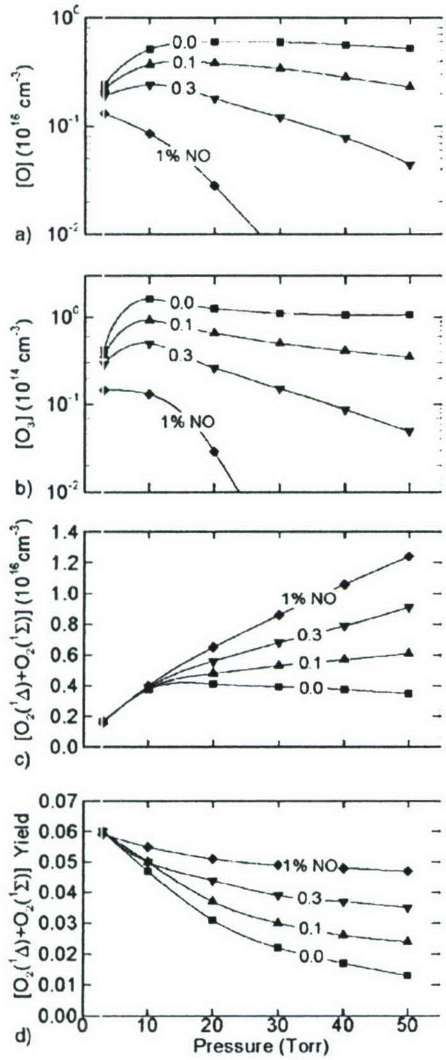

FIG. 11. Plasma properties at the exit of the flow tube ($\alpha = 0.3$ eV/molecule, He/O_2=70/30, $r=3$ cm) as a function of pressure and NO addition. Densities of (a) O, (b) O_3, and (c) $O_2(^1\Delta)+O_2(^1\Sigma)$, and (d) combined $O_2(^1\Delta)+O_2(^1\Sigma)$ yield. Three-body quenching by O atoms is included. Addition of small mole fractions of NO regulate the O-atom density and restores yield.

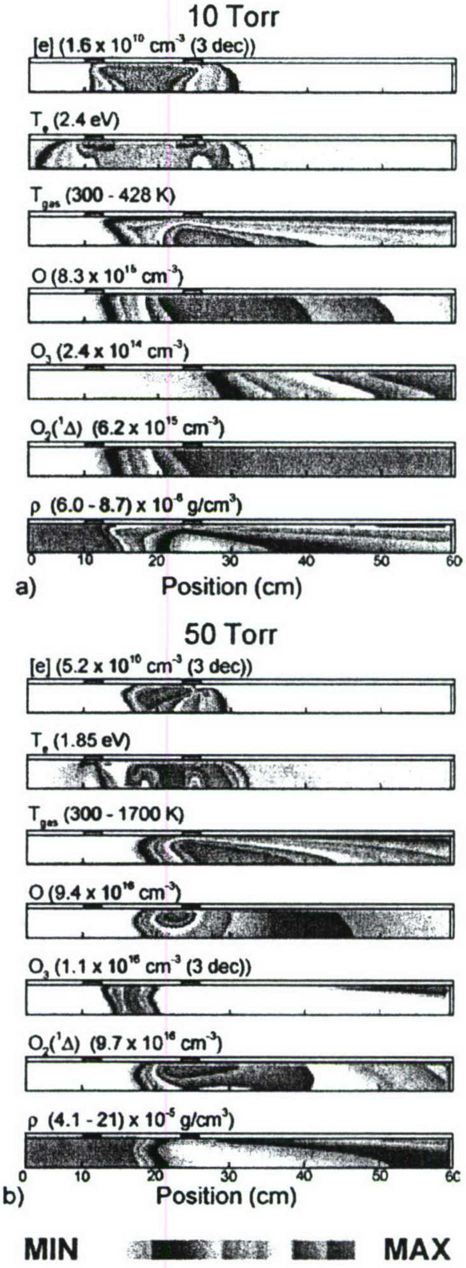

FIG. 12. (Color) Plasma parameters [electron density, electron temperature, gas temperature, and densities of O, O_3, and $O_2(^1\Delta)$, and total gas mass density] for (a) 10 and (b) 50 Torr (He/O_2=70/30, 25 MHz rf excitation, $\alpha=0.3$ eV/molecule). All values are averaged over one rf period. The flow is from the left. The scales are linear with zero minimum values with the exception of T_g unless the number of decades is indicated for log plots. The maximum value is indicated in each figure. Discharge constriction at the higher pressure occurs near the downstream electrode.

trons and gas heating. The shorter mean-free paths result in electron-impact excitation occurring dominantly in regions of high electric field (that is, electron transport is local as opposed to nonlocal). Gas heating and the resulting rarefaction produce nonuniformities in gas density which even with uniform electric fields may produce nonuniform values of E/N (electric field divided by gas number density).

For example, plasma properties and the spatial distribution of species densities are compared in Fig. 12 for $\alpha = 0.3$ eV/molecule for moderate (10 Torr, 133 W) and high (50 Torr, 670 W) pressures. These results are averages over the 25 MHz cycle in the quasi-steady-state. (When comparing these results to those from the plug-flow model, recall that the values obtained from the plug-flow model are volume averages. The peak values as a function of radius in the 2D model, in many cases occurring on the axis, will be larger than those from the plug-flow model.) At 10 Torr the electron density is smoothly distributed between the electrodes with a peak value of 1.6×10^{10} cm^{-3}. The cycle averaged electron temperature is 1.9 eV in the bulk plasma, peaking at 2.4 eV near the electrodes. The dissociation fraction of the inlet O_2 is 4.5%, producing a peak O-atom density of 8.3×10^{15} cm^{-3}. The O atoms are progressively converted to O_3 as they flow towards the exit, producing an exit density of O_3 of 2.4×10^{14} cm^{-3}. The increase in gas temperature is about 130 K which decreases downstream where the O_3 density is highest. Due to the low gas temperature, $O_2(^1\Delta)$ quenching (mostly by ozone) is negligible.

At 50 Torr, the discharge becomes inhomogeneous with the highest electron density of 5×10^{10} cm^{-3} near the downstream electrode. The peak electron temperature drops to 1.85 eV. Due to recombination and Frank-Condon heating, the peak gas temperature increases to 1700 K. The rarefaction of the gas near the downstream electrode allows for higher proportional power deposition there. Oxygen molecules are more highly dissociated (10% fractional dissociation) producing a peak O-atom density of 9.4×10^{16} cm^{-3}. Due to the high temperature near the downstream electrode, O_3 produced in the upstream portion of the discharge is largely destroyed prior to leaving the discharge zone. The O_3 density is gradually restored downstream near the tube walls where the gas is coolest. The $O_2(^1\Delta)$ density maximizes in the discharge region where the power deposition is concentrated near the downstream electrode.

The reduced electric field E/N (electric field/gas number density) is not uniformly distributed over the discharge. The maximum values of E/N occur in the sheath regions near the electrode. However, at the pressures of interest, the majority of power deposition occurs in the bulk plasma where the electron density is maximum. In these volumes, typical values of E/N (averaged over a rf cycle) are 10–25 Td (1 Td $=10^{-17}$ V cm^2) with there being a tendency for the E/N to decrease with increasing pressure as diffusion losses decrease. For example, for $\alpha=0.3$ eV/molecule, E/N in the bulk plasma decreased from 25 Td at 3 Torr to 13 Td at 50 Torr. (These values do not significantly change for higher values of α.) Since the fractional power deposition into $O_2(^1\Delta)$ is maximum for $E/N \approx 10-15$ Td, operating at higher pressures is kinetically more efficient since a larger fraction of power deposition is transferred to $O_2(^1\Delta)$.

Just as managing the O-atom and O_3 densities, and the gas temperature are important to scaling $O_2(^1\Delta)$ to higher pressures, so is managing the stability of the discharge. The transition from a diffusive and homogeneous discharge to one prone to instabilities or constricted states is not unusual when operating at higher pressures in electronegative gases.[12,15,19] At pressures lower than those associated with streamer propagation (as in corona discharges[24]) the onset of instabilities or constrictions results from a nonuniformity that produces local regions of higher power deposition or electron heating that diffusion is not able to disperse across a larger volume. That is, electron transport is local as opposed to nonlocal.

In the geometry investigated here, pressure scaling is ultimately limited by an instability initiated by discharge constriction which occurs between 40 and 50 Torr. This trend is shown in Fig. 13 where the electron density and power deposition are plotted for pressures from 3 to 50 Torr for $\alpha=0.3$ eV/molecule. The corresponding gas densities are shown in Fig. 14. Power deposition, diffusively distributed at 3 Torr, gradually constricts about the downstream electrode, producing a corresponding constriction in the electron density. This constriction results, in part, from an increasing degree of rarefaction in the total gas density in going from upstream to downstream as the gas heats. The lower gas density near the downstream electrode enables a higher conductivity and higher local power deposition.

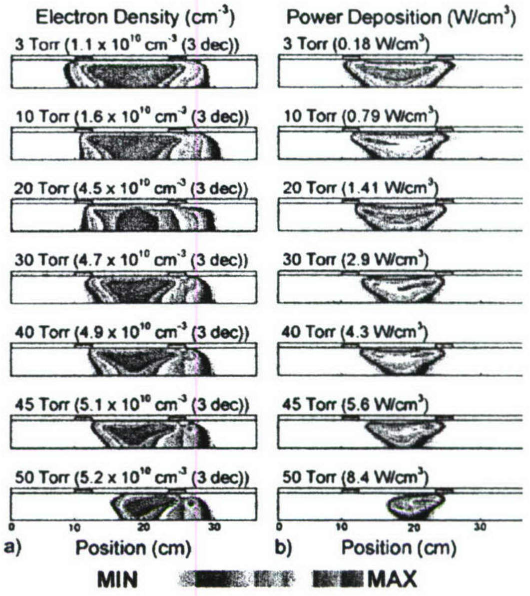

FIG. 13. (Color) Plasma parameters for pressures from 3 to 50 Torr ($He/O_2=70/30$, 25 MHz rf excitation, $\alpha=0.3$ eV/molecule). (a) Power deposition and (b) electron density. All values are averaged over one rf period. The flow is from the left. The scales are linear with zero minimum values unless the number of decades is indicated for log plots. The maximum value is indicated in each figure. Discharge constriction occurs near the downstream electrode due to rarefaction of the gas.

A measure of the onset of a constriction instability is the maximum value of the pressure normalized power deposition, P (W/cm^3 Torr). When keeping α constant and increasing pressure, and in the absence of constrictions, P should also remain a constant. The maximum value of P in the discharge, shown in Fig. 15, has a gradual increase from

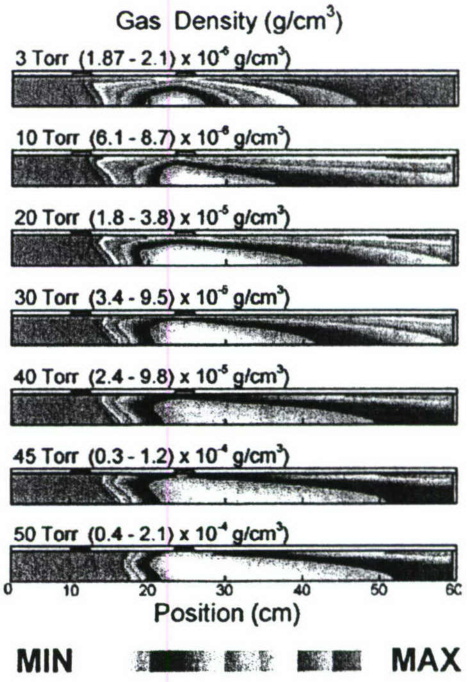

FIG. 14. (Color) Total gas density for pressures from 3 to 50 Torr ($He/O_2=70/30$, 25 MHz rf excitation, $\alpha=0.3$ eV/molecule). Significant rarefaction of the gas occurs near the downstream electrode.

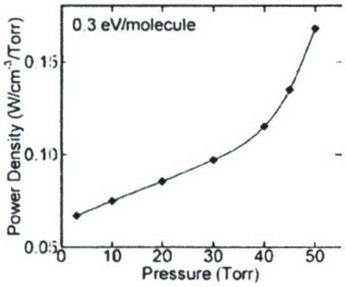

FIG. 15. Maximum value of the pressure normalized power deposition (W/cm^3 Torr) as a function of pressure (He/O_2=70/30, 25 MHz rf excitation, α=0.3 eV/molecule). A transition from a uniform and homogeneous discharge to constricted discharge occurs between 40 and 50 Torr.

3 to 40 Torr, followed by a rapid increase above 40 Torr. This rapid increase indicates a constriction in the discharge.

The axial distributions of gas temperature and neutral oxygen species are shown in Figs. 16 and 17 for pressures from 10 to 50 Torr for α=0.3 and 0.9 eV/molecule (133 and 400 W). The higher gas temperatures obtained at high pressures result in depletion of ozone in the afterglow. The maximum yields (15%–20% for α=0.3 and 25%–30% for α=0.9) are obtained at 50 Torr at the edge of the discharge zone. The yields then drop below 5% for α=0.3 and below 10% for α=0.9 due to quenching.

The hierarchy of the main quenchers of $O_2(^1\Delta)$ for 10, 30, and 50 Torr obtained with the 2D model is shown in Fig. 18 (α=0.3 eV/molecule) and Fig. 19 (α=0.9 eV/molecule). For the lower energy input (0.3 eV/molecule), O_3 is the main quencher in the afterglow up to 30–40 Torr. This result is basically the same as predicted by the plug-flow modeling. With increasing pressure and increasing absolute densities of atomic oxygen and $O_2(^1\Delta)$, quenching by these species begins to dominate. The pooling reaction,

$$O_2(^1\Delta) + O_2(^1\Delta) \rightarrow O_2(^1\Sigma) + O_2, \tag{22}$$

generates $O_2(^1\Sigma)$ as a product that is quenched to form $O_2(^1\Delta)$. For the higher energy input (0.9 eV/molecule), atomic oxygen and $O_2(^1\Delta)$ become the main quenchers in

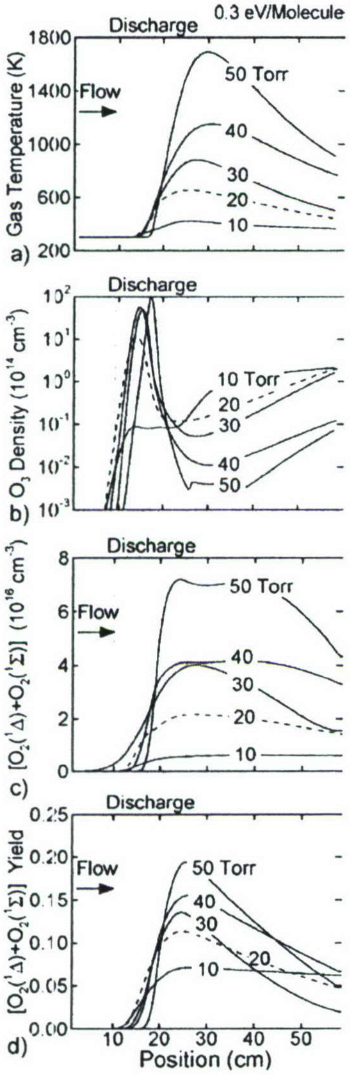

FIG. 16. Axial distribution of (a) gas temperature, (b) O_3 density, (c) $O_2(^1\Delta)+O_2(^1\Sigma)$ density, and (c) combined $O_2(^1\Delta)+O_2(^1\Sigma)$ yields (He/O_2=70/30, 25 MHz rf excitation) for α=0.3 eV/molecule.

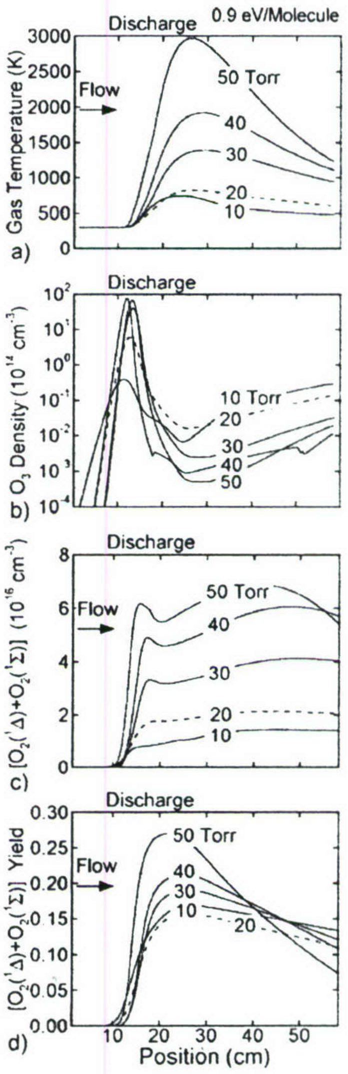

FIG. 17. Axial distribution of (a) gas temperature, (b) O_3 density, (c) $O_2(^1\Delta)+O_2(^1\Sigma)$ density, and (c) combined $O_2(^1\Delta)+O_2(^1\Sigma)$ yields (He/O_2=70/30, 25 MHz rf excitation) for α=0.9 eV/molecule.

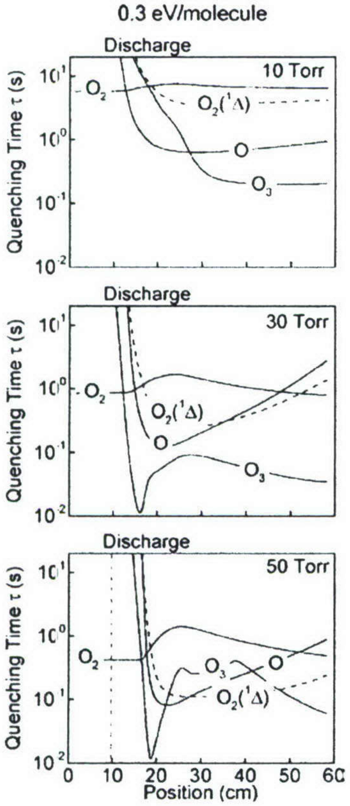

FIG. 18. Quenching times for $O_2(^1\Delta)$ for (a) 10, (b) 30, and (c) 50 Torr ($He/O_2=70/30$, 25 MHz rf excitation) for $\alpha=0.3$ eV/molecule. Up to 30–40 Torr ozone is the main quencher in the afterglow. With increasing pressure and increasing absolute densities of atomic oxygen and pooling reactions of $O_2(^1\Delta)$, quenching by these species begins to dominate.

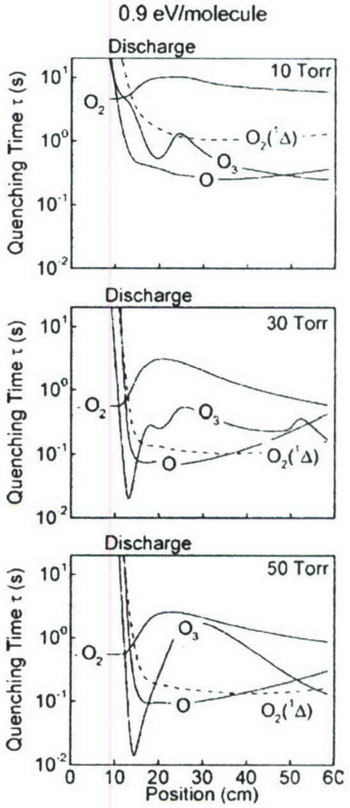

FIG. 19. Quenching times for $O_2(^1\Delta)$ for (a) 10, (b) 30, and (c) 50 Torr ($He/O_2=70/30$, 25 MHz rf excitation) for $\alpha=0.9$ eV/molecule. Quenching by atomic oxygen and pooling reactions of $O_2(^1\Delta)$ dominate.

the afterglow even for lower pressures, as shown in Fig. 19.

A summary of pressure scaling for $O_2(^1\Delta)$ production is shown in Fig. 20. $O_2(^1\Delta)$ densities and yields obtained from the 2D model as a function of power (for $\alpha=0.3$, 0.6, and 0.9 eV/molecule) are plotted for different pressures. These values are taken on the tube axis near the exit plane at 58 cm. Absolute $O_2(^1\Delta)$ production generally increases with power for any given pressure; however, it is not necessary maximum at the highest pressure. The yield of $O_2(^1\Delta)$ also increases with power for any given pressure; however, the yield at a given power generally decreases with pressure. These trends are largely a result of the increase in gas heating and influence of O_3, O, and $O_2(^1\Delta)$ quenching at higher pressures, and discharge constriction resulting from nonuniform rarefaction along the flow tube.

V. CONCLUDING REMARKS

Pressure scaling of the absolute densities and yields of $O_2(^1\Delta)$ in flowing He/O_2 plasmas was investigated using plug-flow and 2D plasma hydrodynamics models. We found that the densities and yields of $O_2(^1\Delta)$ can have significant sublinear scaling with pressure. Although yields may decrease with increasing pressure, absolute densities of $O_2(^1\Delta)$ typically do increase. Although these results depend on the layout of the electrodes and the aspect ratio of the flow tube more general conclusions can be made. Obtaining high yields of $O_2(^1\Delta)$ will require careful management of the O_3 density. Left unchecked, quenching of $O_2(^1\Delta)$ by the O_3 produced at high pressure is a rate limiting step. At higher energy densities and pressures, quenching by O atoms and en-

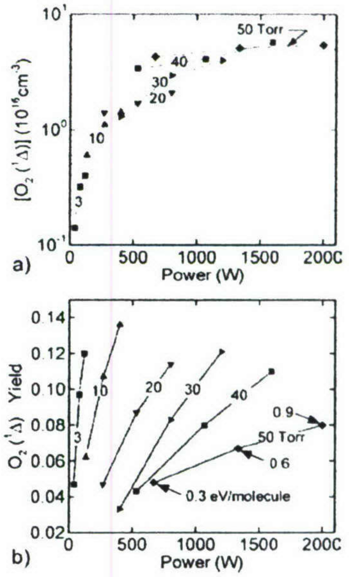

FIG. 20. Summary of pressure scaling of (a) $O_2(^1\Delta)$ densities and (b) yields as a function of power ($He/O_2=70/30$, 25 MHz rf excitation). Values are on the axis at 58 cm. $O_2(^1\Delta)$ production increases with increasing eV/molecule while yields at higher pressures may decrease.

ergy pooling with $O_2(^1\Delta)$ may also become important. This is particularly the case for possible three-body quenching involving O atoms, though the importance of this reaction can be minimized by managing the density of O atoms with additives such as NO. Pressure scaling also requires management of the gas temperature, as the rate of exothermic recombination reactions rapidly increase. Although the destruction of O_3 at higher temperatures is beneficial, in general an intermediate gas temperature is likely preferred. Discharge stability must also be managed and this will be highly temperature dependent. Nonuniform excursions of gas temperature in the plasma zone will produce nonuniform power deposition and constrictions near electrodes. As such, low aspect ratio, transverse electrodes allowing for more aggressive gas cooling and more distributed electric fields will likely be required for high pressure operation.

ACKNOWLEDGMENTS

This work was supported by the Air Force Office of Scientific Research and the National Science Foundation (CTS-0520368).

[1] W. E. McDermott, N. R. Pchelkin, D. J. Benard, and R. R. Bousek, Appl. Phys. Lett. **32**, 469 (1978).

[2] H. Fujii, S. Yoshida, M. Iizuka, and T. Atsuta, J. Appl. Phys. **67**, 3948 (1990).

[3] A. Elior, B. D. Barmashenko, E. Lebiush, and S. Rosenwaks, Appl. Phys. B: Lasers Opt. **B61**, 37 (1995).

[4] M. Endo *et al.*, IEEE J. Quantum Electron. **34**, 393 (1998).

[5] D. Furman, E. Bruins, V. Rybalkin, B. D. Barmashenko, and S. Rosenwaks, IEEE J. Quantum Electron. **37**, 174 (2001).

[6] J. Kodymova, O. Spalek, V. Jirasek, M. Censky, and G. D. Hager, Appl. Phys. A: Mater. Sci. Process. **77**, 331 (2003).

[7] J. Kodymova and O. Spalek, Jpn. J. Appl. Phys., Part 1 **37**, 117 (1998).

[8] A. A. Ionin, Y. M. Klimachev, A. A. Kotkov, I. V. Kochetov, A. P. Napartovich, L. V. Seleznev, D. V. Sinitsyn, and G. D. Hager, J. Phys. D **36**, 982 (2003).

[9] D. L. Carroll, J. T. Verdeyen, D. M. King, B. S. Woodard, L. W. Skorski, J. W. Zimmerman, and W. C. Solomon, IEEE J. Quantum Electron. **39**, 1150 (2003).

[10] Yu. V. Savin *et al.*, J. Phys. D **37**, 3121 (2004).

[11] A. N. Vasiljeva, K. S. Klopovskiy, A. S. Kovalev, D. V. Lopaev, Y. A. Mankelevich, N. A. Popov, A. T. Rakhimov, and T. V. Rakhimova, J. Phys. D **37**, 2455 (2004).

[12] A. Hicks, S. Norberg, P. Shawcross, W. Lempert, J. W. Rich, and I. Adamovich, J. Phys. D **38**, 3812 (2005).

[13] D. S. Stafford and M. J. Kushner, J. Appl. Phys. **98**, 073303 (2005).

[14] N. Yu. Babaeva, R. A. Arakoni, and M. J. Kushner, J. Appl. Phys. **99**, 113306 (2006).

[15] O. V. Braginsky, A. S. Kovalev, D. V. Lopaev, Yu. A. Mankelevich, O. V. Proshina, T. V. Rakhimova, A. T. Rakhimov, and A. N. Vasilieva, J. Phys. D **39**, 5183 (2006).

[16] O. V. Proshina, T. V. Rakhimova, O. V. Braginsky, A. S. Kovalev, D. V. Lopaev, Yu. A. Mankelevich, A. T. Rakhimov, and A. N. Vasilieva, J. Phys. D **39**, 5191 (2006).

[17] G. Bauville, B. Lacour, L. Magne, V. Puecha, J. P. Boeuf, E. Munoz-Serrano, and L. C. Pitchford, Appl. Phys. Lett. **90**, 031501 (2007).

[18] D. L. Carroll *et al.*, Appl. Phys. Lett. **85**, 1320 (2004).

[19] A. Hicks, Yu. G. Utkin, W. R. Lempert, J. W. Rich, and I. V. Adamovich, Appl. Phys. Lett. **89**, 241131 (2006).

[20] D. L. Carroll *et al.*, Appl. Phys. Lett. **86**, 111104 (2005).

[21] D. L. Carroll *et al.*, IEEE J. Quantum Electron. **41**, 1309 (2005).

[22] A. A. Ionin, I. V. Kochetov, A. P. Napartovich, and N. N. Yuryshev, J. Phys. D **40**, R25 (2007).

[23] K. S. Klopovskii, A. S. Kovalev, D. V. Lopaev, N. A. Popov, A T. Rakhimov, and T. V. Rakhimova, JETP Lett. **80**, 603 (1995).

[24] G. V. Naidis, J. Phys. D **38**, 2210 (2005).